# PIEZOELECTRIC NANOSCALE ULTRASOUND TRANSDUCERS (PNUTS) FOR MINIATURIZED INTERNET OF THINGS RECEIVERS

Submitted in partial fulfillment of the requirements for

the degree of

Doctor of Philosophy

in

Electrical and Computer Engineering

Pietro Simeoni

B.S., Physics Engineering, Politecnico di Torino
M.S., Nanotechnologies for the ICTs, Politecnico di Torino

Carnegie Mellon University
Pittsburgh, PA

May 2021

## ACKNOWLEDGMENT

*In primis*, I would like to thank my defense committee members Gianluca Piazza, Maysam Chamanzar, Tamal Mukherjee, and Matteo Rinaldi for their valuable feedback and insights on the work presented in this thesis. In particular, I would like to thank my advisor Gianluca for his guidance over the last 4 years. Looking back at the progress made since I started I could not be more grateful for his guidance.

Secondly, a big thank you to my family back in Italy. I have been fortunate enough to have two parents that supported me in the path I chose, even when it meant being far from home for most of my adult life. Successfully completing this program is an achievement that is as much mine as it is theirs.

A thanks goes to the amazing friends and colleagues that helped me in small and big ways to maintain a balanced perspective on life, especially in moments I was doubting whether I would be able to complete my Ph.D. A special mention goes to the "pasta club". Antonis, Marina, Luca, and Gabri, thanks for the precious memories of my years in Pittsburgh.

An equally important thanks goes my colleagues and friends Gabriel, Zach, and James. Besides the invaluable help you gave me to complete my thesis, our 5 pm discussions definitely made me a better person. Our conversations kept me sharp, challenged my believes, gave me perspective, and showed me what civil disagreement looks like.

Thank you to all my friends that were on this journey with me including Harlin, Ayaz, Shafee, Ashraf and Abhay.

Finally, I would like to acknowledge the sources of funding that made my work possible. This includes the Carnegie Mellon Electrical and Computer Engineering Department for supporting my first year and the DARPA SHIELD and NZERO programs for supporting me

during my second and fourth year. I would like to thank Marsha and Philip Dowd for providing financial support during my third year through the 2019 Dowd Graduate Fellowship. I am honored to be a Dowd fellow and I am immensely grateful to them for believing in the project.

# PIEZOELECTRIC NANOSCALE ULTRASOUND TRANSDUCERS (PNUTS) FOR MINIATURIZED INTERNET OF THINGS RECEIVERS

Abstract

Pietro Simeoni
Carnegie Mellon University
February 2021

The landscape of connected devices has both grown in size and changed in nature in the last few decades. When the internet came along, it represented a first wave of connectivity that enabled communication between desktop computers. As computers moved to smaller form factors such as laptops and more recently smartphones, the need for connectivity was extended to this class of devices. This second wave was wireless in nature, and came with the additional constraint of lower power consumption as these devices are powered by batteries. We are now going through a third wave of connectivity, where everyday appliances and sensor nodes distributed in the environment are equipped with the ability to remotely receive and report back information. This third wave is commonly referred to as the internet of things (IoT), and as it rolls out, the constraints on form-factor and power consumption become increasingly tight and challenging to engineer.

Because of the high density of wireless nodes, radio frequency bands are becoming a scarce resource and they constitute yet another constraint to account for during the system design. The number of wireless nodes is increasing exponentially and we expect to have a trillion sensors deployed by the year 2030. To make the deployment of a trillion sensors feasible, these nodes must be small and function on limited power budgets. For a subset of

IoT applications, a network of sensors would need to be installed in a localized area, where the required communication range is less than 10 m and where a central hub can orchestrate the connection between different nodes.

For such applications, ultrasound between 40 kHz and 100 kHz becomes an attractive candidate to overcome several of the constraints outlined above. This frequency range offers two important advantages: 1) The acoustic waves attenuation is low and permits communication over several meters (loss $< 3$ dB/m). 2) The node electronics can operate at extremely low power, potentially extending its lifetime to several years while drawing power from a miniaturized battery.

If ultrasound is used in place of RF waves, we must replace the node antenna with an ultrasound transducer. In this work we introduce a novel ultrasound sensor that we dub the piezoelectric nano-scale ultrasound transducer (pNUT). The pNUTs are characterized by piezoelectric films that are only 100 nm thick and by a footprint that is 1 to 2 orders of magnitude smaller than the state of the art, while showing similar performance. A model for the scaling of ultrasound transducers is presented to offer guidelines for the design of miniaturized ultrasound sensors. Finally, we design a circuit with accessible off-the-shelf components to demonstrate a low-power pNUT-based ultrasound wake-up receiver (WuRx). The WuRx presents a communication range of several meters, confirming the feasibility of miniaturized ultrasound tags for distributed sensors networks.

# TABLE OF CONTENTS

# LIST OF TABLES

# LIST OF FIGURES

**Dedication**

This dissertation is dedicated to

Daniela, Marco, Luca, and Nicola

# Chapter 1

# Introduction

## 1.1 Background

The landscape of connected devices has both grown in size and changed in nature in the last few decades. When the internet came along in 1982, there were much fewer nodes mainly represented by desktop computers. As micro fabrication techniques improved and Moore's law unfolded, the number of operations a computer could perform per unit of energy grew exponentially, which led to a differentiation in the type of devices that were commercially available. Desktop computers improved in performance, and laptop computers were born thanks to the increase in efficiency that allowed them to operate on a battery power supply and within reasonable form factors. This trend continued, and combined with advances in radio frequency (RF) front ends, sensors miniaturization, and battery chemistry, it produced a several consumer-electronic products such as cellphones first, smartphones after them, and a variety of devices like smartwatches, earbuds, home pods etc. As a hobbyist, it is possible to inexpensively purchase small micro-controller boards equipped with wifi and bluetooth modules and experiment building personal internet-connected devices. To go even further, there are a lot of parallel research efforts to miniaturize these wireless modules and ensure bio-compatibility to implant them in human bodies, where they can monitor a variety of

health related variables [1][2]. The exponential growth of nodes connected to the network, and the breadth of form and scope of these nodes is referred to as the Internet of Things (IoT) [3].

The advancements in integrated circuit (IC) manufacturing described above enable the design of extremely miniaturized computing platforms (Fig.1.1) that can accommodate sufficient processing, memory, and sensing in just a few square millimeters area.

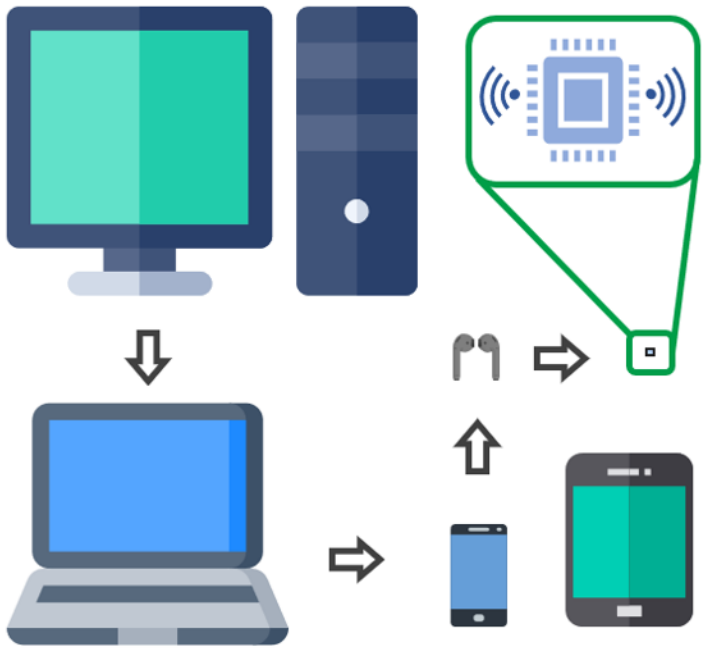

**Figure 1.1** The evolution of computers. This is a qualitative illustration of how the nature of computing platforms changed in size and nature over the last several decades.

These nodes are meant to record a variety of variables from the environment around them, and report them back to a central hub (star network configuration). The nodes are set to implement different functions that can go from machinery temperature monitoring, to indoor position tracking for items in a warehouse, to air quality control in traffic intersections. Because of the general purpose of these sensing nodes, they are meant to be deployed in high numbers to collect abundant information from their surroundings. In order to make the deployment of a high number of these nodes feasible, three requirements must be satisfied.

The nodes must:

- Be small
- Secure privacy
- Have long lifetimes

The privacy issue is outside the scope of this thesis. We will instead focus on the challenges related to miniaturization and power consumption. The power consumption issue is a direct consequence of making these nodes wireless, which is necessary due to the distributed nature of these sensor networks. If we are using RF to communicate wirelessly with the node, it needs to be equipped with an antenna. To receive RF signals efficiently, antennas need to have lateral dimensions comparable to the wavelength of operation. In contrast, the electronics interfacing the antenna would benefit to operate at lower frequency (i.e. larger wavelengths) to maintain a low power consumption. Therefore, a physics-limited trade-off exists in making a wireless node that is simultaneously small and power efficient. Since the relationship between wavelength and frequency is set by the propagation speed of the wave, this thesis explores the possibility of taking advantage of the lower propagation speed of airborne acoustic waves to build a small receiver that operates on a limited power budget. This idea is illustrated in Fig. 1.2.

Ultrasound (US) in the 40 - 100 kHz range is especially interesting as it is characterized by millimeters-long wavelengths, while presenting relatively low attenuation in air ($< 3$dB/m) [4]. This guarantees a communication range of 5 to 10 meters, making the approach attractive for a subset of applications.

## 1.2 Ultrasound Transducers and State of the Art

If we use ultrasound as a preferred communication approach, we need to substitute the node antenna with an ultrasound transducer. There are two types of transducers commonly used

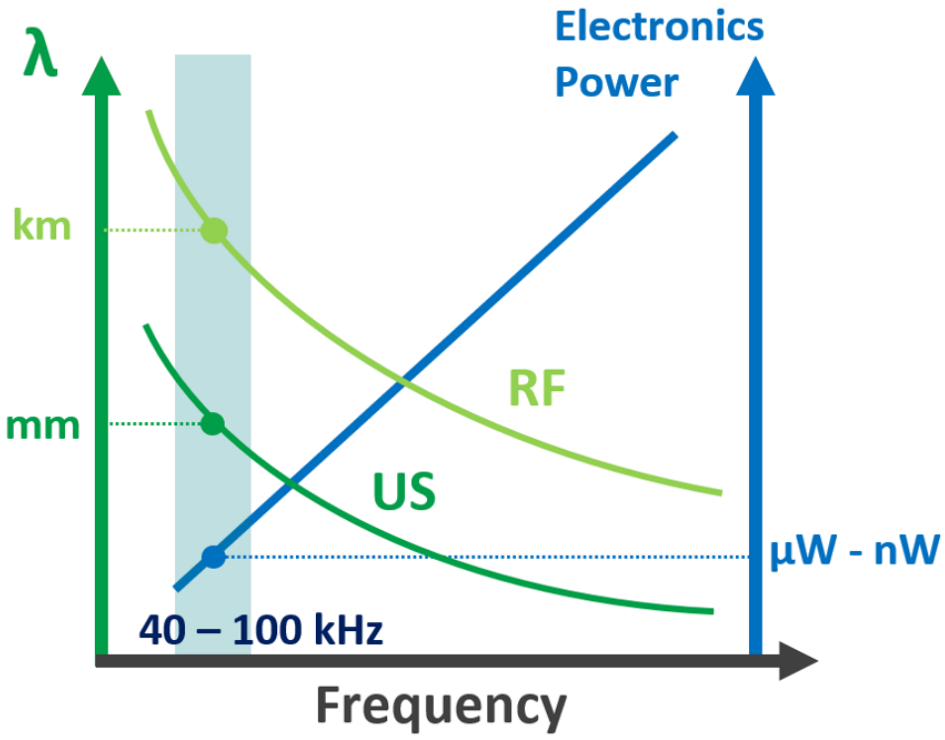


**Figure 1.2** Relation between wavelength and frequency for RF and US, and power consumption of the interfacing electronics.

commercially and in research (Fig. 1.3):

- Capacitive Micromachined Ultrasound Transducer (cMUT)
- Piezoelectric Micromachined Ultrasound Transducer (pMUT)

cMUTs are parallel plate capacitors separated by an air gap. The top plate is only anchored laterally and is therefore free to bend when an external pressure is applied. As the plate moves, the value of the capacitance between the two plates changes accordingly. To measure a net current flow resulting from the displacement, we need to apply a polarization voltage between the two plates. This requirement implies that cMUTs transduction mechanism is inherently not passive, and therefore not suitable for the low-power applications we are targeting. pMUTs consist of multi-layer suspended plates with at least one layer made of a piezoelectric ceramic. As an external pressure bends the plate, the *direct piezoelectric*

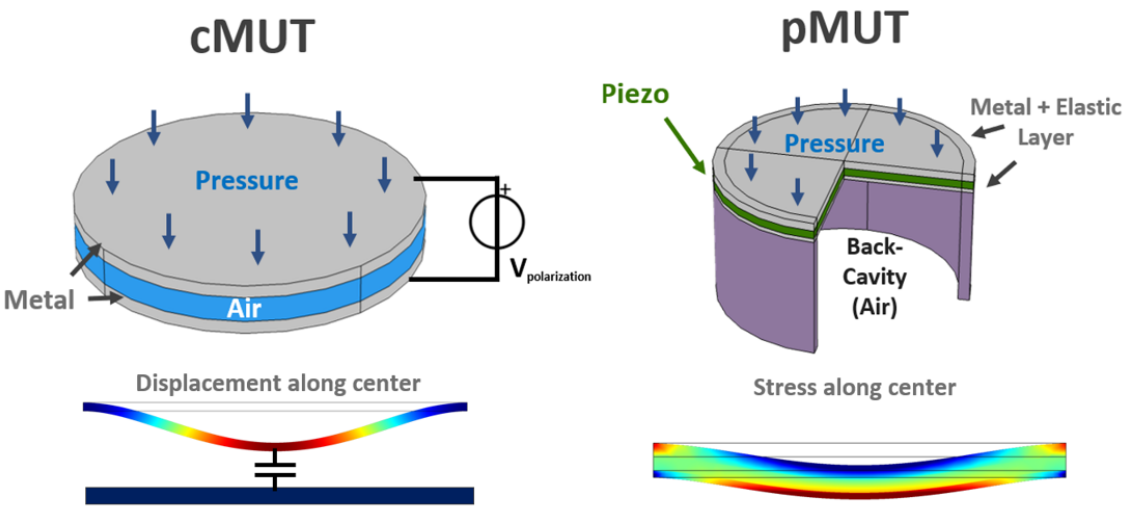


**Figure 1.3** Depiction of the two most common typologies of MEMS ultrasound transducers: cMUTs (left) and pMUTs (right).

*effect* converts the resulting in-plane strains into a charge polarization. The other layers in the stack serve two purposes. First, you have metal layers to form the electrodes that pick up and route the electrical signal, secondly you have an *elastic layer* responsible for shifting the *neutral plane* (zero-strain plane) away from the center of the piezoelectric layer. Moving the neutral plane is necessary to generate a net polarization across the piezoelectric thickness and detect a non-zero electrical output. Because the piezoelectric effect is a passive transduction mechanism, pMUTs are the device of choice for this thesis.

It is then interesting to see how ultrasound transducers, and pMUTs in particular, operating in the 40-100 kHz band evolved over time. From Fig. 1.4, we can see how advances in micro-fabrication and thin films deposition lead to a reduction in pMUTs lateral dimensions from few cm to just a few mm.

This reduction was enabled by thinning down the thickness of the piezoelectric layers from millimeters down to the µm range without degrading the piezoelectric properties of the films. The focus of this thesis is to explore the next phase of pMUTs miniaturization. The objective is using AlN films with thicknesses of only 100-200 nm to deliver an ultrasound transducer that resonates in the 40 - 100 kHz frequency range, while occupying a footprint

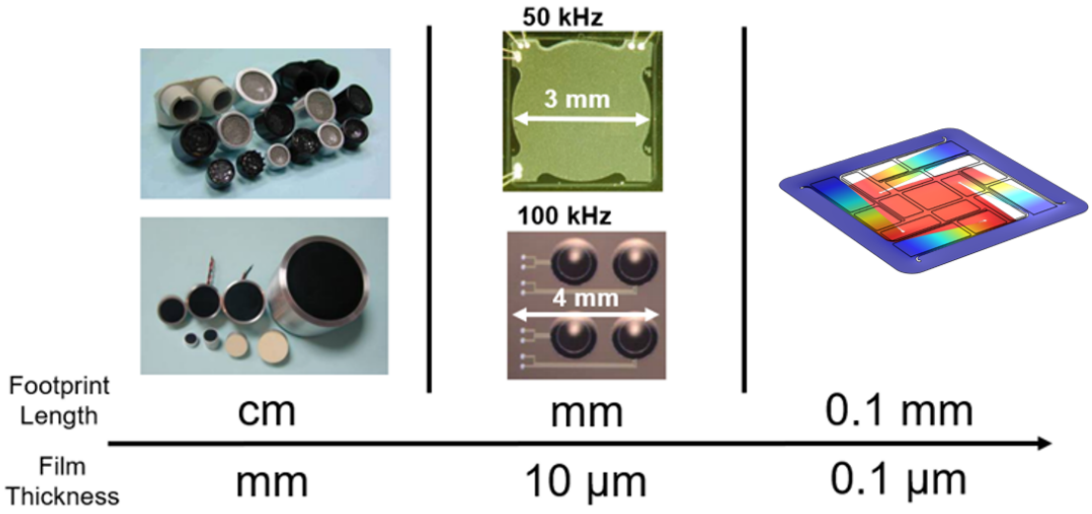


**Figure 1.4** Evolution of ultrasound transducers. As piezoelectric thin films synthesis improved, thinner piezoelectric layers enabled the fabrication of smaller low-frequency transducers. [5][6][7].

of approximately 100 µm x 100 µm, and without losing in performance with respect to its larger counterparts.

Such device would deliver two main advantages:

- If the design of the node is constrained by the available area, it is now possible to miniaturize the largest element of the system
- If the design is not constrained by the available area, smaller transducers can be arrayed together to occupy a larger area, and increase the system sensitivity and range

In the next chapters we will explore the advantages and limitations of thickness scaling as an approach for miniaturization. We will see that traditional geometries are not suitable for extremely thin films, and that significant design changes need to be made to build functional devices. Because of the important design changes developed in this work, we consider these devices as a separate class from traditional pMUTs, and throughout this document we will refer to them as piezoelectric nanoscale ultrasound transducers (pNUTs).

## 1.3 Overview of the pNUT

In this section, we take a high-level look at how the pNUT is designed. The motivation behind the important design changes outlined below is related to the role played by residual stress in high-aspect ratio flexural resonators. If we tried to scale down the thickness of a classic circular pMUT, we will find that either its resonance frequency is dramatically different than the one predicted by its geometry and material properties, or simply that the device is broken. In both cases, we have that the residual stress in the films used to build the device introduces a very large tension in the plate. Because of the geometry and boundary conditions of pMUTs, this tension cannot be relaxed, leading either to a significant change in the plate stiffness or to mechanical failure. More details on this are presented in Chapter 2 (Section 2.2.2) and Chapter 3 (Section 3.2.1).

The proposed pNUT geometry consists of 4 cantilever beams connected to a common central plate. Like traditional circular pMUTs, the device is composed by a laminate comprising a piezoelectric and an elastic layer. As the ultrasound waves reach the device surface, the central plate is displaced vertically, forcing the 4 beams to bend. As bending moment is developed in the beams, the piezoelectric effect converts the acoustic energy into an electrical signal that can be read out by an electronic circuit. The deformation mode of the transducer is shown in Fig. 1.5.

From the image we show that the stack is composed by an aluminum nitride piezoelectric layer of approximately 100 nm thickness, sandwiched between two platinum layers with thicknesses of around 10 nm and 200 nm. In fact, because of the aggressive scaling in the piezoelectric layer, we show that the electrodes themselves can play the role of the elastic layer. The different thickness between top and bottom electrodes is then required to obtain a net shift in the neutral plane away from the center of the piezoelectric layer. On the right side of Fig 1.5. we present SEMs images of the early prototypes of the devices that motivated the research presented in this thesis. We can see that the top metal is patterned

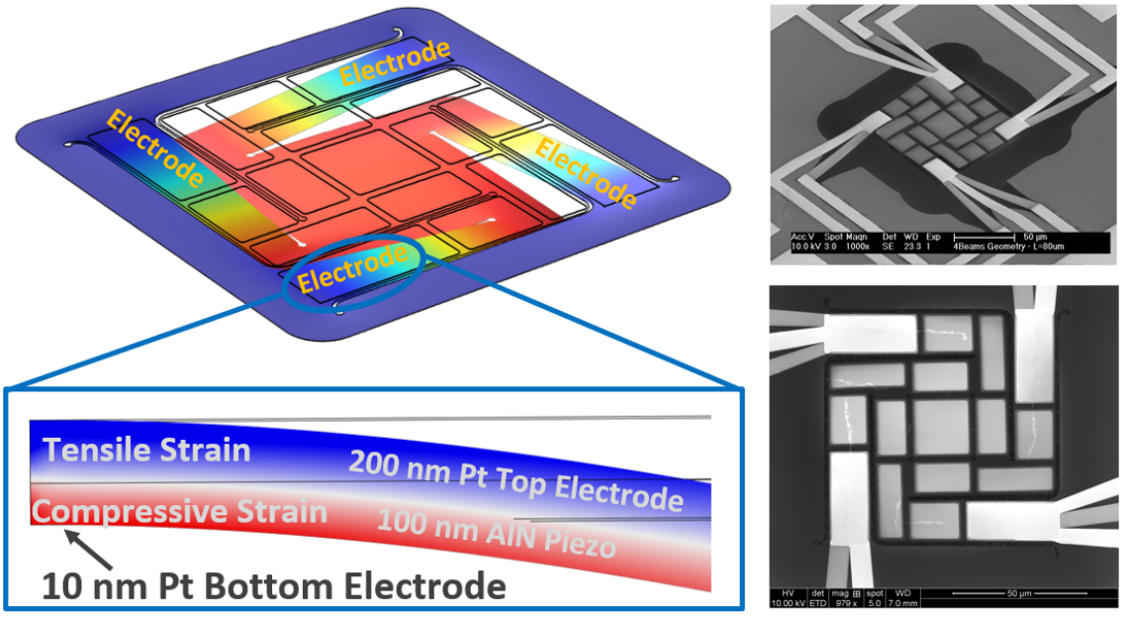


**Figure 1.5** Left: Main resonance mode of 4-beams pNUT. Right: SEM images of early prototypes of the devices.

on the central plate as well. While the details of the design and fabrication process will be presented in chapter 3, we highlight that only the electrodes on the beams anchors are required to have a functioning devices, and that the metal patterned on the rest of the device surface is there to help maintaining the resonance frequency in the desired range by mass loading the device. In the next section, we comment on some application scenarios for the pNUTs. An analytical model of the pNUT -along with its limits- is presented in Chapter 2. The fabrication process, challenges, and recommendations for future fabrications are presented in Chapter 3. Chapter 4 comments on how to model pNUTs when they are combined in an array. Finally we show experimental data in Chapter 5 and 6, where we talk about the experimental setups to characterize the devices and show a demonstration of a working ultrasound receiver.

## 1.4 Motivation and Applications

As mentioned above, the applications for distributed nodes networks that could benefit from an ultrasound wake-up receiver (WuRx) are numerous. Typically, use-case scenarios include, but are not limited to, any indoor settings (Fig. 1.6).

**Figure 1.6** Application scenarios for distributed sensing tags equipped with ultrasound receivers.

Possible settings that are characterized by a wealth of information that can be gathered through sensors networks are factory floors, warehouses, and healthcare facilities. The example of what a factory floor populated with distributed sensors is shown in Fig. 1.7.

A functional network is made by two types of objects, a transmitter (Tx) that represents the central hub of the network, and a receiver (Rx), which in this case is embedded in the sensing tags distributed across the monitored space. The job of the Tx is to orchestrate the information recovery from the tags. To do that, it sends out a key that is picked up by the Rx in the tags. The low-power consumption afforded by an ultrasound-based receiver, makes it ideal to build a WuRx. WuRxs are useful whenever you have a duty-cycled system that needs to be active infrequently (e.g. once every hour) and for short amounts of time. When this conditions are met, the system can be left asleep for most of its lifetime, therefore saving

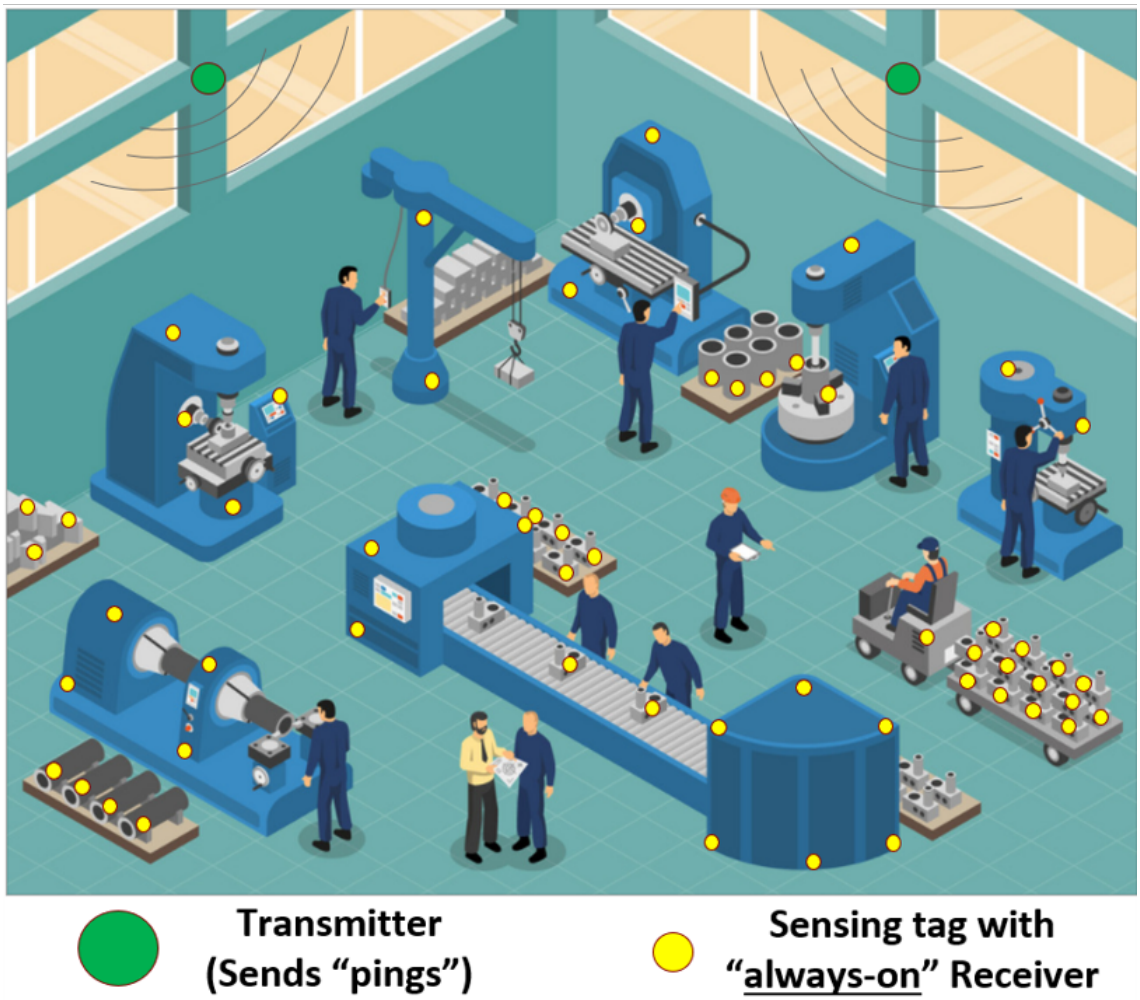


**Figure 1.7** Factory floor with a distributed network of sensors.

power. At the same time, the WuRx is always on while operating on extremely low power budgets, and it brings the main system back to life whenever a specific signature is detected. These type of systems have gathered increasing interest in recent years as industrial and military IoT technology is rolled out, and more computing moves further to the edges of the network. At the edges, access to the power grid is often not an option and despite the less demanding nature of the computations, energy remains a scarce resource. The recent DARPA program NZERO [8][9] is an example of such need. The program produced several systems tackling the problem in different and creative ways such as those described in [10] [11] [12]. An example of a WuRx that uses ultrasound can be found in [13].

Another application of interest is the use of ultrasound sensors for indoor navigation. Notoriously, GPS does not work in indoor spaces, as the frequency bands used by the satellites are blocked by buildings walls. Interest in the field is highlighted by competitions organized by Microsoft [14], where our colleagues at Carnegie Mellon ranked 6th worldwide with their ultrasound time-of-flight approach [15]. Miniaturizing ultrasound transducers while maintaining high sensitivity would simplify the integration with ICs and enable mass production of small, low-cost tags for indoor positioning.

Finally, using the acoustic waves themselves to remotely transfer power to small tags is another area that is being explored [4]. Miniaturizing the transducers and creating arrays to cover larger areas would offer better coupling to the acoustic waves than a single large transducer, thus increasing the power conversion efficiency per unit area. This would effectively create zero-power tags that can be turned on remotely when necessary. An example of an application of such technology is shown in Fig. 1.8.

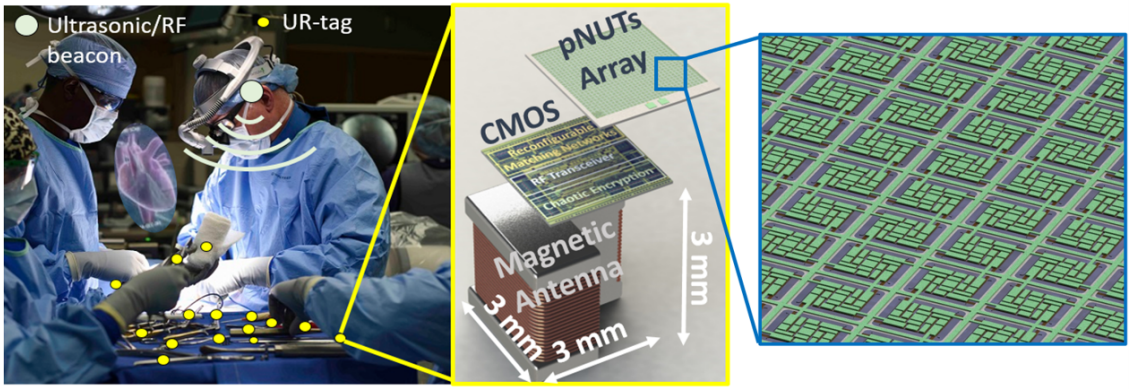


**Figure 1.8** Zero power tags for locating objects in mixed-reality.

# Chapter 2

# Individual pNUTs Modeling

In this chapter we model and study the dynamics of piezoelectric Nanomachined Ultrasonic Transducer (pNUT). We treat them as flexural resonators operating in the linear regime. An equivalent circuit model is used to describe the frequency behavior of the devices, similarly to what has been previously done for microscale devices [16] [17]. Notice that in the 40 - 100 kHz frequency range, airborne acoustic waves have wavelengths between 8.5 and 3.5 mm, 1 to 2 orders of magnitude larger than the pNUTs lateral dimensions. It is then appropriate to model the devices as lumped-element circuits. We will also point out in what specific circumstances the pNUT model deviates from more classical microscale counterparts.

## 2.1 Equivalent Circuit Model

The complete equivalent circuit for an ultrasound transducer operating in receive (Rx) mode is shown in Fig. 2.1

The circuit is divided in three sections, each representing a distinct physics domain: acoustic, mechanical, and electrical. Variables in the separate domains relate to each other through proportionality factors described by transformer elements. Table 2.1 shows the appropriate units for components and variables in each domain.

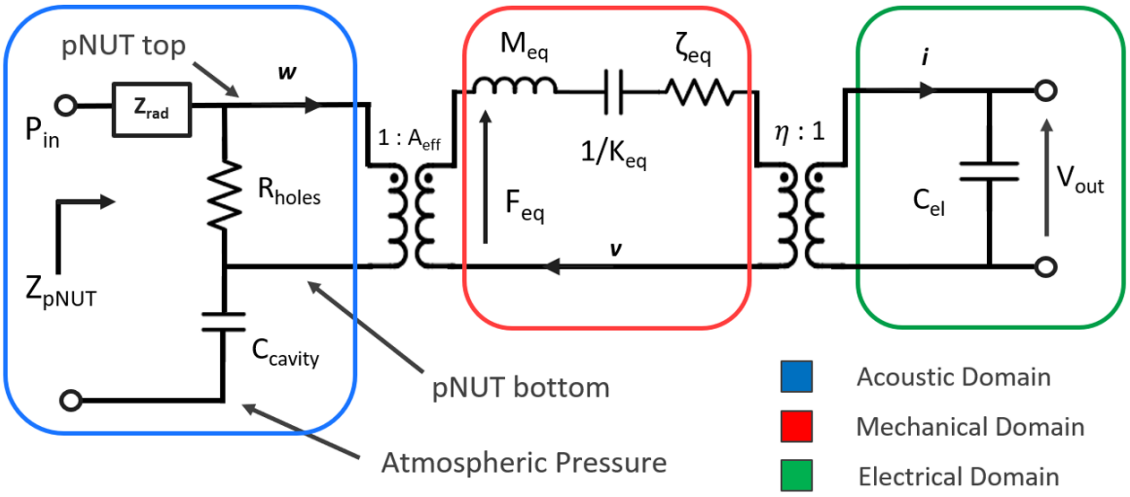


**Figure 2.1** Lumped equivalent circuit of a pNUT.

**Table 2.1** Units of components and variables of the equivalent circuit in the acoustic, mechanical, and electrical domain

| Component/Variable | Acoustic | Mechanical | Electrical |
|---|---|---|---|
| Resistor | $\frac{Ns}{m^5}$ | $\frac{Ns}{m}$ | $\Omega$ |
| Capacitor | $\frac{m^5}{N}$ | $\frac{m}{N}$ | $F$ |
| Inductor | $\frac{kg}{m^4}$ | $kg$ | $H$ |
| Voltage | $Pa$ | $N$ | $V$ |
| Current | $\frac{m^3}{s}$ | $\frac{m}{s}$ | $A$ |

We proceed to describe each domain and derive analytical expressions for the elements associated with each one of them.

### 2.1.1 Airborne waves propagation

The propagation of acoustic waves from the ultrasound source (Tx) to the pNUT takes place over several wavelengths. Therefore, while the frequency response of the device can be modeled as a lumped equivalent circuit, the energy that is transferred from the airborne incident wave to the device depends on the impedance matching between the medium and

the pNUT. To illustrate this concept, we can draw intuition from delay line theory. In a delay line, the level of matching is typically quantified by the $\Gamma$ factor [18]:

$$\Gamma = \frac{Z_L - Z_0}{Z_L + Z_0} \tag{2.1}$$

As a forward-propagating wave $P^+$ encounters an impedance $Z_L$ that is different from the medium characteristic impedance $Z_0$, a reflected (i.e. backward-propagating) wave $P^-$ with amplitude $\Gamma P^+$ is generated. The net amplitude of the wave at the location of $Z_L$ is then equal to $P^+ + P^- = P^+(1 + \Gamma)$.

In our case, assuming line-of-sight communication, the equivalent delay line is represented by the channel formed by projecting the pNUT area on the source as shown in Fig. 2.2.

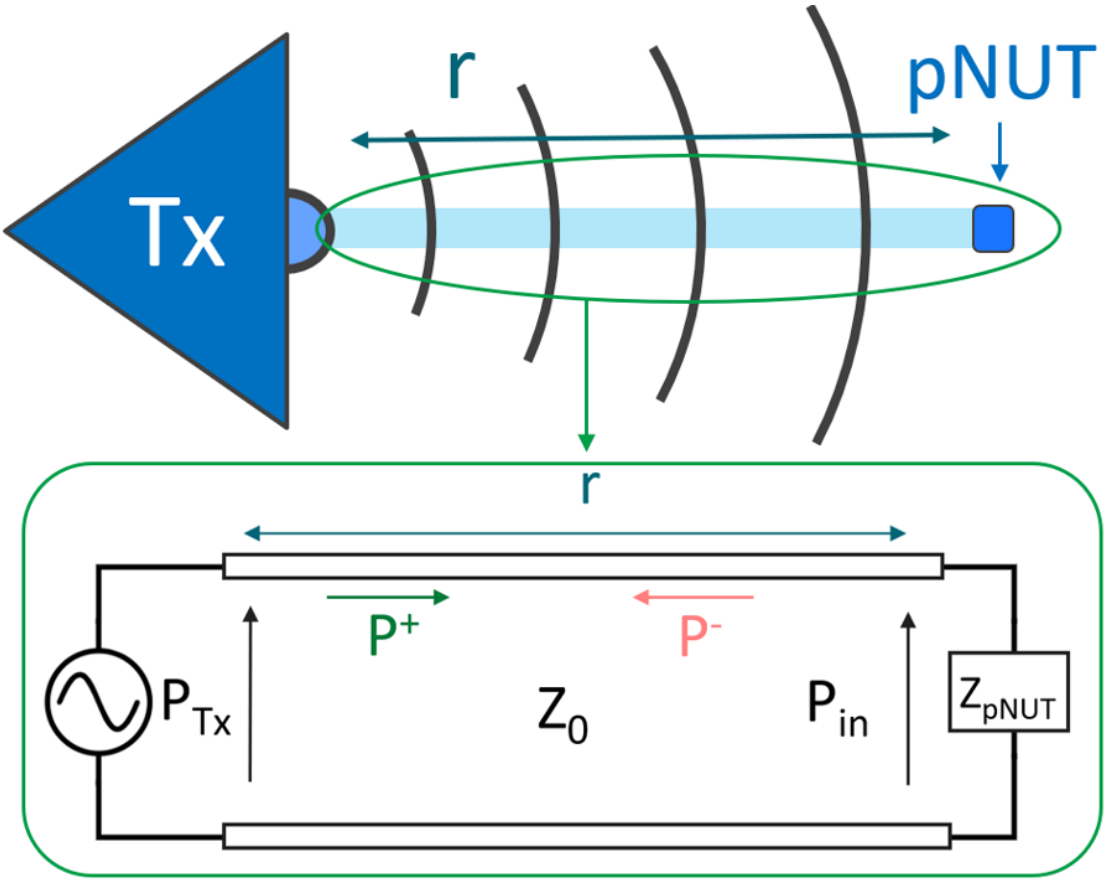


**Figure 2.2** Delay line analogy for acoustic waves propagating from Tx to pNUT.

$Z_0$ is the *characteristic acoustic impedance*, and its value is set by the properties of the medium and by the channel cross-sectional area, which is the transducer total area $A$:

$$Z_0 = \frac{\rho_{air} c_{air}}{A} \tag{2.2}$$

where $\rho_{air}$ is the air density and $c_{air}$ is the sound velocity in air. $Z_L$ is equal to the impedance $Z_{pNUT}$, the impedance seen from the acoustic input of the equivalent circuit model, and it is a function of frequency.

Given the small cross-sectional area of the channel, we approximate the pressure wave in it as a plane wave. As the wave travels the distance between the Tx and the pNUT, its amplitude decreases due to two main mechanisms:

- Spreading losses. As the wavefront total surface increases, the intensity, measured in $W/m^2$ decreases with the inverse of $r^2$, where r is the distance from the Tx.
- Viscous losses. This loss results from heat dissipation as the wave compresses and releases the medium molecules. This loss is approximately 1 - 2.5 dB/m in in the 40 - 100 kHz band in air [4].

Accounting for these two loss mechanisms, the acoustic pressure amplitude as the wave propagates away from the Tx is given by:

$$P_{in} = (1 + \Gamma)\gamma P_{Tx} e^{-\alpha r} \frac{r_{Tx}}{r}. \tag{2.3}$$

In equation 2.3, $\gamma$ is a coefficient that accounts for the directivity of the Tx, $P_{Tx}$ is the pressure at the Tx, $r$ is the distance between the Tx and the pNUT, $\alpha$ is a coefficient that accounts for viscous losses, and $r_{Tx}$ is the radius of the Tx itself. We can get a first order idea of the pressure amplitudes we can generate at a given distance by plotting the pressure

generated by an ideal isotropic ($\gamma = 1$) hemispherical Tx with a radius of 10 cm. Assuming a maximum initial pressure of 350 Pa as mandated by current regulations [4] we can see in Fig. 2.3 the generated pressure over distance for a signal at 40 kHz and 100 kHz.

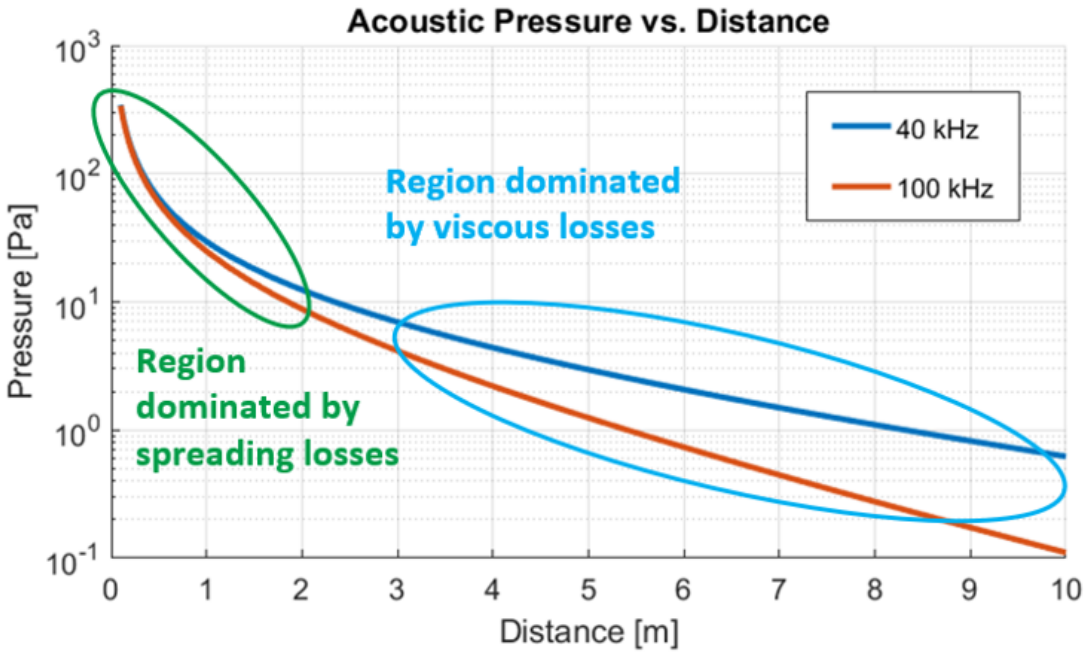


**Figure 2.3** Acoustic pressure generated by an ideal isotropic hemispherical Tx with a radius of 10 cm.

For a given distance, we can then obtain the acoustic pressure present on the transducers top surface by multiplying the propagated acoustic pressure value by $(1 + \Gamma)$.

### 2.1.2 Acoustic Domain

The acoustic domain is characterized by three main components: the capacitor $C_{cavity}$, the resistor $R_{holes}$, and transducer radiation impedance ($Z_{rad}$). We now describe the nature of these components and describe how to quantify them to a first order.

$C_{cavity}$ represents the effect of the hollow volume behind the transducer. At rest, the acoustic pressure on the backside of the device is equal to zero. When the suspended plate moves vertically, for example when electrically actuated or excited by an incident acoustic wave, a small change in the volume of the back-cavity takes place. As a result, the pressure

in the cavity shifts away from atmospheric pressure in proportion to the relative change of the volume [19]. Therefore, the back-cavity behaves as a spring element that opposes the motion of the transducer. The value of the equivalent capacitor is given by

$$C_{cavity} = \frac{V}{\rho_{air} c_{air}^2} \tag{2.4}$$

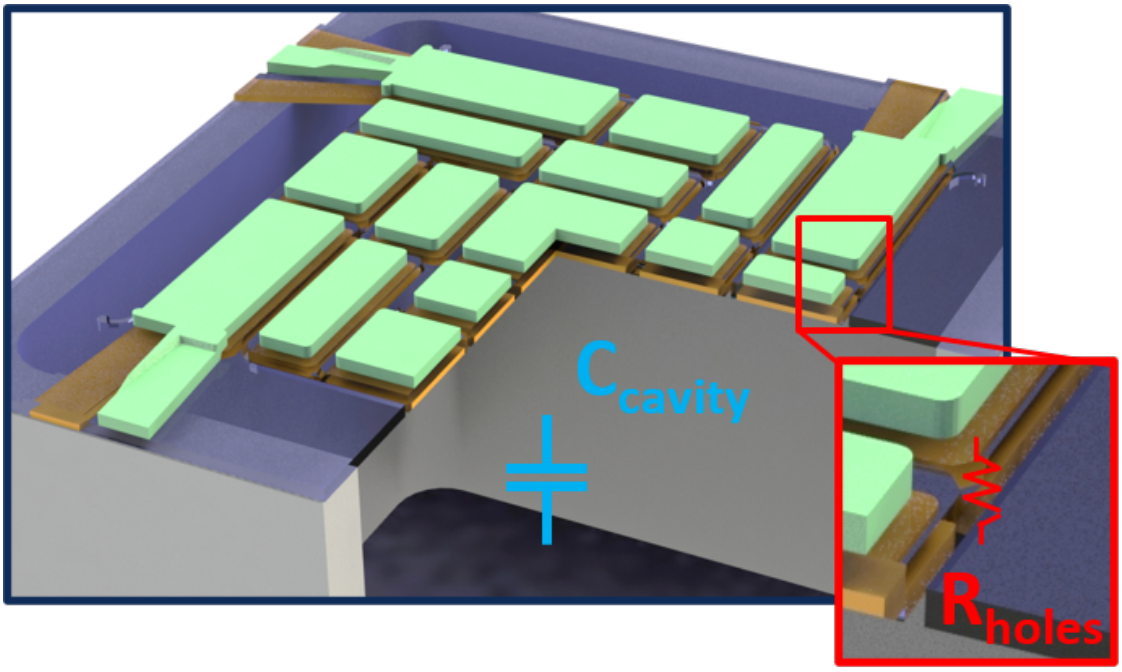


**Figure 2.4** Rendering of the transducer portions modeled by $C_{cavity}$ and $R_{holes}$.

The device geometry is generated by etching slots through the AlN layer. This creates a path for pressure equalization between the top and bottom side of the device. This effect is represented by the equivalent resistor $R_{holes}$. Estimating the value of this component analytically is not easy; when the device is released, it bends out of plane because of the stress-gradients across the films stack thickness, complicating the geometry of the slots. However, an upper bound on the value of $R_{holes}$ can be obtained by modeling the slots as a rectangular duct [19]:

$$R_{holes} = \frac{12 t_{slot} \mu_{air}}{l_{slot} w_{slot}^3} \tag{2.5}$$

The final element in the acoustic domain is the radiation impedance $Z_{rad}$. This is a complex impedance that represents the energy transferred to the medium surrounding the transducer in the form of radiated acoustic waves. This means that, in the equivalent circuit, the energy dissipated by the real part of $Z_{rad}$ is not actually lost, but rather radiated away. A good radiator has the value of $Re\{Z_{rad}\}$ as close as possible to the air acoustic impedance $Z_0$. The imaginary part of $Z_{rad}$ models the portion acoustic energy that is transferred back and forth between the medium and the transducer through the inertia of the mass of the medium. In a denser medium, like water, the effect can be quite important, and $Im\{Z_{rad}\}$ can significantly shift the resonance frequency of the transducer. Generating an analytical formulation of $Z_{rad}$ is not easy and often not possible. Generally, for a flexural transducer the value of $Z_{rad}$ is approximated by the one of a piston in an infinite baffle. The piston is characterized by an effective radius $a_{eff}$, which in our case is given by $\sqrt{A_{eff}/\pi}$.

The expression of $Z_{rad}$ of the equivalent piston in air, measured in $Ns/m^5$, is given by:

$$Z_{rad} = Re\{Z_{rad}\} + Im\{Z_{Rad}\} = \frac{\rho_{air} c_{air}}{\pi a_{eff}^2}[1 - \frac{J_1(2ka_{eff})}{ka_{eff}} + j\frac{S_1(2ka)}{ka_{eff}}], \tag{2.6}$$

where $J_1$ is the first order Bessel function of the first kind, and $S_1$ is the first order Struve function.

In the next sections, we will show that as long as the plate thickness and area are scaled together, in the electrical domain the reactive parameters of the pNUT -and of flexural resonators in general- remain constant. However, the same scaling dependence does not hold for the parameters in the acoustic domain. The dependence of these parameters with respect to the device total thickness is presented in Fig. 2.5.

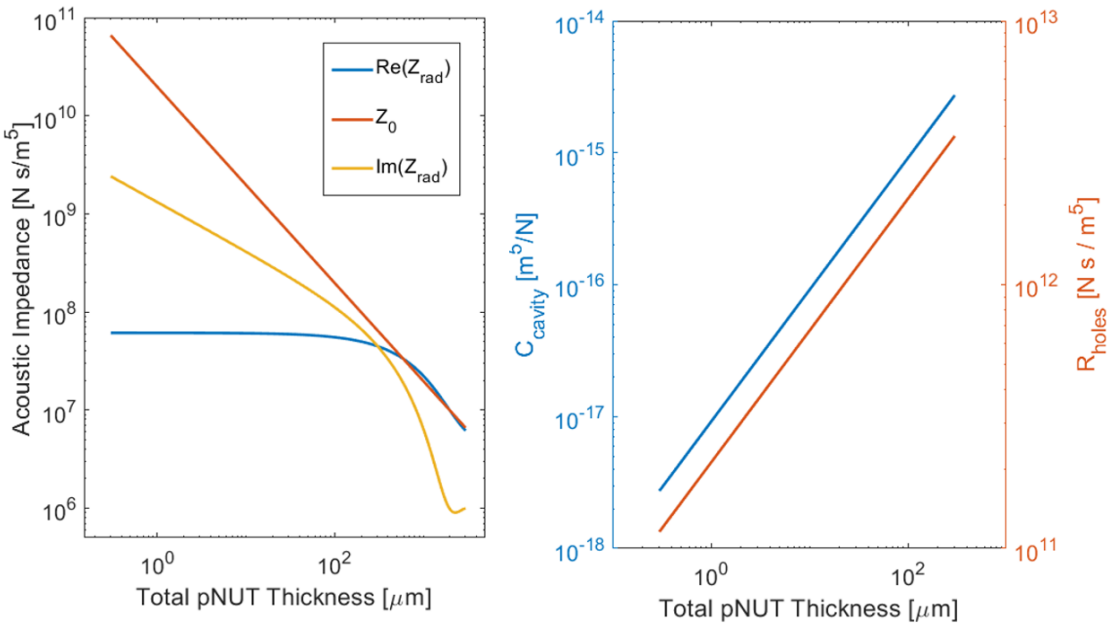


**Figure 2.5** Acoustic parameters values when scaling up the thickness and area of the pNUT. The starting point is a device with 300 nm thickness and an area of 100 µm X 100 µm. To estimate $Z_{rad}$, we assume a frequency of 50 kHz. We notice that scaling up the total thickness to 3 cm would not be feasible in practice, and the plots are only meant to illustrate the equivalent parameters dependence on geometry.

From the figures, we see that for a small radiator as the case of the pNUT, there is a large mismatch between the radiation impedance and the acoustic impedance of air $Z_0$. As the device dimensions are increased, they get closer to the acoustic wavelength at 50 kHz ( the reference frequency used to generate the plots in Fig. 2.5), and the real part of $Z_{rad}$ ends up converging to the value of $Z_0$. The value of $Im(Z_{rad})$, which is negligible compared to the mass of the transducer at all frequencies because of the small mass density of air, ends up converging to zero as the device is scaled up. When the device operates at resonance, its equivalent circuit looks purely resistive. If $Re(Z_{rad})$ was the only resistive component when the device is 300 nm thick, we would observe very high quality factors and a great mismatch with the impedance of air $Z_0$. As shown in Fig. 2.12, and experimentally in Chapters 5 and 6, the pNUTs present values of quality factors similar to those reported for much larger pMUTs operating at similar frequencies. The reason is that the way $Z_{rad}$ is calculated does not take into account the viscosity of the medium ([20]), which is the main

energy loss mechanism for highly scaled micro-structures [21][22].

As mentioned above, the value of $R_{holes}$ represents an upper bound on the range of possible values. For $C_{cavity}$ we assume that the undercut necessary to release the devices remains constant across the scaled geometries at 30 µm. This means that the depth of the back-cavity stays constant, and the total volume is increased only by the area scaling up with the total thickness of the film stack. For both $C_{cavity}$ and $R_{holes}$, higher values are desirable. Because the value of $C_{cavity}$ is only $3e-18\frac{m^5}{N}$ for the 300 nm thickness case, the device response to ultrasound will be considerably stiffened, reducing the sensitivity and shifting the resonance frequency above the target range of 30-100 kHz. As explained in Chapter 3, this issue is solved by adding a back-etch step to the fabrication process to open the cavity. For simplicity, and within the limits of the lumped equivalent circuit model, opening the cavity (i.e. the value of $C_{cavity}$ goes to infinity) we remove $R_{holes}$ from the equivalent circuit since its presence would not affect the electrical response of the pNUT.

### 2.1.3 Mechanical Domain

We now look at the variables that govern the frequency response dictated by geometrical and material properties. We derive the equations for a 4-Beams pNUT, and show that the values of the reactive parameters are preserved when thickness and area of the devices are scaled simultaneously.

Due to the large number of variables in the following equations, the variables description can be found in the nomenclature section, along with the variables used throughout the document.

#### 4-Beam pNUT Equivalent Parameters

The lumped equivalent model of the 4-beam pNUT can be thought of as 4 parallel springs connected to a common central mass. The value of the individual springs is here approxi-

mated as the one of a beam with clamped-free boundary conditions (i.e. a cantilever).

Since we are dealing with a laminate beam, the first step of the derivation is to obtain the flexural rigidity $D$ and the effective surface $\mu_{eff}$ mass density of the stack. The expressions for these two quantities can be found in [23]. Since we are approximating the beams as cantilevers, we take their normalized mode shape ([24], pp.139) as:

$$Y_{CF}(x) = 1 - cos(\frac{\pi x}{2}) \tag{2.7}$$

where $x$ is the normalized coordinate along the length of the beam. From the mode shape, it is possible to obtain the equivalent parameters $M_{eq}$, $K_{eq}$, and $\eta$:

$$M_{eq} = 4\mu_{eff} W_b L_b \int_0^1 Y_{CF}(x)^2 dx + \mu_{eff}(L_b - W_b)^2 \tag{2.8}$$

$$K_{eq} = 4\frac{DW_b}{L_b^3} \int_0^1 \left( \frac{d^2 Y_{CF}(x)}{dx^2} \right)^2 dx \tag{2.9}$$

$$\eta = 4e_{31,eff}(z_n - z_{piezo})\frac{W_b}{2L_b} \int_{x_{el}} \frac{d^2 Y_{CF}(x)}{dx^2} dx \tag{2.10}$$

$M_{eq}$ is an inertial term that measure the device ability to store kinetic energy. Similarly $K_{eq}$ represents the pNUT ability to store potential energy when the beams are deformed. Together, $M_{eq}$ and $K_{eq}$ define the dynamics of a 1-dimensional second order system that matches the displacement experienced at the tip of the beams and over the central plate. The role of $\eta$ is to provide a proportionality factor to link the displacement set by the mechanical parameters with the voltage produced across the electrodes through the inverse piezoelectric effect. The value used to model $e_{31,eff}$ for AlN is $-0.75 C/m^2$ ([25] pp.442).

In the 4-beams pNUT geometry, for a given $A$, the values of $L_b$ and $W_b$ are not independent since once we fix the length of a beam the width will automatically occupy the remaining portion of the device side. For example, in a 100 µm x 100 µm pNUT, if we fix the beam length to be 70 µm, the width will automatically be set to be approximately 30 µm (as we want to keep the holes between beams to a minimum). Once we fix the value of A and the relative length of the beams we can see that both $L_b$ and $W_b$ scale with $\sqrt{A}$. Therefore, we can extract how the parameters derived above vary as we scale the device thickness and area simultaneously (Fig. 2.6).

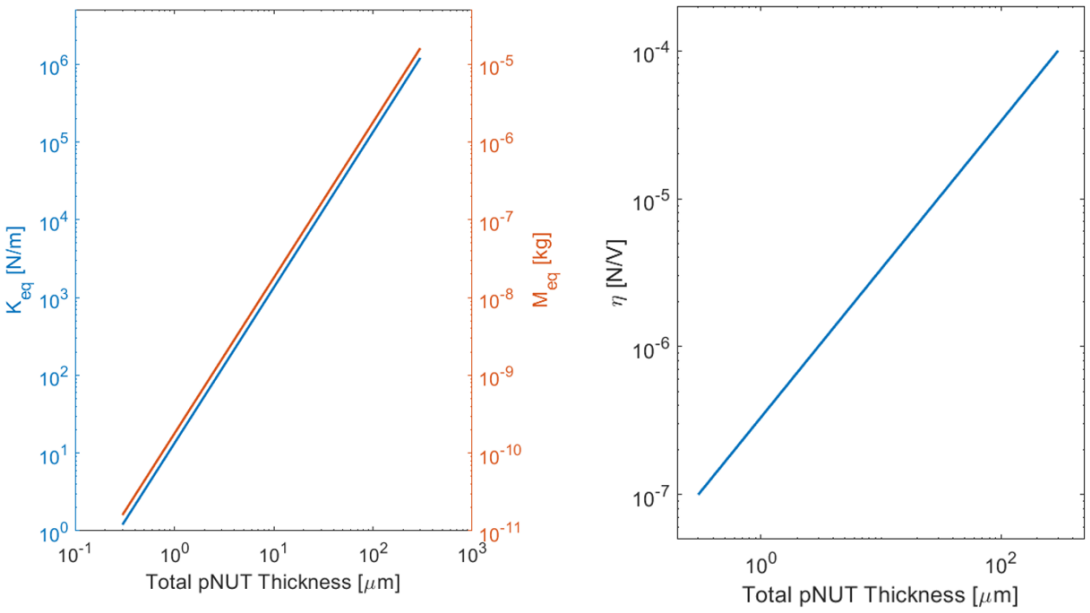


**Figure 2.6** Dependence of $K_{eq}$, $M_{eq}$, and $\eta$ on thickness and area scaling. $K_{eq}$ and $M_{eq}$ both scale quadratically with the geometrical parameters, indicating that the resonance frequency remains constant. $\eta$ increases linearly with the resonator scaling.

We see that as we scale down thickness and area, the value of $\eta$ decreases proportionally. This is because of $\eta$ dependence on the distance between the center of the piezoelectric layer and the laminate neutral axis. This quantity is represented by $(z_n - z_{piezo})$, and is proportional to the total stack thickness. As shown in the next section, the fact that $\eta$ decreases with scaling does not reduce the out-of-resonance sensitivity of the devices, as it

results in the equivalent circuit reactive parameters to remain constant once moved over to the electrical domain. In other words, the dependence of $M_{eq}$, $K_{eq}$, and $\eta$ on the total stack thickness cancels out when we move all parameters in the electrical domain.

### 2.1.4 Purely Electrical Equivalent Circuit and Scaling Relations

The electrodes capacitance can be written as

$$C_{el} = \epsilon_0 \epsilon_r \frac{A_{el}}{t} \tag{2.11}$$

Starting from the equations derived above we can obtain an expression of the components in the acoustic and mechanical domain once they are moved over to the the electrical domain, allowing us to describe the behaviour of the system purely in terms of electrical quantities. The transformed, purely electrical equivalent circuit is shown in Fig. 2.7.

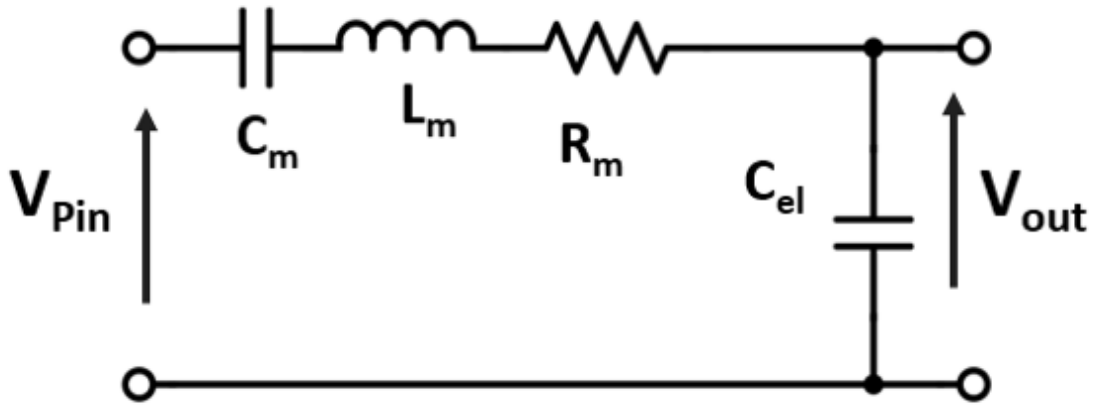


**Figure 2.7** Equivalent circuit model of the pNUT once we move all components over to the electrical domain. In this model we are assuming an open back-cavity is present, which allows us to remove $C_{cavity}$ and $R_{holes}$ from the circuit.

To move elements from one domain to another we use the following relations:

$$L = \frac{M}{\eta^2}, \quad C = \frac{\eta^2}{K} \tag{2.12}$$

Therefore, the proportionality relation of the components in the electrical equivalent model with respect to the device thickness and area are

$$\eta \propto t, \quad A_{eff} \propto A \tag{2.13}$$

$$V_{Pin} = P_{in}\frac{A_{eff}}{\eta} \propto \frac{A}{t} \tag{2.14}$$

$$L_m = \frac{M_{eq}}{\eta^2} \propto \frac{tA}{t^2} = \frac{A}{t} \tag{2.15}$$

$$C_m = \frac{\eta^2}{K_{eq}} \propto \frac{At^2}{t^3} = \frac{A}{t} \tag{2.16}$$

$$C_{el} \propto \frac{A}{t} \tag{2.17}$$

$$f_0 \propto \frac{t}{A} \tag{2.18}$$

The value of $R_m$ is given by:

$$R_m = \frac{1}{Q_{air}}\sqrt{\frac{L_m}{C_m}} \tag{2.19}$$

From these proportionality relations it is possible to see that as long as area and thickness of the device are scaled together, the out-of-resonance frequency response governed by the structural parameters of the device remains constant. At resonance, the circuit is purely resistive and the response is set by $R_m$. Since $C_m$ and $L_m$ remain constant with scaling, the value of $R_m$ is determined by the quality factor in air $Q_{air}$. The role played by $Q_{air}$ and how

scaling affects its value will be discussed in the next section. Notice that the relations hold for both the circular diaphragm [16] and 4-beam pNUT geometries, and are applicable to flexural resonators in general.

As discussed in [26], the first step to observe this scaling trend in literature consists in normalizing the reported sensitivities by the quality factor of the main resonance mode. This normalization accounts for the fact that transducers operating at different frequencies present significant differences in how air damping affects their response at resonance, therefore normalizing for differences in $R_m$ . Next, we observe that most published work presents the Tx sensitivity of the transducers, measured in $nm/V$, rather than the Rx sensitivity, as it is easier to measure. For this reason, we take advantage of the proportionality relations 2.20 and 2.21 to obtain a coefficient that is proportional to the Rx sensitivity starting from the Tx sensitivity figures reported in literature.

$$Tx_{Sensitivity} = \frac{d}{V} \propto \frac{F_{eq}\eta}{K_{eq}F_{eq}} \propto \frac{At}{t^3} \propto \frac{A}{t^2} \tag{2.20}$$

$$Rx_{Sensitivity} = \frac{V_{out}}{P_{in}} \propto \frac{F_{eq}}{\eta P_{in}} \propto \frac{A}{\eta} \propto \frac{A}{t} \tag{2.21}$$

From these relations, a coefficient proportional to the Rx sensitivity is obtained by taking the reported Tx sensitivities and multiplying them by the piezoelectric layer thickness. We finally normalize the coefficient by the transducers area in order to obtain a coefficient that depends on only one geometrical parameter. Fig. 2.8 shows a survey of AlN pMUTs from published works, and it is possible to observe the inverse linear dependence of the derived coefficient with the thickness of the piezoelectric layer.

The works referenced in Fig. 2.8 with the respective data is presented in Table 2.2. The fact that this trend emerges from literature data serves as a confirmation that the proportionality relationships outlined above are correct, and are equally valid for classic

pMUTs, pNUTs, and flexural resonators in general.

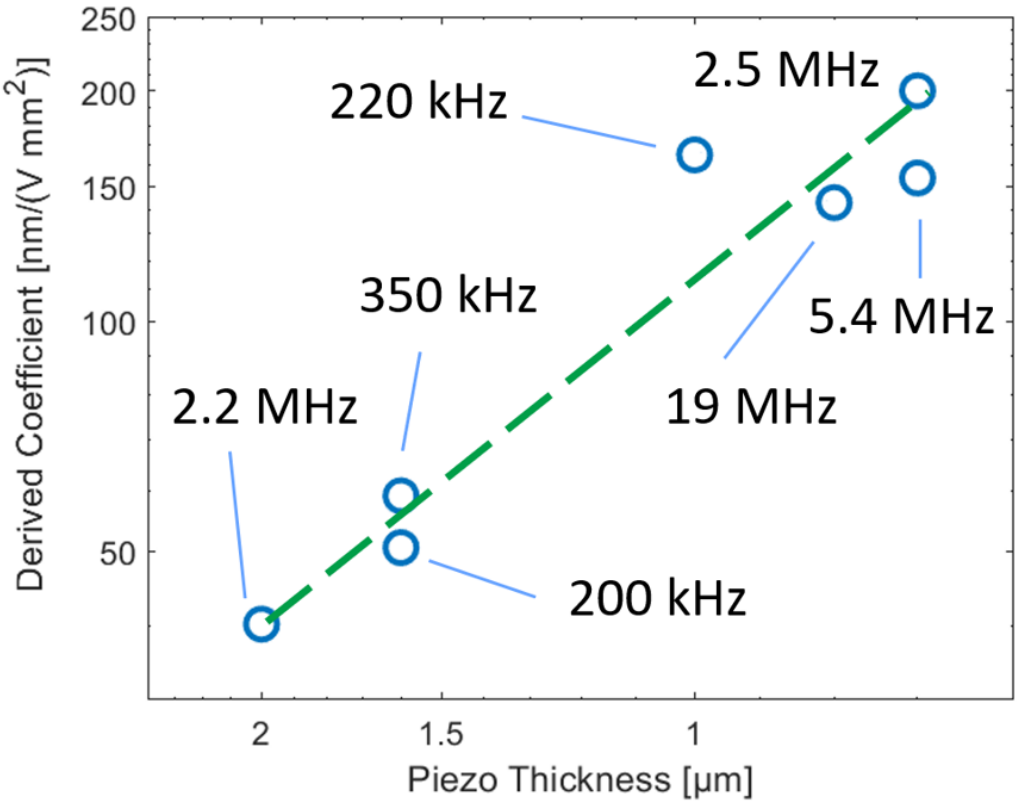


**Figure 2.8** Linear dependence on plates thickness of the derived coefficient proportional to the static Rx sensitivity in works from literature.

### 2.1.5 Quality Factor Scaling

In the previous section we showed that all values of the components in the purely electrical circuit are independent from scaling with the exception of $R_m$. The dependence of $R_m$ value on scaling depends on the quality factor of the transducer. In flexural resonators operating in air, air-damping is typically the main loss-mechanism. As the plates move in the fluid, part of the energy in the plate is passed to the medium either in form of radiation (represented by $Re(Z_{Rad})$), or in the the form of viscous losses. In fact, the expression of the radiation impedance that was shown in Section 2.1.2 was derived assuming a continuum non-viscous medium. When making this assumption we can neglect the tangential component of the

**Table 2.2** Compiled data used to generate the data in Fig. 2.8

| **TxS [nm/V]** | **Q** | $f_{res}$ **[Hz]** | **Radius [µm]** | **Area** $[mm^2]$ | **Piezo/Total Thickness** | **Comments** | **Ref** |
|---|---|---|---|---|---|---|---|
| 30 | 60 | 2.5e6 | 40 | 5e-9 | 0.7/1.4 | | [27] |
| 20 | 100 | 5.4e6 | 29 | 2.6e-9 | 0.7/1.4 | | [27] |
| 430 | 25 | 200e3 | 230 | 1.7e-7 | 2*0.8/2.4 | Double piezo | [28] |
| 452 | 42 | 350e3 | 170 | 9.1e-8 | 2*0.8/2.4 | Double piezo | [28] |
| 45 | 40 | 2.2e6 | 95 | 2.8e-8 | 2/3.3 | Curved plate | [29] |
| 400 | 50 | 220e3 | 175 | 9.7e-8 | 1/2.1 | | [30] |
| 20 | 140 | 19e6 | 25 | 2e-9 | 0.8/3.3 | | [16] |

medium velocity. As discussed in [20] (pp. 440), when the medium is considered to be viscous, the tangential components of the fluid velocity cause a disturbance in the pressure field, but they do not extend to the far field. In other words, this energy transfer from the transducer to the medium results in heat dissipation. An overview of various models used to estimate air damping in cantilever beams that account for the medium viscosity through the Navier-Stokes equations can be found in [31]. In the derivation presented in the previous section, the quality factor normalization is applied in order to compare transducers operating at different frequencies. However, if we fix the operational frequency, the quality factor of an ultrasound transducer is affected by the mass and geometry of the device as well. Although the particular geometry of the transducer has an effect on it experiences air-damping, we can gain insights on the quality factor scaling by looking at the expression of losses in cantilevers, which has been extensively characterized [32]:

$$\phi_{air} \approx \frac{AP_{atm}}{m\omega}\sqrt{\frac{M}{RT}} \tag{2.22}$$

in Eq. 2.22, $\phi_{air} = Q_{air}^{-1}$ is the loss due to air damping, $A$ is the cantilever area, $P_{atm}$ is the atmospheric pressure in the gas, $m$ is the total mass, and $\omega$ is the frequency of vibration. The terms under the square root are the gas constant, the gas temperature, and the gas molar mass ($R$,$T$, and $M$ respectively). It is worth noting that this expression does not make a distinction between the damping resulting from heat dissipation and acoustic radiation. We can then use this expression to see how the losses we observed experimentally (presented in Chapter 5) would scale with the geometry. In general, we can expect the impedance of a radiator to be close the matching condition with the surrounding medium provided the dimensions are comparable to the wavelength of the operational frequency. Interestingly, we see that as the transducer dimensions are scaled up using the proportionality dependence of Eq. 2.22, the pNUT resistance ends up following closely the theoretical value of the radiation resistance calculated in Section 2.1.2 for a circular piston in an infinite baffle (Fig. 2.9).

A possible interpretation of this convergence is that as the transducer dimensions are increased, there is a transition from a region where viscous losses dominate to a region where losses are dominated by radiation to the far field, where the device resistance is dominated by $Re(Z_{rad})$. Eq. 2.22 does not distinguish between the two loss mechanisms as it is derived directly by means of Navier-Stokes equations -which account for the medium viscosity-, while the derivation of $Z_{rad}$ explicitly neglects the role played by viscous losses. As shown in Chapter 5, the pNUTs show quality factors between 5 and 10, which are typical for pMUTs with thicknesses and areas around 10 to 100 times larger.

This points to an interesting design insight. Because of the pNUT use of the Pt electrodes as elastic layers, as well as having the central plate, the pNUTs are characterized by a much larger equivalent mass than an equivalently scaled pMUT. In theory, additional material can be added on the central plate in a separate lithographic step, further increasing the equivalent mass. From Eq. 2.22 we see that as long as we remain in the desired frequency range, the mass adjustment can be exploited to reduce the losses to maintain a high quality factor.

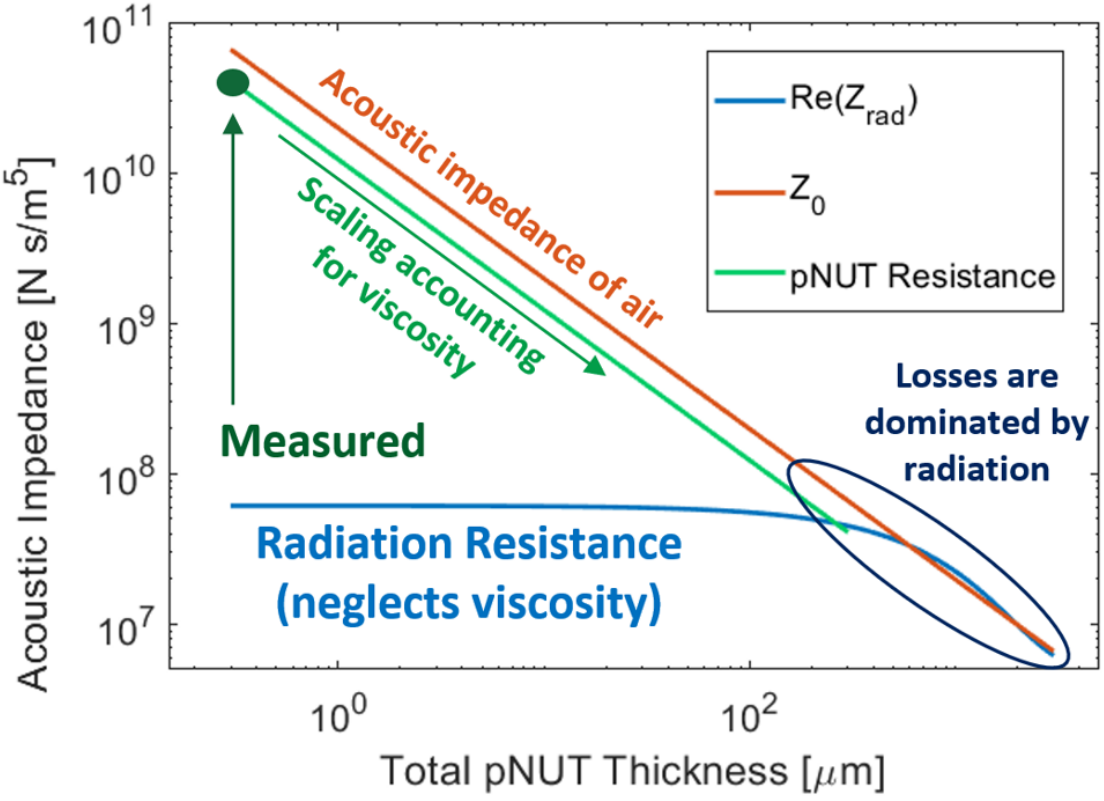


**Figure 2.9** Comparison between the scaling of the measured pNUT acoustic resistance according to models accounting for viscosity and the theoretical radiation resistance of a piston with equivalent dimensions.

It is important to notice that the use of the electrodes metal to increase the equivalent mass of the transducers is feasible only in highly scaled films, in the order of few hundreds of nm. This is because it is typically impractical to deposit and pattern much thicker metal layers through sputtering or evaporation.

### 2.1.6 The Effect of Scaling on Transducers Performance

The analysis shown at the end of Section 2.1.4 shows that the scaling relations derived for the reactive parameters is confirmed by the experimental data presented in literature. We can now combine these relations with the theory presented in the previous sections to obtain a complete analysis of the pNUT equivalent circuit response and better understand the impact of highly scaled geometries on the receive sensitivity of an ultrasonic transducer.

When the transducers operate at resonance, their impedance is purely resistive. The value of the equivalent resistive component quantifies the losses in the resonator, and its resistance value sets the value of Γ. Therefore, for a fixed area, varying Γ over a range of values between -1 and +1 is equivalent to varying the losses in the resonator in a range between zero and infinity.

The complete equivalent circuit model at resonance is shown in Fig. 2.10

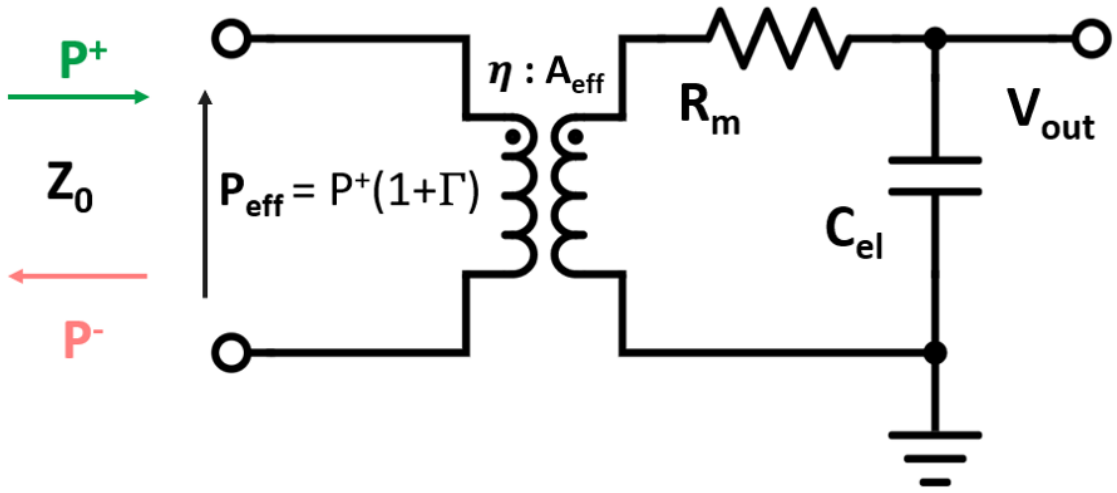


**Figure 2.10** Complete equivalent circuit model when the transducers operate at resonance.

For our scaling analysis we select a reference geometry and assign the corresponding values to $Z_0$, $\eta$, $A_{eff}$, and $C_{el}$ according to the equations derived in the previous sections. The reference geometry we choose for the pNUT is a 100 µm x 100 µm area with an AlN thickness of 100 nm and a Pt thickness of 200 nm. This geometry sets the resonance frequency to 50 kHz. Since we do not know $R_m$, which is set by the quality factor, we sweep its value over a range that generates values of Γ ranging from -1 to +1. We can now estimate the Rx sensitivity by setting $P^+$ equal to 1 Pa, and calculating the output voltage with respect to Γ.

This procedure can be repeated for larger transducers and it will give us an idea of how scaling affects the devices performance. To do that, we define a scaling factor $SF$. $SF$ is

a coefficient that multiplies the area and thickness of the reference geometry. Interestingly, the only parameter that changes as we vary $SF$ is $Z_0$, since we know that both the turn ratio $\eta : A_{eff}$ and $C_{el}$ -as well as the resonance frequency- remain constant with respect to scaling.

We can repeat the same analysis for any flexural resonator geometry (assuming it is possible to overcome some of the issues highlighted in section 2.2 for other geometries). For example, we can use the equivalent circuit data reported in [33] to generate a pMUT with a resonance frequency of 50 kHz and an area of 100 µm x 100 µm, and observe how its Rx sensitivity changes with respect to $SF$ and $\Gamma$. More details on this model, including a MATLAB script to perform the analysis, are presented in Appendix A. The Rx sensitivity for the reference pNUT and the reference pMUT with respect to scaling is presented in Fig. 2.11.

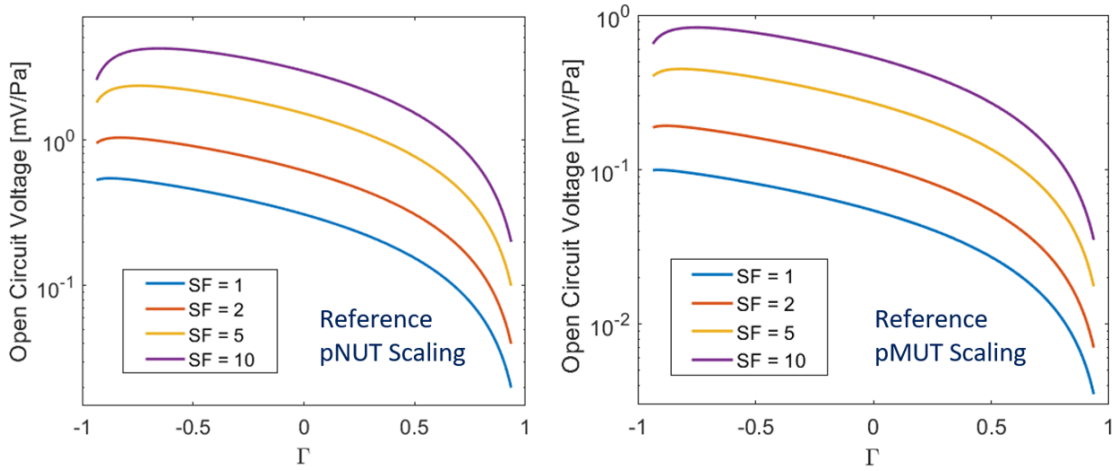


**Figure 2.11** Value of the theoretical open-circuit Rx sensitivity vs. $\Gamma$ for the reference pNUT and pMUT. Both devices have a resonance of 50kHz and an area of 100 µm x 100 µm when $SF = 1$.

The first insight that emerges from this analysis is that scaling is detrimental to the Rx sensitivity regardless of the transducer of choice. This is in agreement with the fact that as we reduce the transducer area, the total available acoustic energy decreases. In this model there are two main mechanisms that determine how efficiently we convert the acoustic energy

into an electrical signal across the electrodes. The two mechanisms are the level of matching between $Z_0$ and $R_m$ and the amount of losses represented by $R_m$. In Fig. 2.11 we see that, for the values of $SF$ under consideration, as $\Gamma$ becomes more negative the Rx sensitivity does not change significantly, while as it becomes more positive it quickly decreases. In the first case these two mechanisms compensate for each other, which means that despite the mismatch between $Z_0$ and $R_m$ increases ($\Gamma$ is more distant from 0), the losses introduced by $R_m$ decrease. In the second case these two mechanisms both contribute to waste energy: the transducer is both mismatched to the medium and lossy.

This model offers a straightforward way to compare the performance of different ultrasound sensors geometries and topologies. Once we fix the transducer area and its resonance frequency, all the other properties are automatically set. This includes the layers stack thickness, $Z_0$, the equivalent transformer ratio $\eta : A_{eff}$, and $C_{el}$.

This idea is presented in Fig. 2.12.

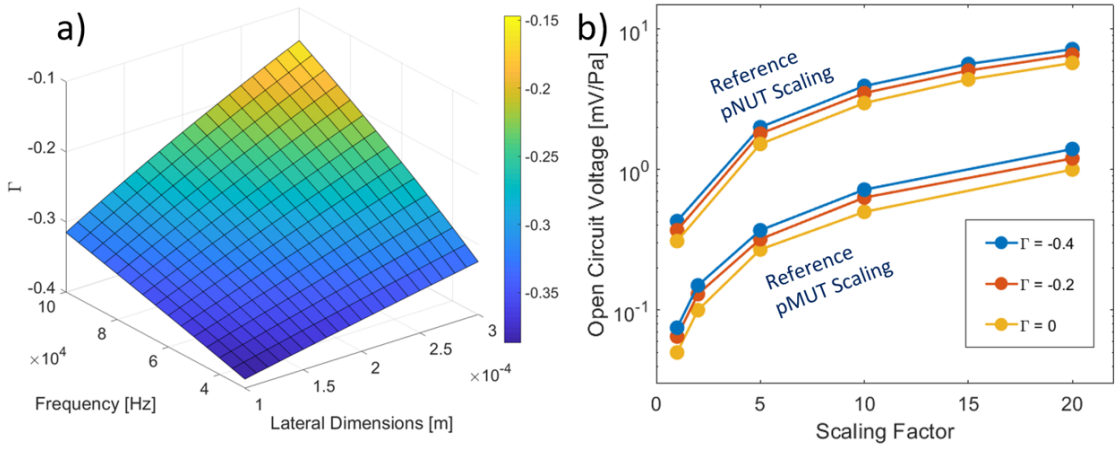


**Figure 2.12** a) Values of $\Gamma$ expected over a range of device lateral dimensions and frequencies of operation. b) Comparison between the Rx sensitivities of the reference pNUT and pMUT as they are scaled.

In Fig. 2.12a we take the value of $R_m$ we measured (presented in Chapter 5) as a reference point, and we scale its value according to the theoretical scaling of $Q_{air}$ presented in Section 2.1.5 (code included in Appendix B). This allows us to define a reasonable interval

of values for Γ. We see that Γ is always larger than -0.4 as we scale up the transducer. We can also reasonably assume that as the transducer dimensions are increased its impedance at resonance will match the one of air, corresponding to $\Gamma = 0$. Therefore we consider an interval of values for Γ between -0.4 and 0. Fig. 2.12b shows the corresponding Rx sensitivities in this Γ interval as we scale the reference pNUT and pMUT. Clearly, the pNUT geometry offers approximately an order of magnitude better performance compared to traditional pMUTs. This property makes the pNUTs ideal for building miniaturized ultrasound receivers, as the significantly higher performance per unit area compensates for the lower acoustic energy available for smaller footprints.

## 2.2 Limits of the Analytical Model

To verify the analytical model formulated in the previous section, we can check the values of the first mode resonance frequency and of the equivalent parameters through finite element analysis (FEA) in COMSOL. The first step is verifying that the analytical models apply to a single cantilever. We consider a laminate beam formed by an AlN and a Pt layer with equal thickness. The beam has fixed length of 70 µm and width of 30 µm, while we vary the thickness of the two layers to observe how its properties scale. In particular, we can observe the resonance frequency of the beam, which ties the relation between $K_{eq}$ and $Meq$, and the static tip displacement per unit voltage, which ties the relationship between $K_{eq}$ and $\eta$ (for 1 V actuation the displacement is equal to $\eta/K_{eq}$). The comparison between the analytical model and COMSOL for a single cantilever beam is shown in Fig. 2.13.

Now that we know the analytical model predicts well the parameters for a single beam, we can move to a complete device. We keep the beams geometry with a width of 30 µm and length of 70 µm, while we vary the thickness of the layers in the laminate. These are dimensions close to the ones used in the fabricated devices and that will be discussed in Chapter 5. For simplicity, we neglect the bottom electrode, only 20 nm in the fabricated devices, and

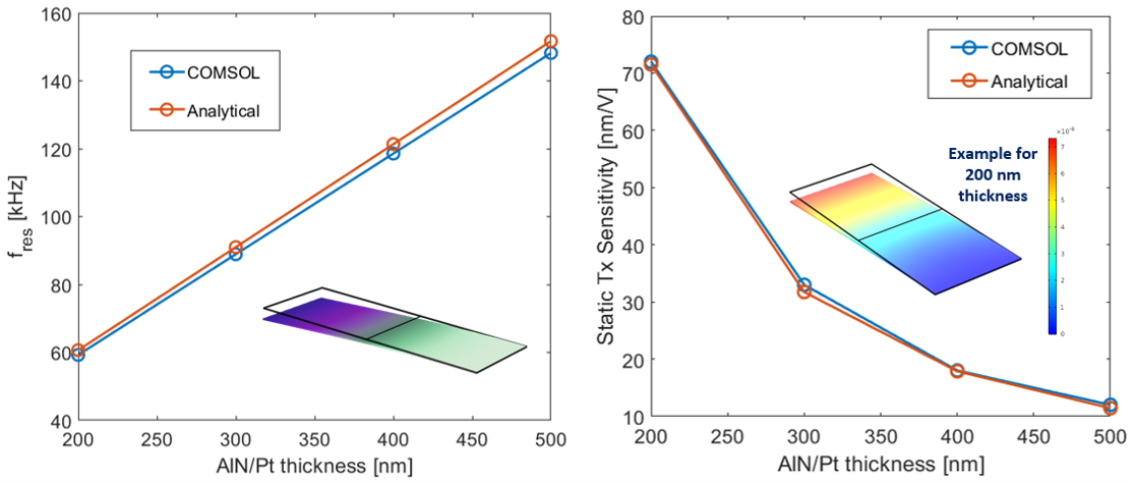


**Figure 2.13** Left: Resonance frequency of a laminated cantilever simulated in COMSOL and with the analytical model. Right: Tx sensitivity of the same cantilevers. In both cases the analytical model agrees well with the results observed in COMSOL.

assume its absence would not affect dramatically the devices mechanical dynamic response.

The first resonance mode of the device obtained from an eigenfrequency simulation in COMSOL is shown in Fig. 2.14a.

We can see that because of the common central plate, the beams are subject to a partial constraint on the angle they can have at the tip. In Fig. 2.14b we can see the mode shape obtained directly from COMSOL on the plate side of the beam, and how it compares to the mode shapes of an ideal cantilever and clamped-guided beam. The mode shape of the real device is in between the two ideal boundary conditions examples, although closer to that of a cantilever. By repeating the same analysis as above, we can see in Fig.2.15 (left) that the resonance frequency of the device observed in COMSOL is higher than the one obtained by assuming clamped-free boundary conditions on the beams. The analytical model matches the results obtained through FEA after the COMSOL mode shape is used in the analytical model. Similar results are shown on the right side of Fig.2.15. The analytical model that uses the COMSOL mode shape to obtain $\eta$ and $K_{eq}$ follows closely the static Tx sensitivity directly observed in COMSOL. On the other hand, the displacement of the pNUT obtained

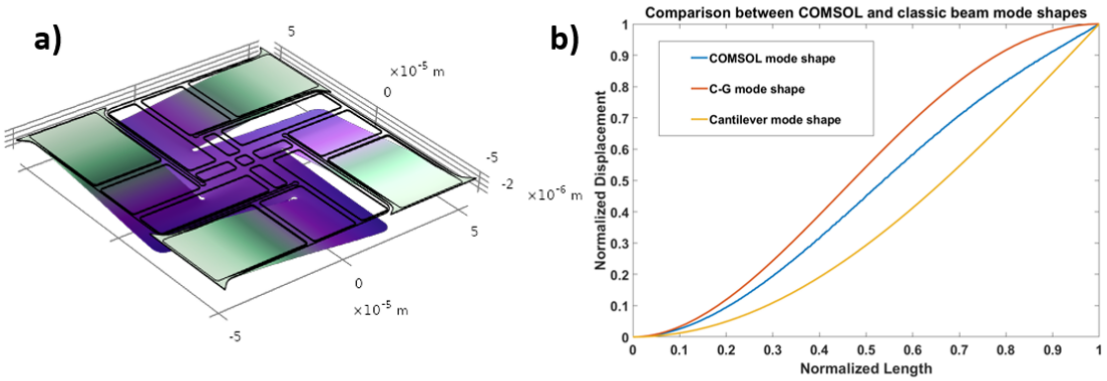


**Figure 2.14** a) Resonance Mode of a device obtained from an eigenfrequency simulation in COMSOL. b) Comparison between the device beams mode shape and mode shapes of a cantilever and a clamped-guided beam.

with the cantilever mode shape, being more compliant, is much higher than the one from the FEA model.

During the design phase, the analytical model is a useful tool to quickly establish the device parameters and get a sense of how those scale as we vary the geometry. However, as outlined in the next sub-sections, we will see that as more non-idealities are taken into account, the analysis through FEA becomes inevitable to understand how a real fabricated device will respond to ultrasound.

### 2.2.1 The Effect of the Undercut from Release

The devices fabrication process, presented in Chapter 3, uses an isotropic release step. Because of this, a certain amount of undercut will always be present, and it measures typically between 20 µm and 30 µm once the devices are completely released. When accounting for the effect of the undercut on the device, the COMSOL model must be modified as shown in Fig. 2.16.

Adding the undercut to the geometry does not change significantly the equivalent mass

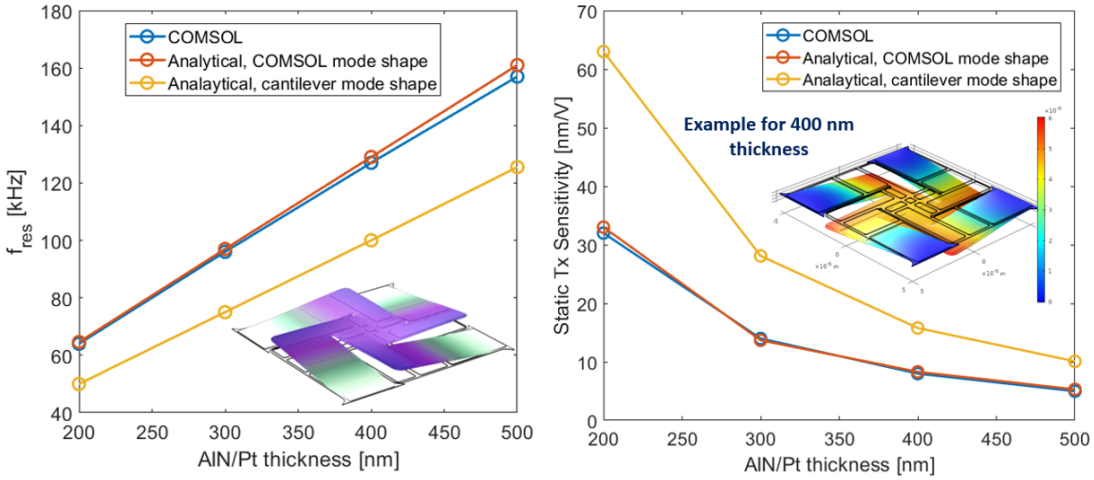


**Figure 2.15** Left: Comparison between the resonance frequency of a pNUT simulated in COMSOL and in the analytical model. Right: The same comparison for the static Tx sensitivity. In both cases the discrepancy between the analytical model and COMSOL is resolved once we use the COMSOL mode shape in the analytical model. This highlights the role of the central plate in stiffening the device response.

of the device, but it decreases $K_{eq}$ by relaxing the clamped constraint previously imposed on the anchored side of the beam. This change modifies the beams mode shape around the clamped region, reducing the amount of bending that occurs. The natural frequency of the modified structure is shown in Fig. 2.17. The model suggests that a small amount of undercut is responsible for most of the softening, while expanding the release further accounts for progressively minor changes in the resonance frequency of the device.

Another important consequence from the presence of the undercut is its effect on the transduction coefficient $\eta$. Just like $K_{eq}$, the value of $\eta$ is determined by the amount of bending that occurs in the beams clamped region (see Eq. 2.9 and 2.10), where the electrodes are located. Relaxing the ideal zero-angle constraint significantly reduces the amount of bending, reducing how effectively we convert the beam in-plane strain into an electric field. This change can be visualize in Fig. 2.18, where we show the normalized electrodes mode shapes when no undercut is present and when we have a 25 µm undercut respectively.

We can see that in the 25 µm undercut case significantly less bending occurs. In theory,

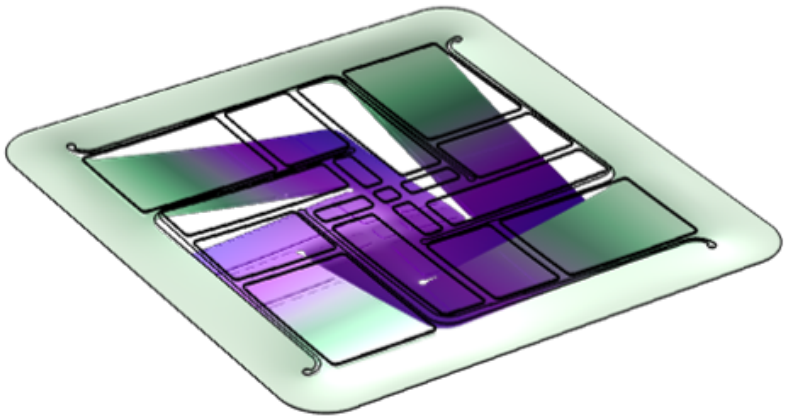

**Figure 2.16** First resonance mode of a device including a 15 µm undercut from the release process.

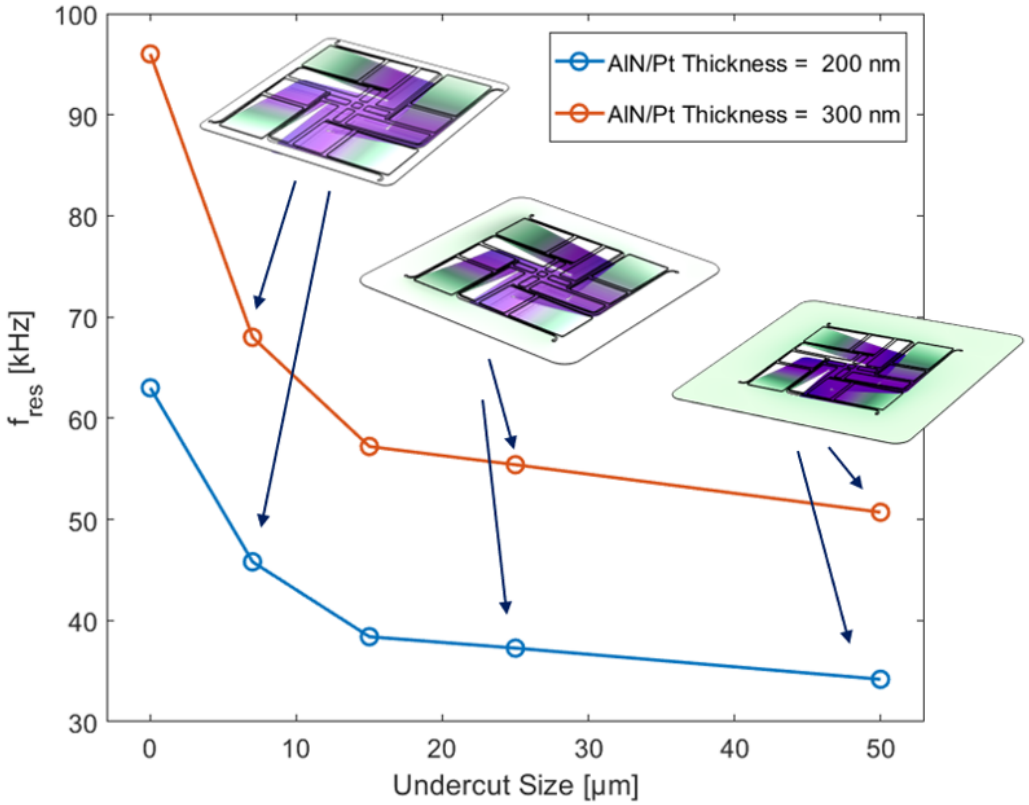


**Figure 2.17** pNUT first resonance frequency for different levels of undercut.

this reduction causes an important reduction in the transduction coefficient of about 20x. This analysis highlights the importance of developing a fabrication process that allows for

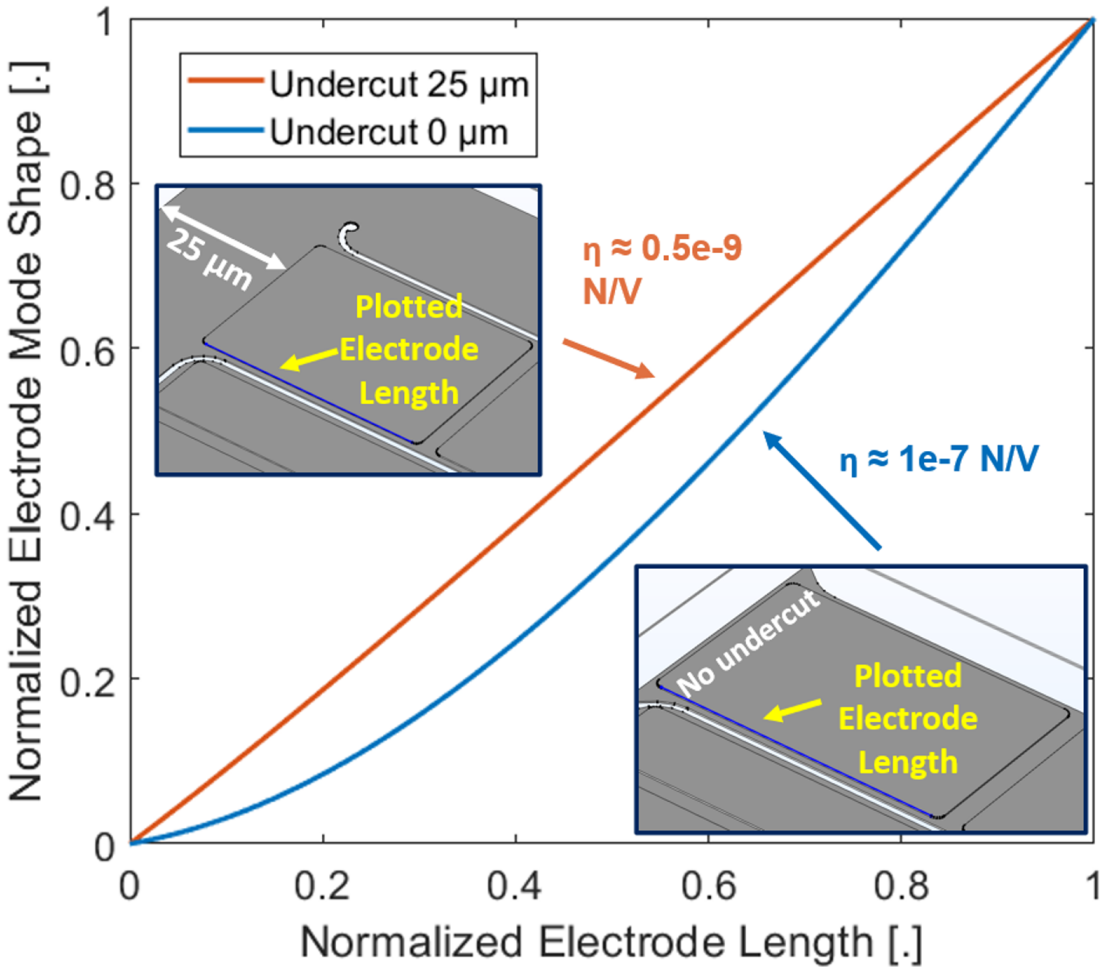


**Figure 2.18** Normalized electrode mode shapes when no undercut and when a 25 µm undercut is present. The figure illustrates how relaxing the fully clamped boundary condition affects the electrodes mode shape and the transduction coefficient $\eta$

precise control of the devices release.

### 2.2.2 The Effect of Residual Stress

Another important non-ideality that must be taken into account is the effect of the residual stress on the devices frequency response. A certain amount of residual stress from the films deposition process is inevitable. In a similar way as the undercut, the stress does not affect the equivalent mass of the resonators, but it can increase or decrease the equivalent stiffness depending on the stress being tensile or compressive, respectively. The in-plane residual

stress influence becomes increasingly dominant as the aspect ratio of the suspended plate increases. An analogy that describes this effect is that of a drum head pelt. The pelt is a high aspect ratio flexural resonator, and the pitch of the drum is not just determined by geometric and material parameters, but by the tension in the pelt as well. On the other hand, a short steel rod is a low-aspect ratio resonator, and adding tension to it does not significantly change its resonance frequency. Classic pMUTs are characterized by a circular geometry that is clamped all around. This geometry, like in the drum case, is extremely susceptible to residual stress. In fact, the fully clamped boundary condition does not allow the structure to deform to relax the stress once it is released. An analytical model that describes the dynamics of a circular plate accounting for the residual stress is described in [34]. The geometry of the 4-Beams pNUT permits to the structure to release some of the tension by deforming. The effect of residual stress on circular plates of different thicknesses and radii compared to a 200 nm thick 4-Beams pNUT is shown in Fig. 2.19.

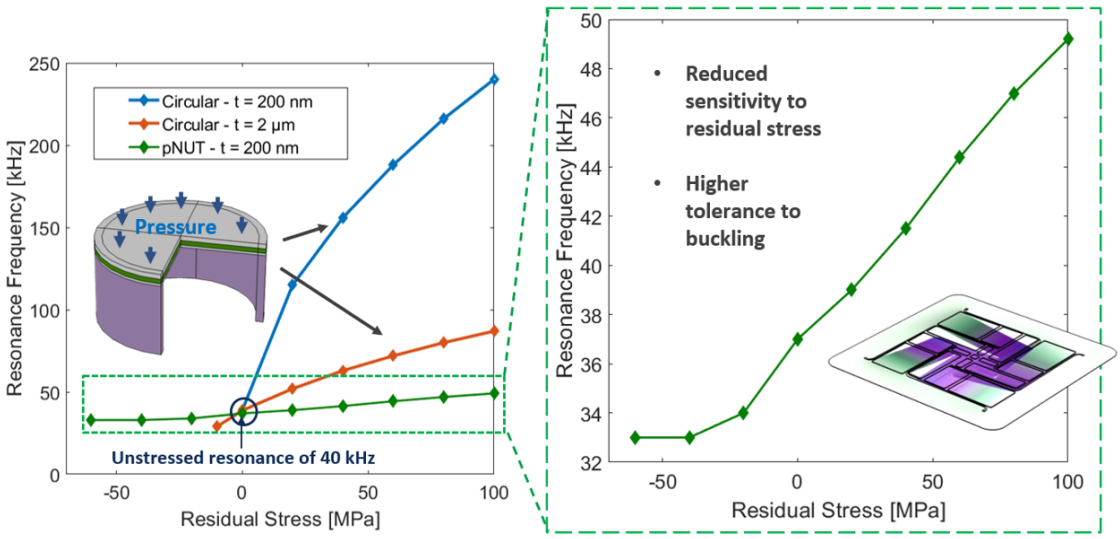


**Figure 2.19** Comparsion of the effect of residual stress on circular pMUTs and on a 4-Beams 200nm thick pNUT. The devices dimensions are selected to have an unstressed resonance frequency of approximately 40 kHz.

Besides having a reduced sensitivity to residual stress, the pNUT also has more tolerance to buckling when the residual stress is negative. While less sensitive, the pNUT resonance

frequency is still shifted by residual stress. In the case of positive residual stress, the resonance frequency is increased, partially counteracting the effect of the undercut seen in the previous sub-section.

Ideally we would prefer a zero dependence of the stiffness on residual stress. This would be achieved by a cantilever-like structure, which is clamped on only one side and can deform along all other directions to relax the stress to 0 MPa. Unfortunately, the in-plane stress distribution along the stack thickness is not uniform, especially because the structure is a laminate. This means that stress gradients along the thickness are present, which will cause the structure to bend out of plane when released. While a circular pMUT, being fully clamped, would not deform vertically, a cantilever would be completely free to curl, potentially even folding on itself. The pNUT geometry offers a compromise between these two scenarios. By only allowing partial relaxation of the residual stress we can reduce the resonance frequency shift while limiting the out-of-plane bending. This effect is evident in Fig. 3.2.

# Chapter 3

# pNUTs Fabrication

## 3.1 pNUTs Fabrication Process

The pNUTs were built in the Carnegie Mellon nano-fabrication facility with a four-masks process as shown in Fig. 3.1.

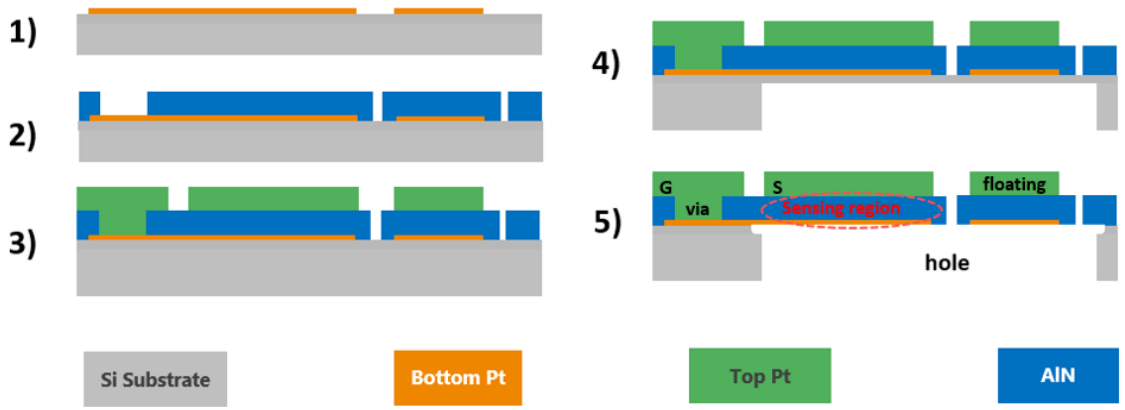


**Figure 3.1** Fabrication process of the pNUTs: 1) Bottom Pt lift-off, 2) AlN deposition and patterning, 3) Top Pt lift-off, 4) backside DRIE, 5) topside $XeF_2$ release.

In step 1) the 20 nm Pt bottom electrode is deposited and patterned through lift-off. In step 2) a 100nm thick AlN layer is sputtered in a Tegal AMS system and subsequently wet-etched in a heated CD26 developer solution. The Pt top electrode is then sputtered and lifted-off in step 3). The device release is performed through a combination of back-side and

front-side etch. First (step 4), the area of the device back-cavity is defined by a back-side Bosch etch process carried out in a STS DRIE System. The depth of the back-etch was characterized to leave about 5 to 10 µm of silicon below the device and prevent damaging it during the removal from the holder. The device release is completed in step 5) by removing the remaining silicon with a $XeF_2$ etch from the front-side.

An example of a fabricated pNUT is shown in Fig. 3.2 b, side by side with a simulated structure characterized by residual stresses of 50 MPa in the AlN layer and 1 GPa in the top Pt layer.

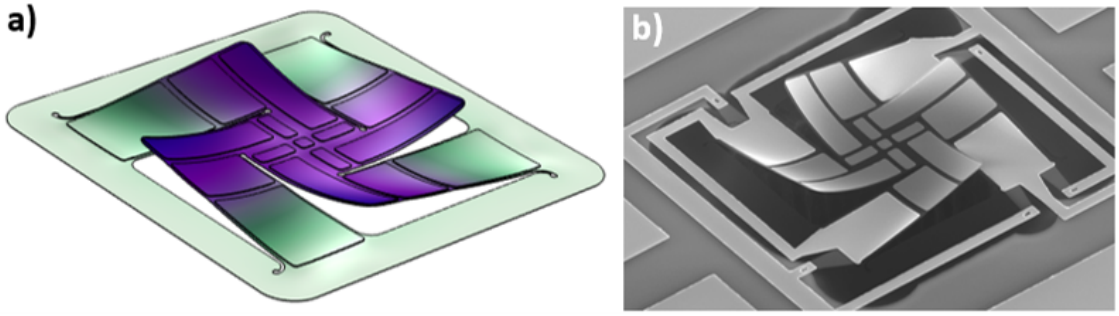


**Figure 3.2** a) Simulated structure characterized by residual stresses of 50 MPa in the AlN layer and 1 GPa in the top Pt layer. b) SEM picture of a fabricated device.

## 3.2 Fabrication Challenges

During the fabrication process several challenges were encountered. In this section we summarize them and describe possible solutions for future pNUTs fabrications.

### 3.2.1 Device Geometry Motivation

Initial prototypes of the pNUT were simple square clamped-clamped beams. An example of the layout of these devices is shown in Fig. 3.3a. Upon release, most of these devices broke due to the difficulty in controlling residual stress in extremely thin sputtered films. Additionally, even if the stress in the single layers could be controlled within ± 100 MPa, the

small thickness of the layers in the laminate produces stress gradients along the thickness of the device in the order of GPa/µm. As shown in Fig. 3.3a, the floating metal in this device variation was patterned as a continuous patch over suspended portion of the device that was not covered by the electrodes. Because of the high stress gradients in the laminate (positive in this case), the structure bent upwards, and tore along the side of the metal sheet. In the same layout we included a variation where the electrodes were split and connected in series with each other and the floating metal was segmented along the same width as the individual beams electrodes as shown in Fig. 3.3b.

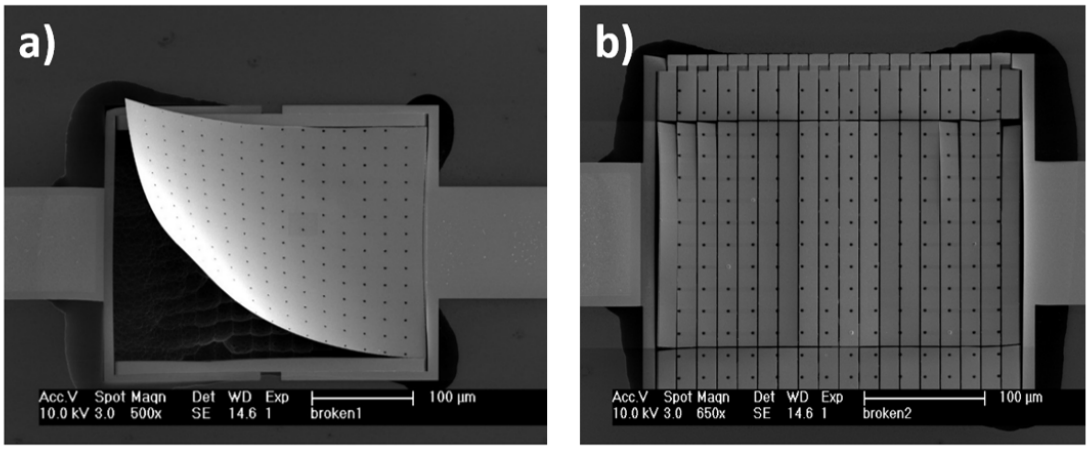


**Figure 3.3** Example of broken devices from early pNUTs prototypes. a): Device with a uniform floating metal. b) Device with segmented floating metal. It is evident how the influence of the stress gradient is reduced along the direction of the segmentation.

In the image, it is evident how the segmentation helps mitigating the bending moment along the width of the device, preventing mechanical failure along that direction. At the same time we see that along the length of the beams we still see some tearing in the plate. This observation prompted a change in the design to make sure there are always discontinuities in the patterned metal by segmenting it along both the in-plane directions to limit the influence of the bending moments resulting from the stress gradients in the stack. Another

observation is that the mechanical failure always originated at the angle of the patterned metal, that was originally designed with sharp 90 degrees angles. A sample layout of the first pNUTs prototypes is presented in Fig. 3.4a. Fig. 3.4b showcases the layout of the last generation of devices. In the image, we can see that besides being segmented, the floating metal is also characterized by rounded corners with 1 µm radius. In doing so, we prevent stress concentration points where tears typically are originated. In a similar way, we round individual beams where they attach to the substrate on the anchor side.

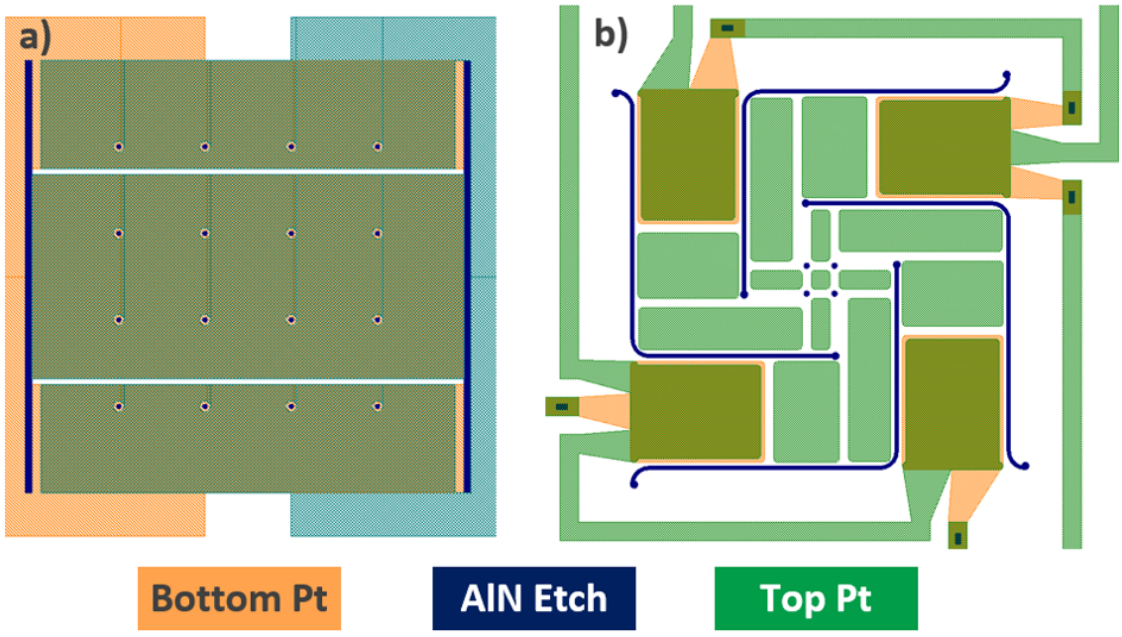


**Figure 3.4** Comparison between the first pNUTs prototypes (a) and latest version (b) layouts. We moved to the 4-beams anchor topology due to the high sensitivity to residual stress of the clamped-clamped design. Additionally, all square corners were eliminated, the top electrode dimensions were reduced by 1 µm compared to the bottom electrode, and the bottom metal was eliminated from the floating region.

In the first devices, the bottom metal was patterned even in the floating metal region. The reasoning for that choice was that it would increase the equivalent mass of the device and maintain the resonance frequency in the desired range of operation. In our last design, we kept only the top metal for the floating region, since the shift in resonance frequency was not significant, especially if compared to the variance in the equivalent stiffness introduced

by the residual stress alone. Finally, the lateral dimensions of the top electrodes were reduced by 1.5 µm compared to the bottom electrodes to limit the overlap of the two metals on the regions where the AlN is sloped along the side of the bottom metal. Since the AlN are only 100 nm to 200 nm thick, it is possible to not have perfect coverage of the bottom electrodes along its perimeter. By making the top metal electrodes slightly smaller we minimize the chance of creating a short circuit between the two electrodes. This design change is especially relevant for the following section.

### 3.2.2 Bottom Metal Lift-off

This issue is present during the first step of the fabrication process, where the bottom electrode metal is deposited and lifted-off. During a lift-off process it is common to have so called "wings" on the perimeter of the patterned metal [35]. An example of this phenomenon is shown in Fig. 3.5. Lift-off wings are problematic when working with very thin piezoelectric films as it results in device shorting.

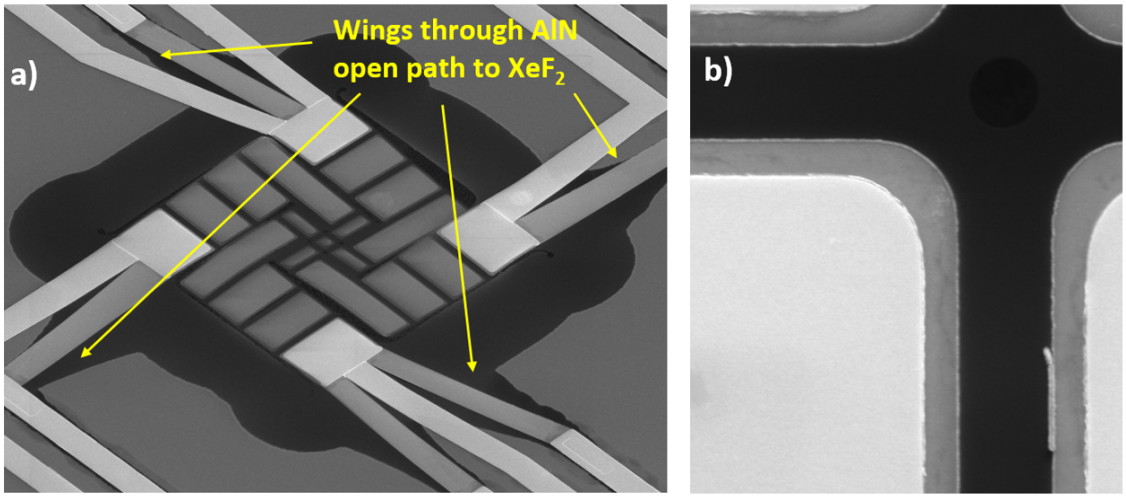


**Figure 3.5** a) Example of effect of lift-off wings in the bottom metal on the devices release. b) Close-up view of the floating metal. both on the top and bottom metal it is possible to see the wings along the perimeter of the rectangles.

This occurrence is especially common if positive photoresist is used, as it is characterized

by a positive slope angle along the sides of the developed pattern (Fig. 3.6). On the other hand, negative photoresist is expected to be more resilient to wings formation, as the negative-angled slope helps creating a sharp discontinuity in the metal film, easing access to the solvent to etch the photoresist during the lift-off [36].

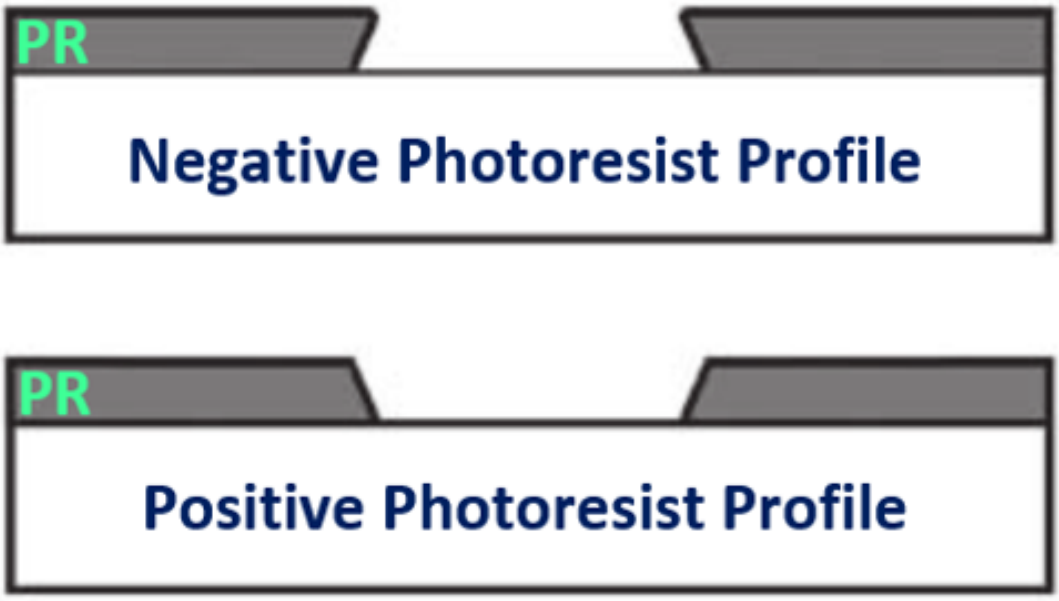


**Figure 3.6** Comparison between positive and negative photoresist profiles.

In the first round of fabricated devices, we used positive photoresist for the bottom electrode step. When we tested the finished devices, we found that almost all of them were presenting a low resistance (between 100Ω and 2kΩ) between the top and bottom electrode. While normally the wings would be covered by the dielectric between the two electrodes, because of the extremely thin piezoelectric layer that characterizes the pNUTs, they were not completely passivated by the AlN, and formed a low resistance path to the top electrode as a result. We identified the problem in the chrome (Cr) adhesion layer used for the bottom electrode. Both the chrome deposited in the CVC and in the 5-Target sputtering system were found to be extremely conformal. In fact, after further testing, even switching to negative

photoresist did not completely eliminate the wings issue. As a temporary solution, after the lift-off, we resorted to breaking the wings with a gentle swab cleaning followed by a 40 kHz sonication in acetone and a step in the spin washer. After repeating these step 3 to 4 times almost all wings were eliminated. For future fabrications, we recommend characterizing the bottom layer lithography with a lift-off photoresist, or possibly switching to the bi-layer method [36]. Another possibility might be switching to a different adhesion metal, such as titanium (Ti), although we did not verify if it is less conformal than Cr.

### 3.2.3 Aluminum Nitride Etch Issues

**Issue #1**

Multiple issues were encountered during this fabrication step. The device geometry is patterned in the AlN through a wet etch. The used etchant is a solution of CD26 developer heated to approximately 70C. The wafer is immersed in the solution for approximately 25 seconds before being rinsed in de-ionized water. During this etch step both the slots that define the beams profile and the vias to access the bottom electrode are patterned. The first issue encountered on this step is that once the wafer is removed from the CD26 and after stripping the photoresist mask, only the vias were thoroughly patterned, while the AlN on the slots seemed completely unaffected. Since the vias consist in 5 µm x 5 µm squares, while the slots are only 1 µm wide lines, we initially thought the issue was that the photoresist on the slots was underdeveloped, leaving the AlN underneath unexposed. However, in a separate test, we observed that overdeveloping the photoresist did not change the results. It is worth noting that this issue was not experienced in the first generation of devices. The only difference between the first round of devices and the later fabrications is that the Carnegie Mellon cleanroom was moved to a new facility and the shape of the container where the etch was taking place. Of course these changes should not have affected the process, and the reasons for the different outcome are still unclear.

**Issue #2**

The solution to the problem outlined above consisted in a modification to the initial fabrication process that is presented in Fig. 3.7. In this variation, we switch the order of step #2 and #3. In this way we pattern the top metal before etching the vias and the slots in the AlN, momentarily leaving the bottom electrode disconnected from the pads. Next, we do the lithography to pattern the vias and slots, and we run an etch step in the ion mill. At this point, the AlN on the slots location is exposed, while the AlN on the vias is masked by the top metal sputtered previously. Now, we time the milling to make sure we etch completely the slots AlN, and etched completely top metal on the vias location, while still leaving some AlN to mask the bottom metal under the vias. At this point we are left with the slots completely patterned, while the vias are yet to be opened. After the milling is complete. Since the vias where correctly etched in the CD26, we now place the wafer in the heated solution to etch the remaining AlN and gain access to the bottom electrode. The fabrication is finished by repeating the top metal deposition step, lifting-off a thin Pt layer (around 30 nm) to connect the pads to the bottom electrode. The modified fabrication process is showed in Fig. 3.7.

In principle this variation should have solved the problem of the slots not being correctly patterned. Once the photoresist was completely stripped, the slots were clearly visible under the optical microscope. Under higher magnification it was also possible to observe the gray color of the silicon substrate under the AlN, indicating the AlN was completely removed. However, after the DRIE step, the devices exposed to $XeF_2$ did not release. The reason for this is still unclear. Unless the issue is related to the $XeF_2$ step itself, the best explanation is that during the AlN wet etch step some residues from the etched film re-deposit in the slots, creating a passive layer on the exposed silicon. These issues are still being investigated and will be the subject of future work. To avoid these problems in future pNUTs designs, we recommend splitting the AlN etch step in two separate masks, to etch the AlN to open

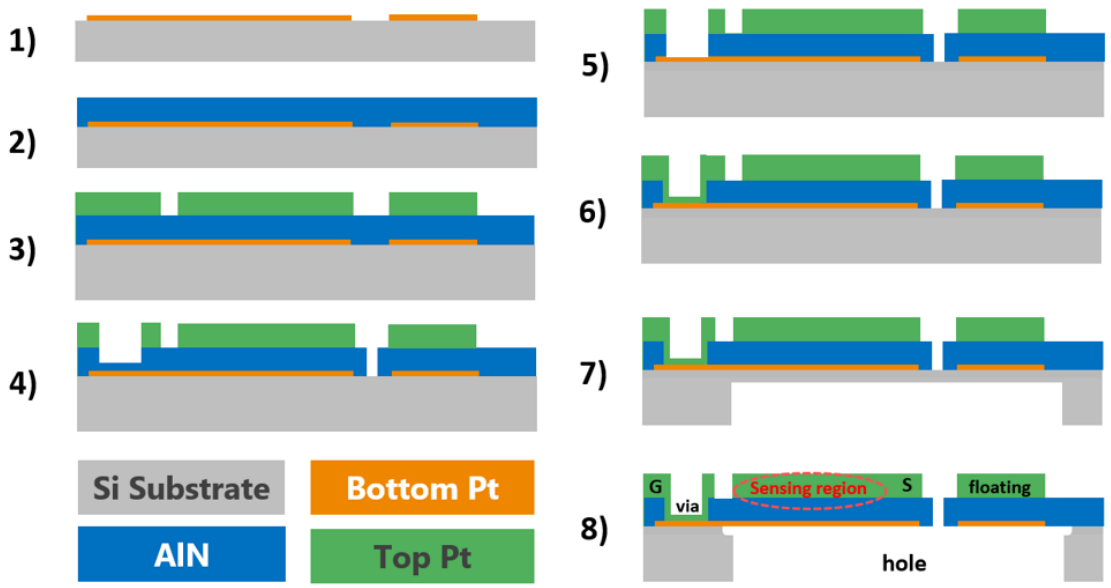


**Figure 3.7** Alternative process to solve the issue the slots not etching. 1) Bottom metal lift-off. 2) AlN sputtering. 3) Top metal lift-off. 4) Ion mill to open the slots. 5) CD26 etch to open the vias. 6) Thin metal lift-off to connect the vias. 7) DRIE. 8) $XeF_2$ release.

the vias first, and to separately mill the slots after that.

In the end, the devices were released directly from the DRIE step by etching the silicon all the way to the device layer. The issue with this approach is that the devices are extremely thin, and during the DRIE step they are in contact with an adhesive meant to keep the chip attached to a holder wafer. When the chip is removed after the etch, many devices are damaged in the process, reducing the yield significantly. Because of time constraints due to the global pandemic, we did not start a new fab aiming at increasing yields. However, we were able to find enough functional devices to validate the models presented in chapter 2 and chapter 4.

# Chapter 4

# pNUTs Arrays Modeling

The pNUTs offer an opportunity to reduce the total area of the transducer to a small fraction of current devices operating in the same frequency range. This makes the integration with electronics more practical and reduces the total size of the IoT nodes to the sub-mm range, with a consequent costs reduction. In our single device design we targeted an area of 100 µm x 100 µm. However, it is possible that for a given node specifications more real estate is available. To take full advantage of the available area we can either scale up the single device area and thickness by the same factor (to maintain a constant operational frequency), or we can build arrays of devices. If we choose to build pNUTs arrays, we must select a method to connect the devices electrodes together. Depending on the selected connection method, the electrical output of the array will vary, as well as the equivalent impedance seen from the input of the interfacing circuitry. The use of an array of devices results in greater flexibility than simply using a larger area device in setting the overall system impedance or the output voltage/current in a given form factor. This is a unique advantage of starting out from a smaller device and synthesizing arrays of pNUTs.

While a large number of connection methods are possible (depending on the size of the array), we describe here three possible scenarios, which serve different implementations and offer different advantages depending on the conditioning electronics used to detect the

electrical signal generated by the pNUTs. In the spectrum of possible methods, at the extremes we have all the devices connected in series on one side, and all the devices connected in parallel on the other one. The third scenario we consider is in the middle of the spectrum, which we call series-parallel (SP). This scenario represents a compromise between the two extremes. In a square array with a SP connection, all the devices in the same row are connected in series with each other, and the rows are connected in parallel. Schematics of the three connection methods are shown in Fig. 4.1.

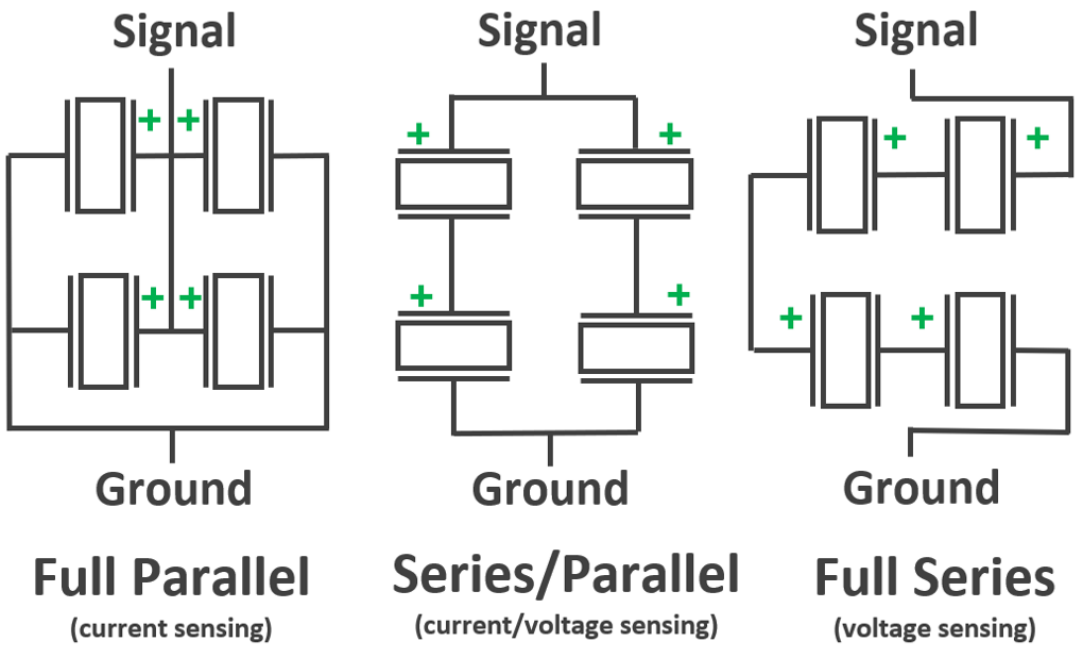


**Figure 4.1** Three pNUTs arrays connection options. From left, connection in parallel, series-parallel (SP), and connection in series.

To observe how the array properties change by varying the connection method, we build a model in the circuit simulation software ADS. The first step to build the model is to generate a cell that describes the individual device response. The cell is represented by a 2-port system, with an acoustic port input and an electrical port output as described in Chapter 2. A picture of the single pNUT cell is shown in Fig. 4.2. For simplicity, we neglect the effects of $R_{holes}$ and $C_{cavity}$, which is appropriate since in the fabrication process we

included the backside etch step to have an open cavity.

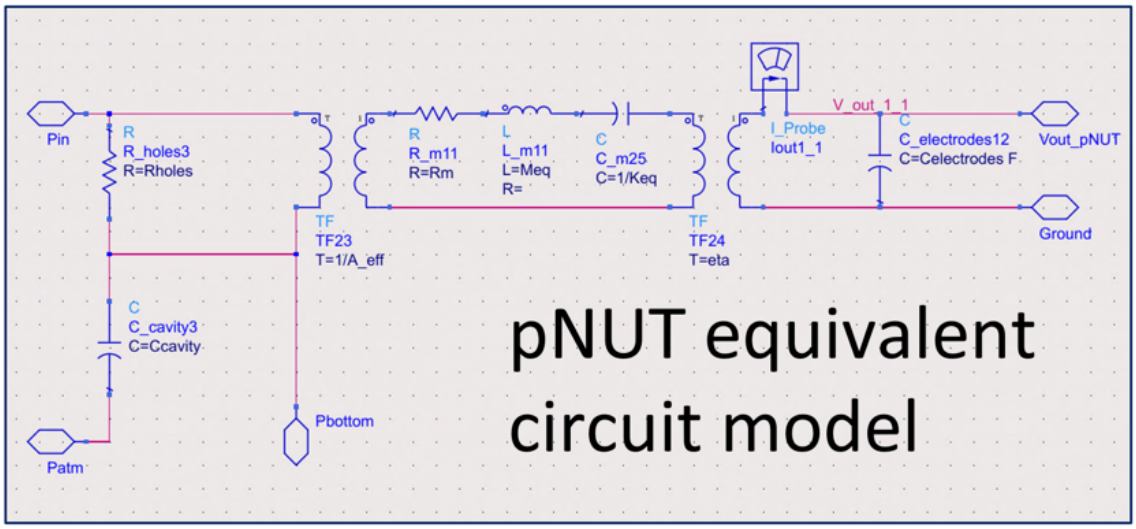


**Figure 4.2** Equivalent circuit model used in ADS to represent a single pNUT within an array.

Once we have functioning single cells, we can use them as instances (building blocks) in ADS, and start connecting them together with the desired connection method. We note that we only have control over the way we connect the electrical port of the cell (i.e. the terminals of $C_{el}$). When incident ultrasound is present, all the devices in the array are experiencing the same acoustic pressure regardless of the connection method. Therefore, in the model, all the acoustic ports are connected to the same acoustic pressure source (see Fig. 4.7a for an example). We can now take a look at the possible connection topologies and the corresponding electrical responses.

## 4.1 Methods of Connection of pNUT Arrays

As a sample individual pNUT, we use the equivalent parameters listed in Table 4.1, which deliver a resonance frequency of 50 kHz.

To study the device response, we run an AC simulation, while applying an acoustic pressure of 1 Pa at the single cell input and sweeping it between 40 kHz and 60 kHz. The

**Table 4.1** Parameters used in the single cell pNUT used to build the arrays model.

| $K_{eq}$ | $M_{eq}$ | $Q$ | $\eta$ | $A_{eff}$ | $C_{el}$ | $P_{in}$ | $R_{holes}$ | $C_{cavity}$ |
|---|---|---|---|---|---|---|---|---|
| $9[\frac{N}{m}]$ | $9e-11[kg]$ | $11[.]$ | $8e-8[\frac{N}{V}]$ | $7e-9[m^2]$ | $2.4[pF]$ | $1[Pa]$ | *Open* | *Short* |

single device open-circuit voltage response is shown in Fig. 4.3.

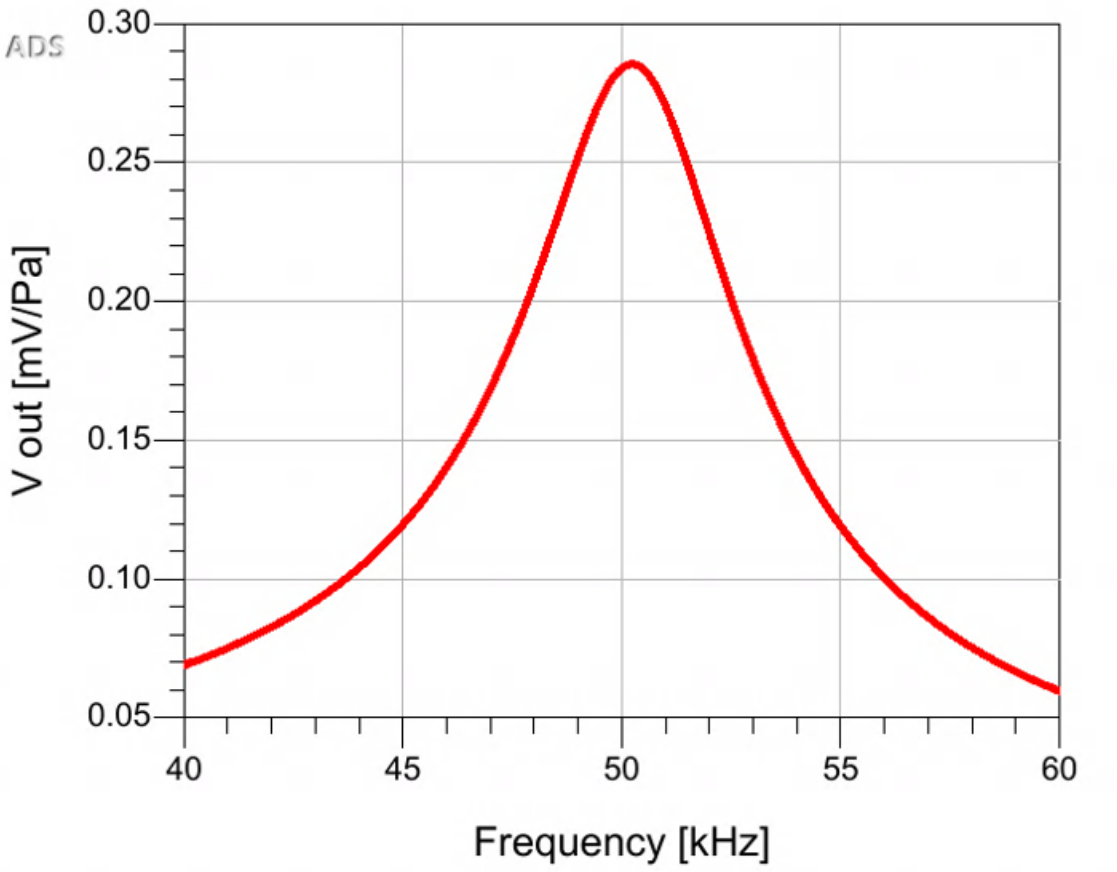


**Figure 4.3** Open circuit frequency response of the single pNUT equivalent circuit used as building block to construct the arrays model.

### 4.1.1 Full Parallel Connection

In the fabricated devices, to connect them in a parallel topology we would run a metal trace to connect all the top electrodes to one pad, and a separate trace to connect all the bottom electrodes to the other pad. In the ADS model this is represented by grounding all

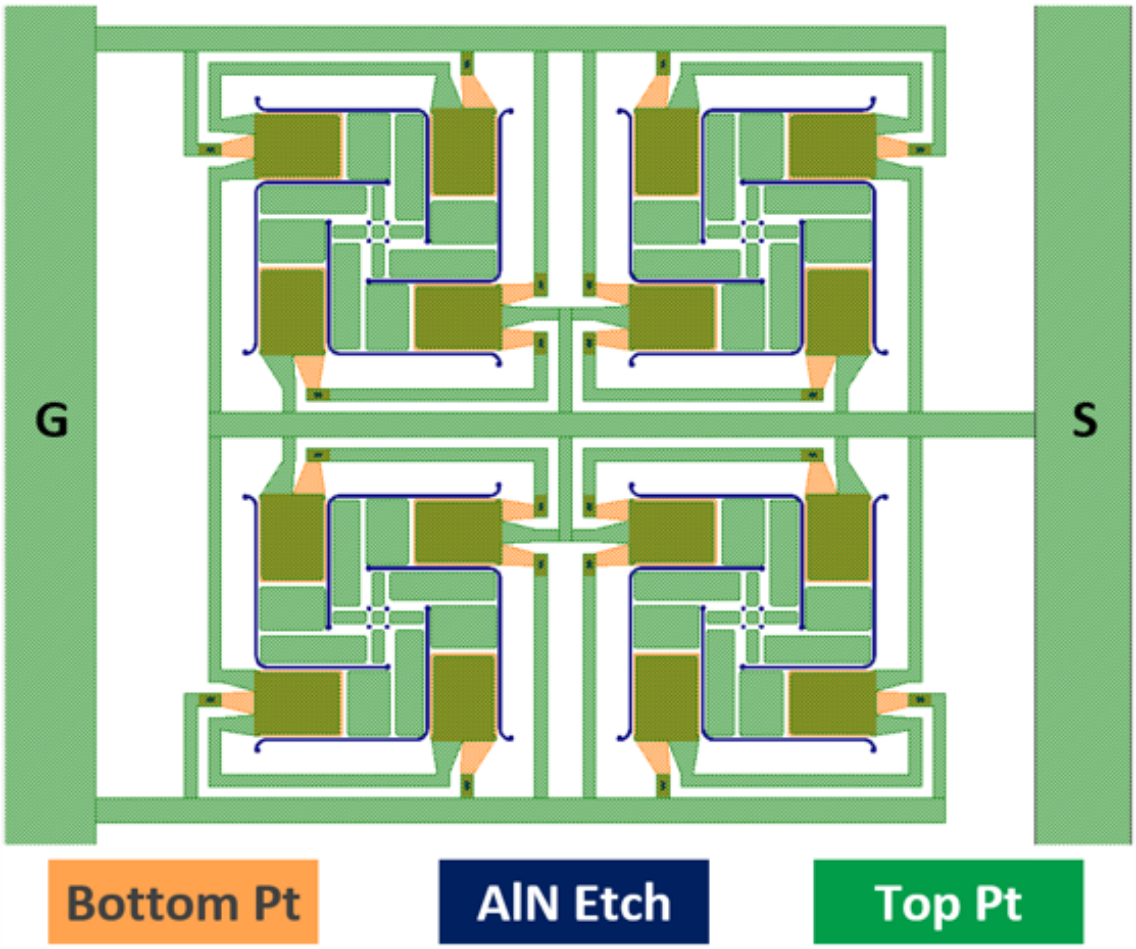


**Figure 4.4** Layout of a 2x2 parallel pNUTs array.

the bottom terminals of the electrical port and wiring all the top terminals together. As an example of how a parallel array is implemented, the layout of a 2x2 array connected in parallel configuration is shown in Fig. 4.4. To study how the response scales with size, we build a 2x2 and a 3x3 parallel array, characterized by 4 and 9 individual cells respectively. Then, we run an AC simulation the same way as the individual pNUT cell example shown above. When probing the open-circuit voltage, the response is identical as the one shown in Fig. 4.3 since all the cells terminal are connected together. When probing the short-circuit current, we observe the response shown in Fig. 4.5.

From the device response, it follows that a parallel connection topology is more suitable for a receiver based on a current sensing amplifier, as the sensitivity (measured in current

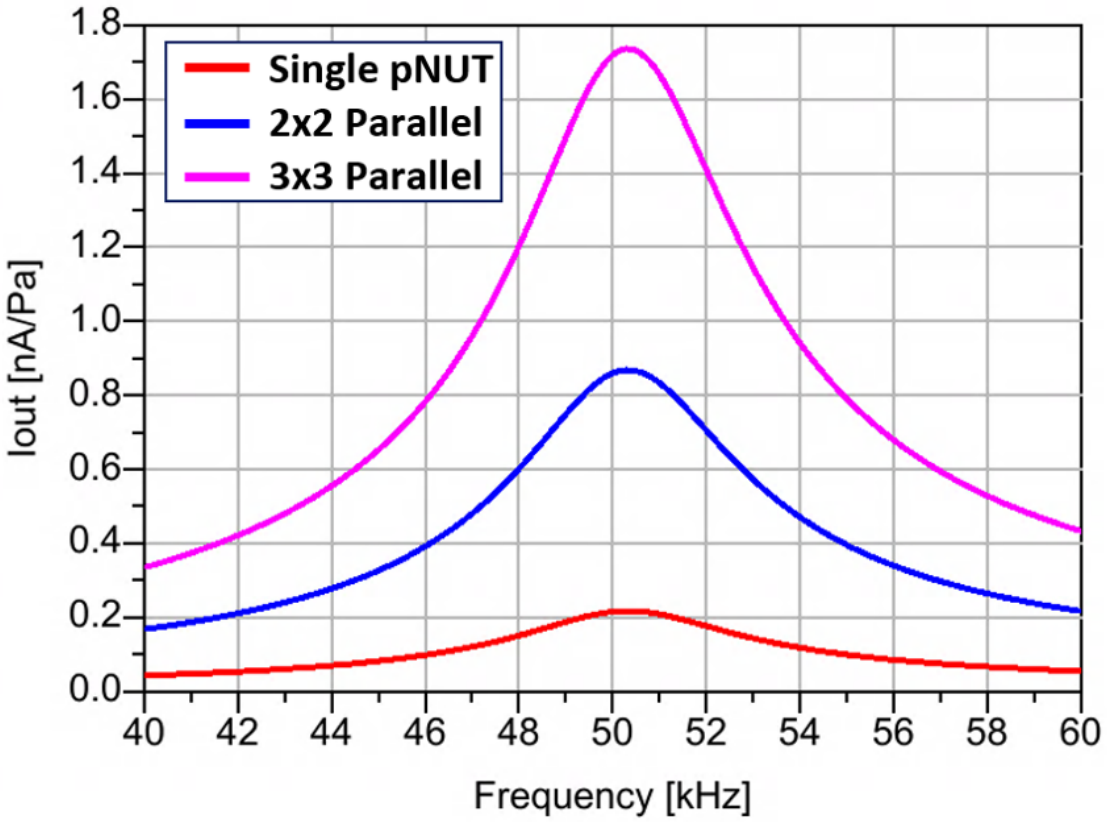


**Figure 4.5** Short-circuit current response of parallel-connected pNUTs arrays.

per unit of pressure in this case) increases linearly with the number of devices. In other words, the sensitivity has a linear dependence to the total transducer area. In case a voltage amplifier is used to recover the response, the parallel array does not offer a boost in sensitivity. However, connecting the devices electrodes together changes the output impedance of the array by increasing the total capacitance, making the parasitic capacitance through the substrate and at the amplifier input less relevant (Fig. 4.6). It is worth noting that when a current sensing circuit is used, like a trans-impedance amplifier (TIA), the increase in capacitance must be taken into account when analyzing the total system performance, as it can introduce instabilities or reduce the bandwidth of the circuit [37]. Additionally, a current sensing approach makes sense as long as the input impedance of the current amplifier remains lower than the array output impedance. If we take an operational amplifier-based TIA as an example, the input impedance of the circuit is set by the gain of the system. In turn, the

system gain is set by the operational amplifier gain-bandwidth product, which is typically correlated with the circuit power consumption. Therefore, the number of devices we can add in parallel to increase the system performance is set by the available power budget.

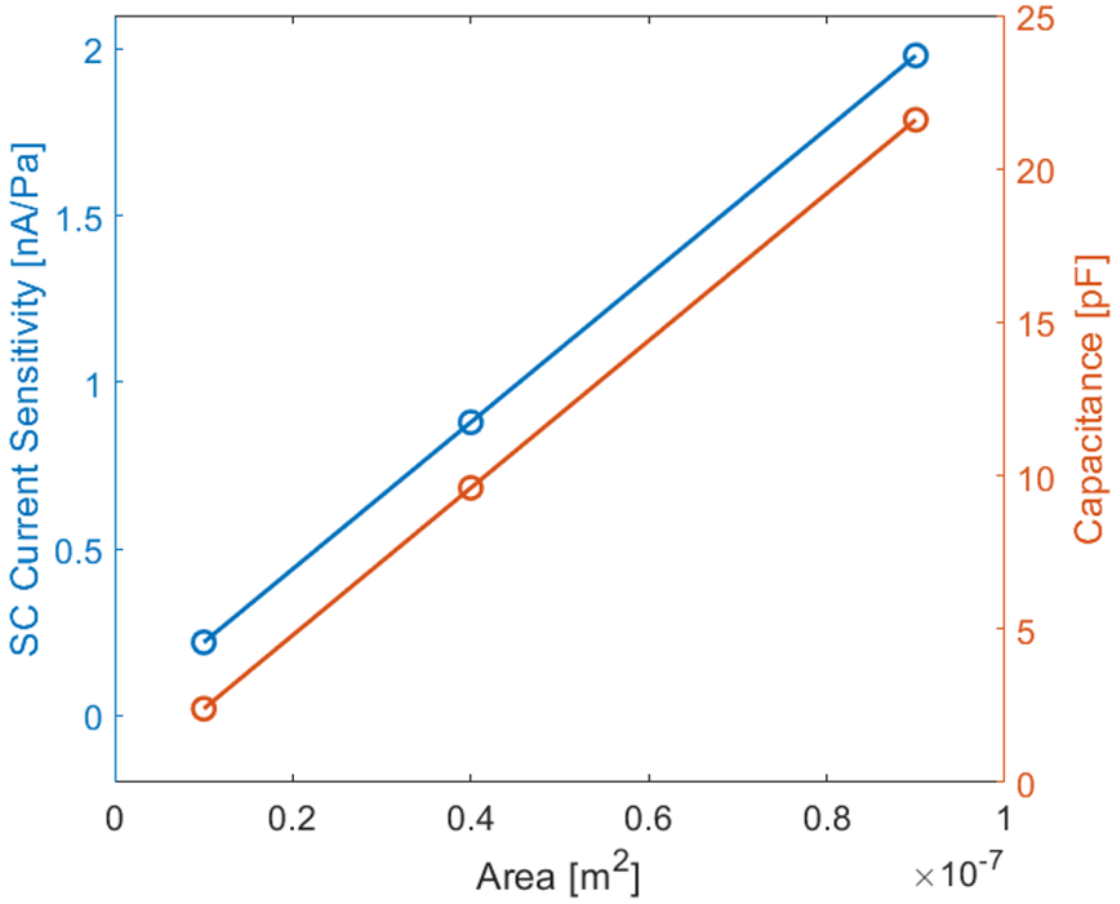


**Figure 4.6** Parallel arrays Sensitivity at resonance (50 kHz) and capacitance vs. total area.

For example, if we build a TIA with the operational amplifier used to build the circuit in Chapter 6 (MIC861 by Microchip), we have a power consumption of about 7 µW for a gain-BW product ($GBW$) of 400 kHz. The formula for the $-3dB$ bandwidth of the TIA is given by:

$$f_{-3dB} = \sqrt{\frac{GBW}{2\pi R_f C_{el}}} \tag{4.1}$$

where $C_{el}$ is the array capacitance and $R_f$ is the feedback resistor that sets the transimpedance gain. For our implementation, the capacitance of a 2x2 parallel array is 10 pF and we can set the minimum value of $R_f$ to $1M\Omega$. We also need to add a capacitor $C_f$ in the feedback loop in parallel to $R_f$ in order to compensate for the instability introduced by $C_{el}$:

$$C_f = \sqrt{\frac{C_{el}}{2\pi GBW R_f}} \tag{4.2}$$

At 50 kHz these numbers deliver a bandwidth of 80 kHz and a transimpedance gain of $600k\Omega$. A 2x2 array should generate about 1.8 nA/Pa, which means approximately 1 mV/Pa at the TIA output. Obviously, for larger parallel arrays the system gain needs to be further reduced to meet the bandwidth and stability requirements. Even accounting for the parasitic capacitance at the VA input shown in Chapter 6, we have a sensitivity close to 1 mV/Pa at the output of the first amplification stage for just a single device. Therefore, we decided to select a voltage sensing approach for our full system demo.

### 4.1.2 Full Series Connection

To connect the devices in a series configuration, we need to link the bottom electrode of the first device to the array terminal, and the top electrode to the bottom electrode of the next device. We repeat this connection for the subsequent devices. The last pNUT top electrode will be connected to the other terminal. An example of the implementation of this configuration in ADS for two pNUTs in series is shown in Fig. 4.7a, while the corresponding layout is shown in Fig. 4.7b.

The way the sensitivity scales in a series configuration occurs in an inverse way compared to the parallel configuration. We have that the total current of the array remains identical to the one of the single pNUT cell, represented by the red curve in Fig.4.5. The open-circuit

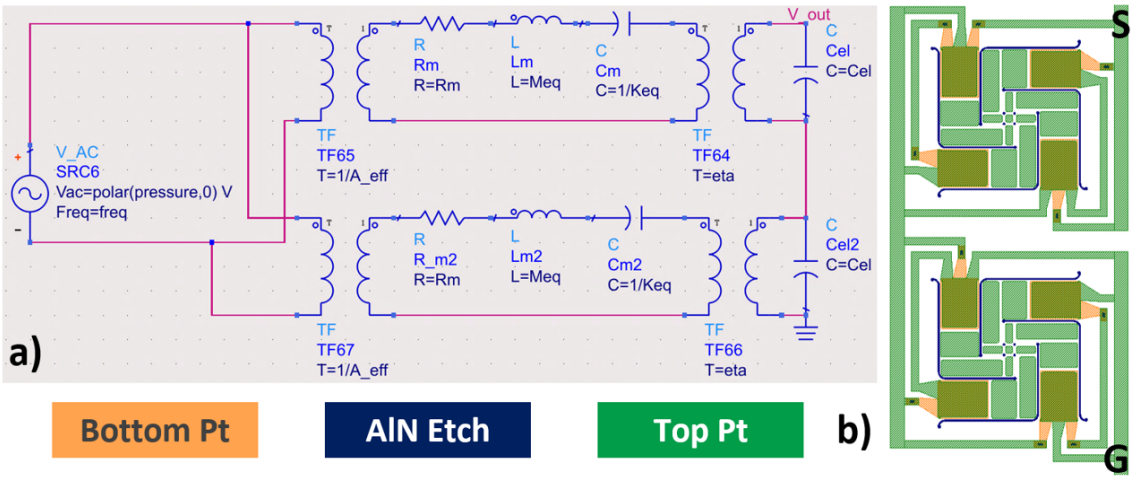


**Figure 4.7** Series connection of two pNUTs. a) Implementation of the series connection in ADS. b) layout of two devices connected in series.

voltage sensitivity on the other hand, scales linearly with the number of devices connected in series. Therefore, the output voltage per unit of pressure grows proportionally with the total array area (Fig. 4.8).

Since we are connecting the parallel plate capacitor across the pNUTs the electrodes in series, the total output impedance of the array is increased proportionally by dividing the single device electrical capacitance by the number of devices we place in series in the array. Since the current remains unchanged, it is more convenient to recover the array output electrical signal with a voltage sensing circuit. Just as the parallel array, we will incur in diminishing return in the total system sensitivity once we start taking into account the amplifier input impedance. If we do voltage sensing, ideally we would want a circuit input impedance as close to an open circuit as possible. However, realistically there will always be some parasitic capacitance between the amplifier input terminal and ground. Using an operational amplifier-based voltage amplifier or buffer, a typical value of capacitance between the positive and negative terminal stands at a few pF, which can be brought down to a few hundreds fF with an IC. Considering that the single pNUT electrical capacitance is also at a few pF (2.4 pF in our example), we will already observe a saturation of the system sensitivity even for small sizes of the array. This effect is shown in Fig. 4.8, where by adding a load

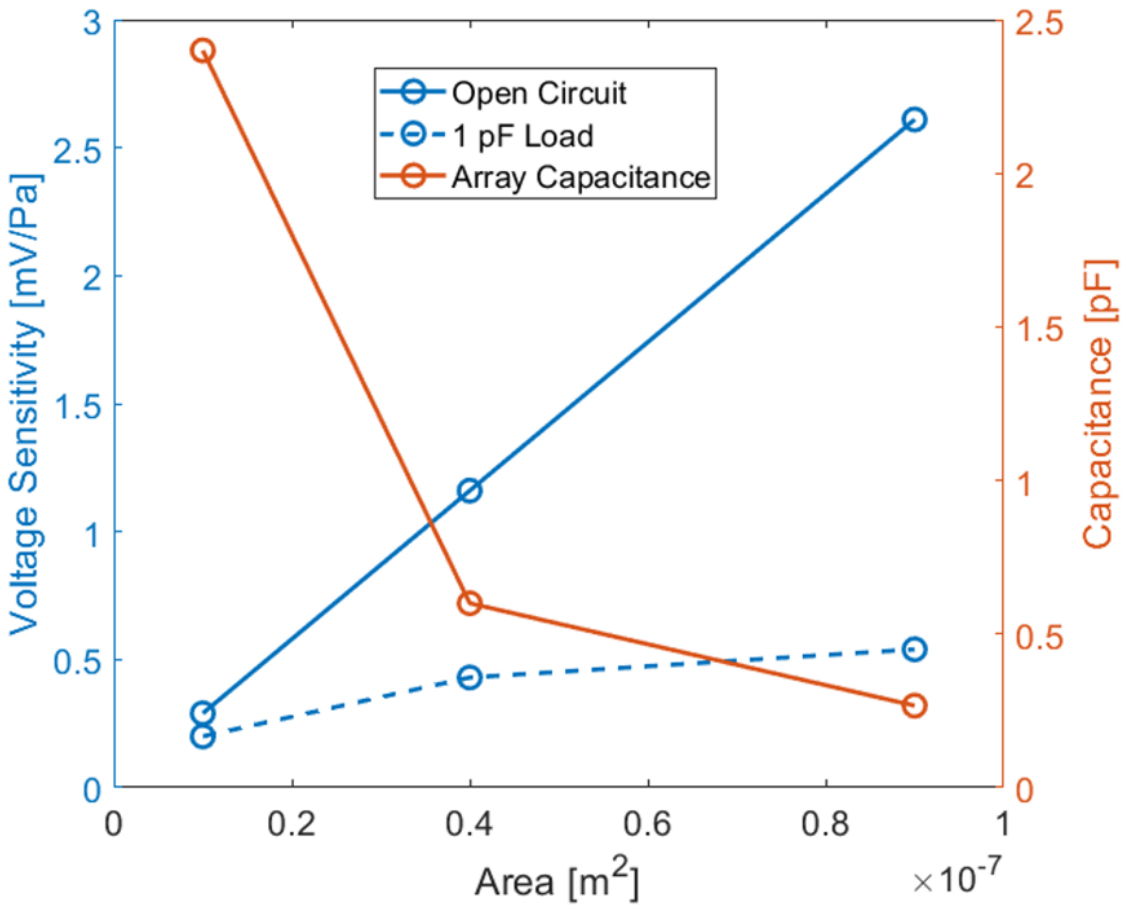


**Figure 4.8** Series arrays Sensitivity at resonance (50 kHz) and capacitance vs. total area.

of 1 pF to the array terminals we can already observe diminishing returns in the system sensitivity as we add more devices connected in series. In the voltage amplifier used in the WuRx demo (Chapter 6) the VA is built with off-the-shelf components soldered on a printed circuit board. The measured input capacitance for this VA was 6.7 pF, clearly making a series array implementation impractical. However, in a scenario in which the pNUT and an IC are monolithically integrated, the expected value of parasitic capacitance can be as low as 100 fF. At this capacitance values, the array can be formed by 20 devices connected in series before matching the parasitic capacitance and observing significant diminishing returns in the Rx Sensitivity. Such system would be characterized by approximately a 20x increase in Rx sensitivity compared to an individual device.

### 4.1.3 Series-Parallel (SP) Connection

The final connection topology we take into consideration is the SP. To implement this topology we build a linear series array as described in the previous section with the desired number of pNUTs. We then connect the same number of series array in parallel with each other as we did for the single devices in a parallel array. The layout implementation of a 2x2 SP array is presented in Fig. 4.9.

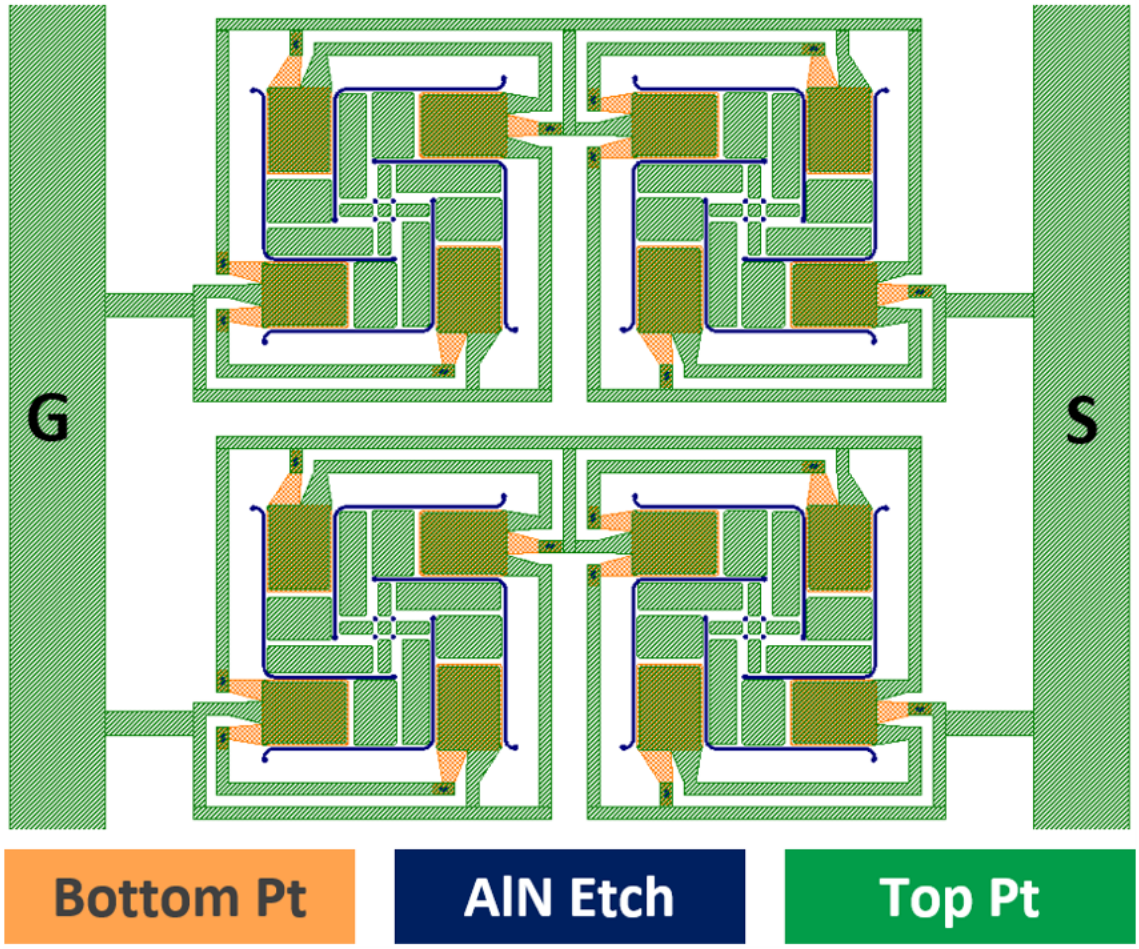


**Figure 4.9** Layout of a 2X2 SP array.

Being a balanced compromise between the series and parallel array connection approaches, the SP configuration can be used both in current sensing and in voltage sensing mode. The array open-circuit voltage sensitivity scales linearly with the number of devices in series. Each row has the same current contribution of a single pNUT. Since in a SP configura-

tion the number of parallel rows is the same as the number of devices in each row, the total short-circuit current sensitivity scales by the same amount as the voltage sensitivity. Finally, the total array electrical capacitance remains identical to the one of the individual pNUT cell. The voltage sensitivity and the array capacitance of SP arrays are shown in Fig. 4.10. We can see that in this case the array sensitivity grows with the square root of the total array area. In fact, in the SP configuration, we are trading off sensitivity for maintaining a constant output impedance. As outlined above, the series and parallel connection topologies are ultimately limited in scaling by the input impedance of the interfacing electronics. This is not the case for the SP array. While, for a given size, the theoretical sensitivity is lower than the other two configurations, once we interface it with a sensing circuit the array size can be increased arbitrarily to increase the total system sensitivity.

It is interesting to notice that, for a given array area, and in absence of a load impedance on the arrays, the total output power for a given input pressure is constant across all connection schemes. This is consistent with the conservation of energy since the same amount of acoustic power is provided to the arrays regardless of their configuration. While this is not the focus of this work, in case we are interested in recovering and converting the acoustic power from the ultrasound, the pNUTs offer the flexibility to vary the connection topology to better match the impedance of the interfacing circuit, and optimize the power transfer efficiency.

## 4.2 Noise in pNUTs Arrays

In an ultrasound receiver system, the most useful metric to quantify the minimum detectable pressure is the signal-to-noise ratio (SNR). Therefore, it is interesting to get an idea of the noise contribution of the pNUTs and how that noise scales once we form an array with different connection methods. The main noise source expected from the devices comes from the thermal dissipation caused by the friction between the device surface and the air molecules

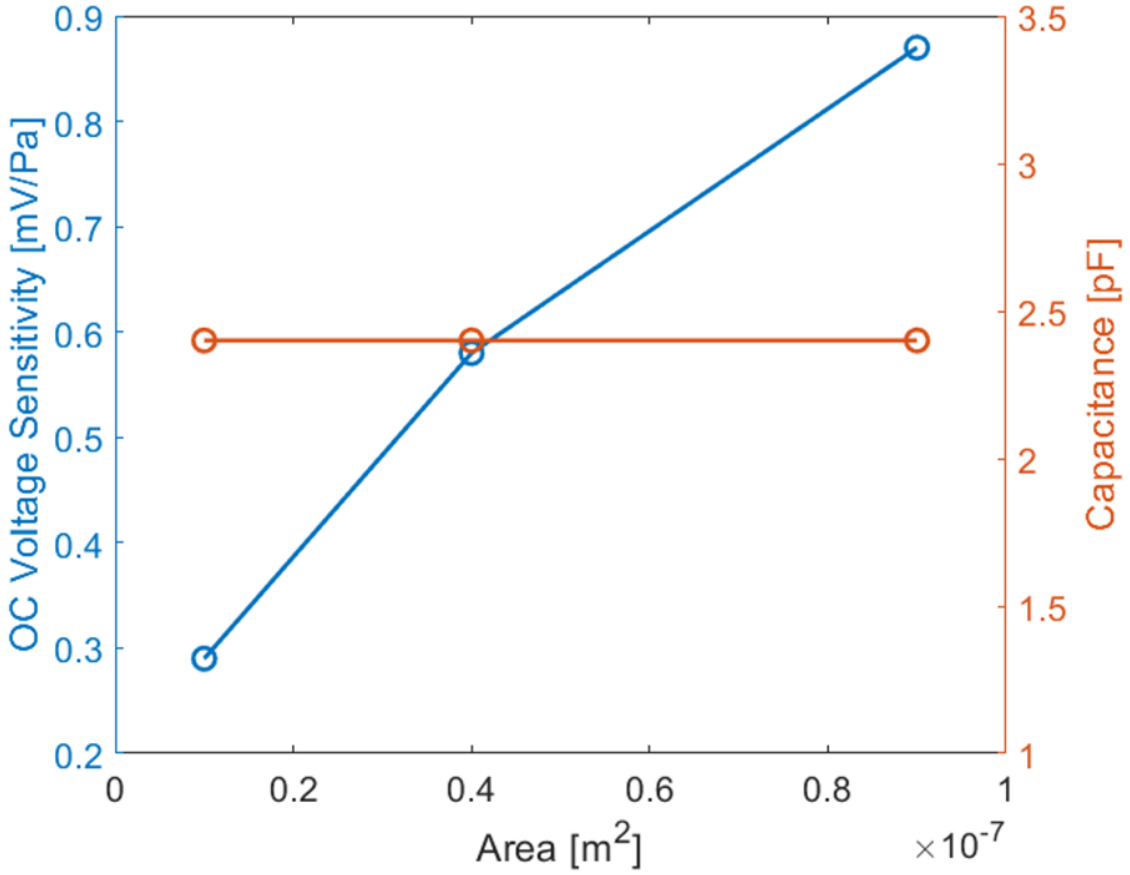


**Figure 4.10** SP arrays Sensitivity at resonance (50 kHz) and capacitance vs. total area.

surrounding it. In the purely electrical equivalent circuit (2.7), we represent this phenomenon through the equivalent resistor $R_m$. The noise spectral density source associated with this resistive element, also called Johnson noise, is given by Eq. 4.3 [38].

$$v_n = \sqrt{4k_bTR_m} \tag{4.3}$$

where $k_b$ is the Boltzmann constant. The noise at the device terminals is shaped by $C_m$, $L_m$, and the electrodes capacitance $C_{el}$. We can obtain the RMS amplitude of the noise by integrating the spectral density over the device resonance peak frequency range (i.e. the device spot noise [39])

$$V_n = \sqrt{4k_bT \int_{BW} Z_{out}(f)df} \tag{4.4}$$

where $Z_{out}$ is the impedance of the pNUT as seen from the electrical port. We obtain the device noise spectral density from the AC simulation in ADS. As an example, we can see the spectral density for a SP and Series arrays in Fig. 4.11 compared to that of a single device. We see that the spectral density of the SP array remains identical to the one of the individual pNUT cell. This is expected since the overall impedance of a SP array stays constant regardless of the size of the array. By integrating over a 20 kHz bandwidth around the resonance frequency, for the SP arrays the total RMS noise $V_n$ stands at around 1 µV. In a similar way, in the series array the total impedance increases linearly, while the equivalent noise source between the array terminals increases sub-linearly (follows square root law). The equivalent noise source at the terminals is obtained by taking the square root of the squared sum of the noise sources. The corresponding increase in noise is shown in Fig. 4.11 on the right.

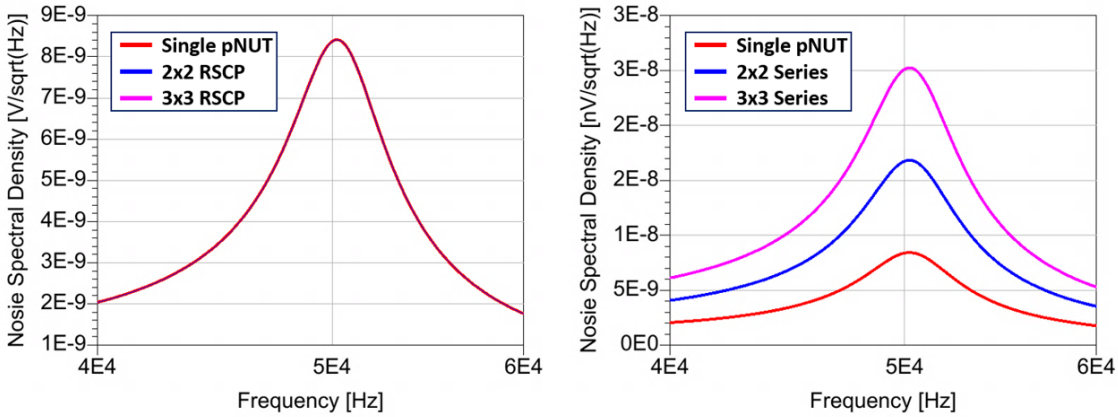


**Figure 4.11** Spectral density of a single pNUT, SP, and Series arrays.

As shown in Chapter 5 in the WuRx system demonstration, the noise from the pNUTs is not the limiting factor for the system sensitivity, and we will see that these noise levels are negligible compared to the ones measured from the electronics. These findings are critical

in pointing out that arrays of pNUTs can be used to effectively enhance the overall system sensitivity.

# Chapter 5

# Devices Characterization

In this chapter we describe the methodologies and experimental setups used to characterize the fabricated pNUTs. The devices discussed here and in chapter 6 are part of the last batch of fabricated devices. As described in chapter 3, these devices were released directly during the DRIE step. Because of this, the devices yield was much lower than it would normally be. However, from the few devices that survived the release process, we are able to obtain enough information to validate the models presented in the previous chapters and show a demonstration of a long-range miniaturized ultrasound WuRx. We consider 4 classes of devices:

- Individual pNUT with floating metal
- Individual pNUT without floating metal
- 2x2 SP array without floating metal
- 3x3 SP array without floating metal

These devices were obtained from two chips that were released separately. The individual pNUTs were obtained from the first chip, while the arrays were obtained from the second chip. As discussed in the following sections, this will lead to slight differences in the frequency of

operation between the single device and the two arrays despite having identical geometries and having the same equivalent mass. The laminate layers thicknesses measured in this fabrication were 30 nm, 130 nm, and 230 nm for the bottom Pt, AlN, and top Pt respectively.

SEM pictures of the devices are presented in Fig. 5.1.

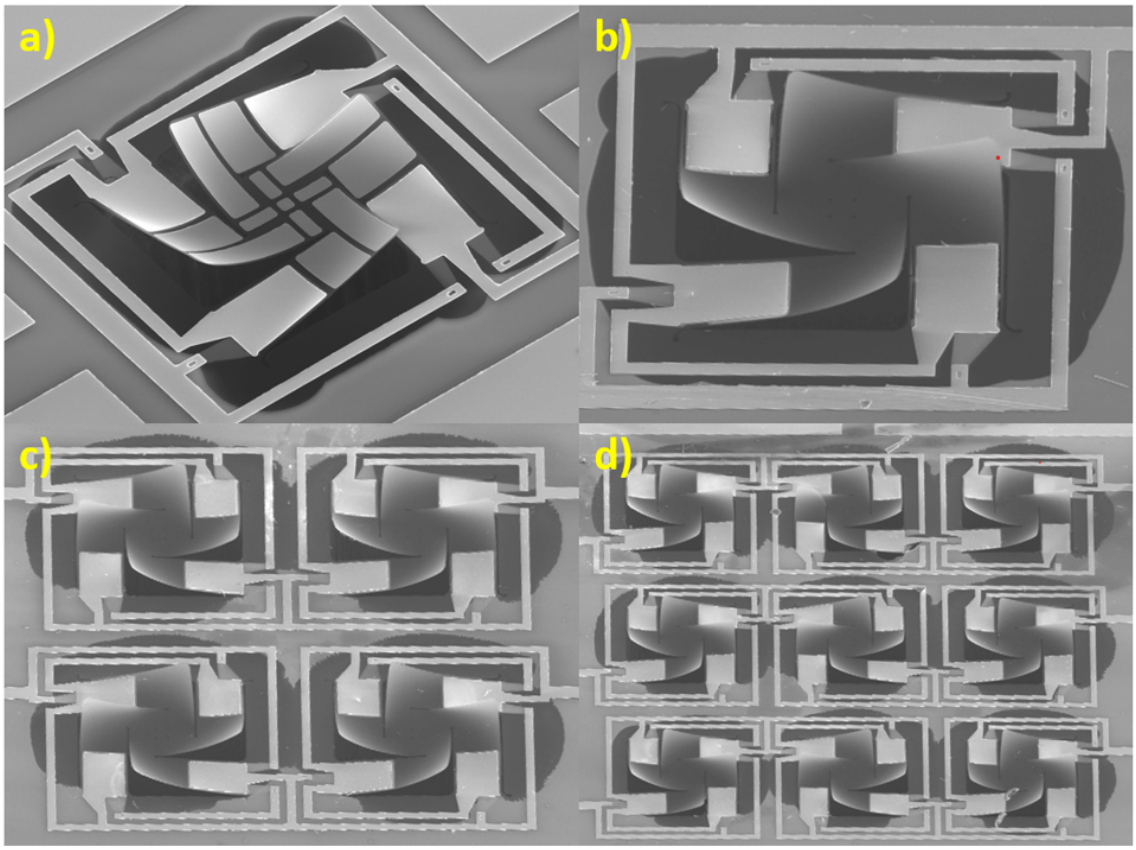


**Figure 5.1** SEM images of the four measured devices. a) Individual device with floating metal. b) Individual device without floating metal. c) 2x2 SP array without floating metal. d) 3x3 SP array without floating metal.

## 5.1 Tx Sensitivity Measurements

The first step to characterize the devices is to measure their Tx sensitivity. The Tx sensitivity is measured by applying an external voltage between the pNUTs electrodes and recording the resulting out-of-plane displacement. We measure the Tx sensitivity in nm per unit voltage (nm/V). The Tx sensitivity is obtained through digital holographic microscopy (DHM). We

use the R-2100 Series microscope by Lyncèe Tec [40]. DHM reconstructs a 3-dimensional representation of the observed sample by measuring both the intensity of a laser reflected by the sample surface - called object beam - and the interference pattern between the object beam and an internal reference. When generated, the reference beam is coherent with the object beam. By adjusting the optical length of the reference beam to be identical to the path of the object beam, we can obtain an interference pattern resulting from the phase differences between the two lasers. The phase differences are related to height variations on the sample surface. The interference pattern effectively converts the information carried by the phase of the object beam into an intensity pattern that can be measured with a camera. An example of a pNUT observed in phase mode is shown in Fig. 5.2.

**Figure 5.2** Example on a pNUT imaged under phase view.

In the figure, gradients in height manifest as fringe patterns like the ones present along the beams length. We can also see that we observe the fringe pattern only in some locations over the device surface. This is due to the thickness of the layers that make up the pNUT plate. Since the layers are extremely thin, depending on the angle of incidence of the object laser with the pNUT surface, different portions of light go through the plate instead of being reflected back into the microscope. Those regions manifest as noise in the phase image and

we cannot get height information from them, like the tip of the beams. For this reason, we recommend that the thickness of the layers should be at least 130 nm for for AlN and 200 nm for the top Pt in order to have a strong enough signal on the central plate. This recommendation is based on what has worked in this implementation, but other combinations of layer thicknesses might also work. To take the measurement, we take advantage of the stroboscopic unit that comes with the DHM. In stroboscopic mode, we can generate a voltage at a given frequency and synchronize it with the DHM image sampling. While taking and processing a single frame can take several periods, thanks to the stroboscopic module we can reconstruct the pNUT displacement over a single period by sampling the holograms at precise phases within different periods. This process is repeated for several excitation frequencies. Finally, we take a discrete Fourier transform (DFT) of the samples from each excitation frequency to generate the pNUTs Tx sensitivity in the frequency domain.

### 5.1.1 Equivalent Parameters Extraction

From the Tx sensitivity measurement it is possible to extract the equivalent parameters of the devices. Since we modeled the resonator as an RLC circuit, we extract the parameters by fitting a second order response to the measured curve. To perform the fitting we use a least-mean-squares approach. We present the fitted function both in terms of the variables $(\eta, K_{eq}, \omega_0, Q)$ and in terms of $(\eta, K_{eq}, M_{eq}, Q)$:

$$d = \frac{\eta/K_{eq}}{\sqrt{(\frac{\omega^2}{\omega_0^2} - 1)^2 + \frac{1}{Q}\frac{\omega^2}{\omega_0^2}}} = \frac{\eta}{\sqrt{(M_{eq}\omega^2 - K_{eq})^2 + M_{eq}K_{eq}(\frac{\omega}{Q})^2}} \tag{5.1}$$

In the first form, it is evident that we have 4 variables but only 3 are independent. For example, if we fix $\omega_0$ and $Q$, we can produce infinite valid values of $\eta$ and $K_{eq}$ as long as their ratio remains constant. To solve this problem we can take an educated guess on the value of one of the variables and select the others by fitting the measured displacement curves.

We will see that this approach is reasonably validated by the Rx sensitivity measurements, presented in Section 5.2.2. The variable that makes the most sense to select is $M_{eq}$. We know from Section 2.2 that $K_{eq}$ is subject to significant uncertainty from the undercut and residual stress, whereas a quick COMSOL simulation confirms that $M_{eq}$ is not affected significantly by these two phenomena. Similarly it is difficult to accurately predict the losses due to air damping. The value of $\eta$ is affected both by the non-ideally-clamped boundary condition at the beam anchors and the quality of piezoelectric layer. As verified through FEA simulations, $M_{eq}$ has little dependence on the exact beams mode shape as its value is largely determined by the mass of the central plate. Therefore, we use the value of $M_{eq}$ predicted by the analytical model and we obtain the rest of the parameters through least-mean-square fitting. The Tx sensitivity of the individual pNUTs is shown in Fig.5.3 and the equivalent parameters obtained from fitting equation 5.1 are shown in Table 5.1 along with the theoretical values from the analytical model.

**Table 5.1** Parameters extracted by fitting the individual devices Tx sensitivities. F and NF refer to the devices with and without the floating metal respectively. The value of $C_{el}$ has been measured separately with precision impedance analyzer.

| | $K_{eq}[\frac{N}{m}]$ | $M_{eq}[kg]$ | $Q[.]$ | $\eta[\frac{N}{V}]$ | $\zeta[\frac{Ns}{m}]$ | $R_m[M\Omega]$ | $C_m[fF]$ | $L_m[H]$ | $C_{el}[pF]$ |
|---|---|---|---|---|---|---|---|---|---|
| F | 2.6 | $2e-11$ | 8.9 | $3.4e-8$ | $0.8e-6$ | 708 | 0.5 | $17e3$ | 2.5 |
| NF | 2.7 | $1.3e-11$ | 5.7 | $4.3e-8$ | $1.15e-6$ | 602 | 0.7 | $6.8e3$ | 2.5 |
| *F | 2.1 | $2e-11$ | – | $1.2e-7$ | – | – | 6.9 | $1.4e3$ | 2.3 |
| *NF | 2.1 | $1.3e-11$ | – | $1.2e-7$ | – | – | 6.9 | $0.9e3$ | 2.3 |

*Analytical model, not accounting for undercut and residual stress (see Section 2.2)

Looking at the extracted parameters, we can see that the devices have similar values of $K_{eq}$. This does not follow automatically by the imposed values of $M_{eq}$, since the corresponding values of $K_{eq}$ are determined by the measured positions of the resonant frequencies. The fact that the values of $K_{eq}$ in the two devices are almost identical confirms the intuitive

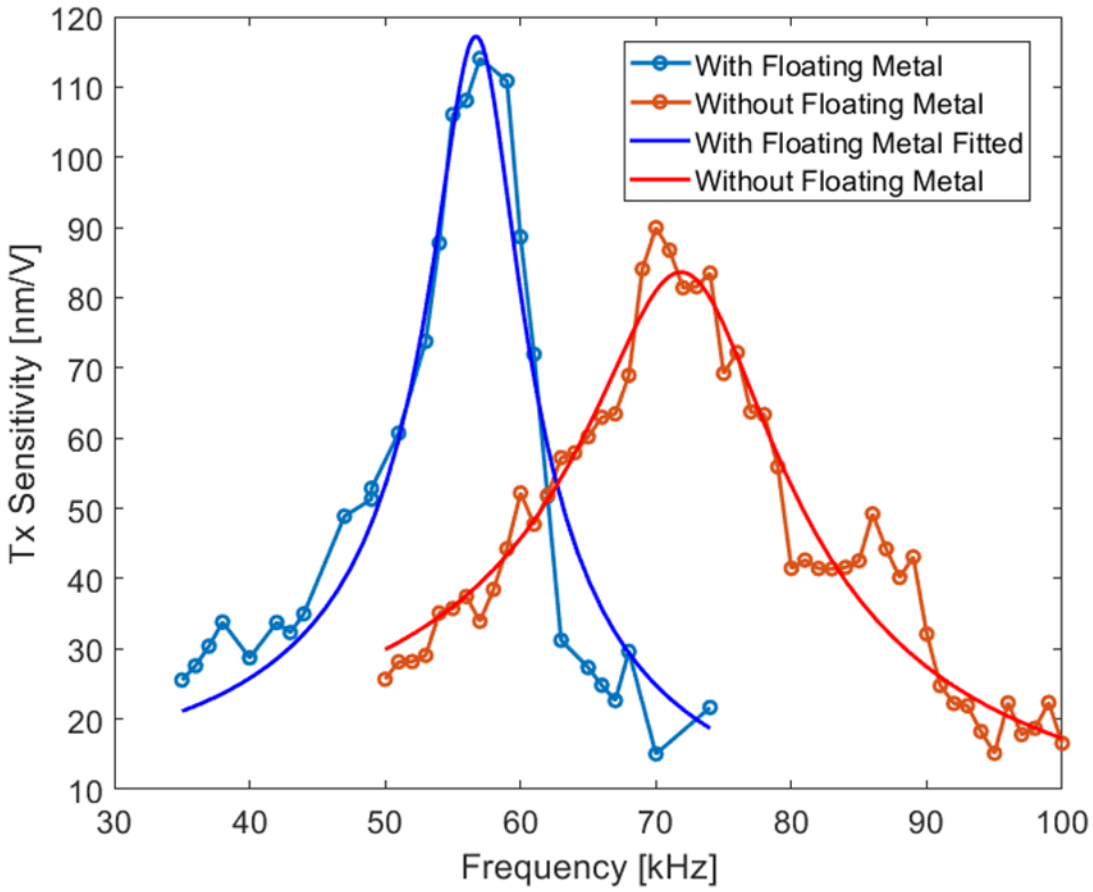


**Figure 5.3** Measured individual pNUTs Tx sensitivity along with the fitted curves.

observation (verified in COMSOL) that most of the stiffness is defined by the mode shape in the clamped region of the beams where the electrodes are located, which is identical for the two measured pNUTs designs. Additionally, we expect the two devices to have very similar levels of stress in their layers as they were positioned very close to each other, and consequently have similar levels of stress-induced stiffening. Therefore, whether the floating metal is present or not is the main reason the two devices have different center frequencies. It is interesting to see that the extracted values of $K_{eq}$ are not too far off from the ones predicted by the purely analytical model. This effect was shown in Sections 2.2.1 and 2.2.2, where we see that the undercut softens the transducer considered in the purely analytical model, while adding positive residual stress in the Pt layer has the opposite effect, bringing the resonance frequency back up. From the undercut study we see that for levels of undercut

of 15 µm or larger - as is the case for the fabricated devices - there is not significant additional softening. We also see that the softening lowers the devices resonance frequency by the same factor for both the presented layer thickness cases. This observation allows us to estimate the drop in stiffness caused by the undercut in the fabricated devices, which changes from 2.1 N/m down to 0.85 N/m. Then, we can estimate the value of the residual stress that causes the stiffness to increase to 2.6-2.7 N/m. The stress level in the AlN layer is both more controllable and repeatable than the stress measured in the Pt during the deposition recipe characterization, and was estimated to be between 20 and 50 MPa. Therefore we can expect the majority of the stress-induced stiffening to be caused by the top Pt layer. During the Pt sputtering characterization, for the same deposition parameters, we measured stress levels ranging around ±100 MPa the expected value. In the Pt deposition run during the devices fabrication we tuned the argon pressure to make sure we would get a positive residual stress in the 100-200 MPa range. In order to increase the devices stiffness from 2.1 N/m up to 2.7 N/m a residual stress of approximately 200 MPa is necessary, which is in agreement with the Pt recipe we characterized. Another interesting insight comes from the scaling of the quality factor between the two pNUTs design. Looking at the scaling from air damping losses reported in equation 2.22, we have that $Q_{air}$ is expected to scale as $\propto M_{eq}f$. Using the resonance frequencies of 57 kHz and 72 kHz, and the respective values of $M_{eq}$, we should obtain a theoretical value of $Q_{air}$ that is 1.54 times higher in the pNUT with the floating metal compared to the variation without it. This value is quite close to the factor of 1.74 obtained from the ratio of quality factors obtained from the curves fitting. Finally, we can compare the values of $\eta$ and $C_{el}$ with respect the one expected from theory. Using equation 2.10, we obtain a theoretical value of $1.2e-7\frac{N}{V}$. The measured $\eta$ of around $0.4e-7\frac{N}{V}$ is on the same order of magnitude but around 60% lower than the ideal value. This should be expected because of non-idealities such as the undercut from the devices release, which affects the device mode shape around the clamped region as pointed out in Section 2.2.1. According to the analysis in Section 2.2.1 the expected reduction was actually more important than 60%,

at around 95% for a 25 µm undercut. A possible explanation for the difference between the extracted experimental value and the model is that the geometry used in the FEA model does not account for the effect of the metal traces connecting to the electrode. These traces significantly stiffen the beam anchor, partially compensating for the softening caused by the release undercut. Using equation 2.11 we have a theoretical capacitance value of $2.3pF$. The experimental values of $2.5pF$ were obtained in a separate measurement with a high precision impedance analyzer. To take the measurement we use two DC probes and landed them on the device terminals to access the device electrodes. We did not have the calibration kit for the impedance analyzer at hand, therefore only the open circuit calibration was performed. The calibration was done over a frequency range between 30 kHz and 100 kHz while only one of the two probes was in contact with the pads. After the calibration was finished the other probe was landed to take the impedance measurement. We observed a value of around $2.5pF$ over the entire frequency range. The difference of a few hundreds of fF's between the theoretical and the measured values can be attributed to parasitic capacitance between the pads through the substrate.

### 5.1.2 Measurements at Low Pressure

We also performed the Tx measurements at low pressure on the pNUT with floating metal. Because of the limited availability of the vacuum chamber and the complexity of the experimental setup, the measurement was done only on one device. The first step to set up the experiment is to secure the chip on a printed circuit board (PCB) with double adhesive tape, and to connect the device pads to two signal and ground metal traces via wirebonding. Then, the PCB is itself secured to a platform with tape and two jumper wires are soldered to the traces. The vacuum chamber has an opening on the topside that can be covered by a 1 cm thick glass cover and several wires that go through a sealed passage to provide electrical access to the inside of the chamber from the outside. The platform with the PCB on top is

placed inside the vacuum chamber, and the jumper wires are secured to the chamber wires with a set of screws.

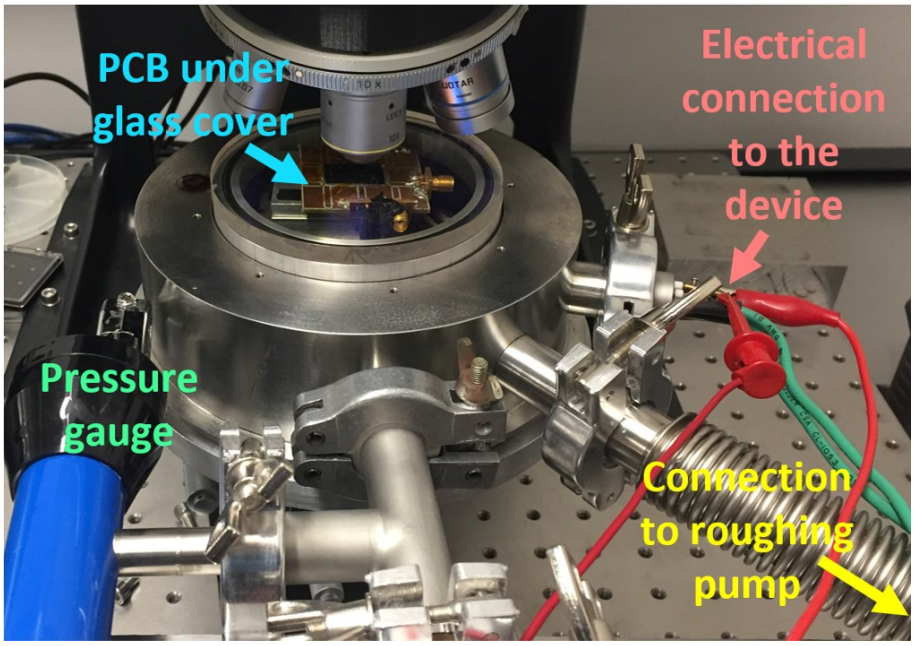


**Figure 5.4** Experimental setup used to measure the Tx sensitivity at low pressure.

It is important to adjust the height of the platform to make sure that when the glass cover is placed on the chamber opening the PCB is right below it. Having a few SMA connectors soldered around the PCB provides enough spacing from chip to make sure the devices are not damaged by being touched by the glass cover. This step is important for two reasons. 1) the pump-down process generates quite strong vibrations, and having the PCB stuck between the platform and the glass makes sure that nothing in the chamber moves. 2) We need the devices to be extremely close to the glass to be able to re-calibrate the tool to compensate for the glass diffraction and image them with the Lyncee Tec. Finally, we connect the chamber wires to the Lyncee Tec stroboscopic unit, and the chamber to a roughing pump. The complete setup is shown in Fig. 5.4.

Because of the vibration, it was not possible to image the devices while the pump was active. Therefore, the minimum stable pressure that the chamber was able to hold after turning the pump off was $0.1 Torr$. This pressure is not low enough to make the losses from

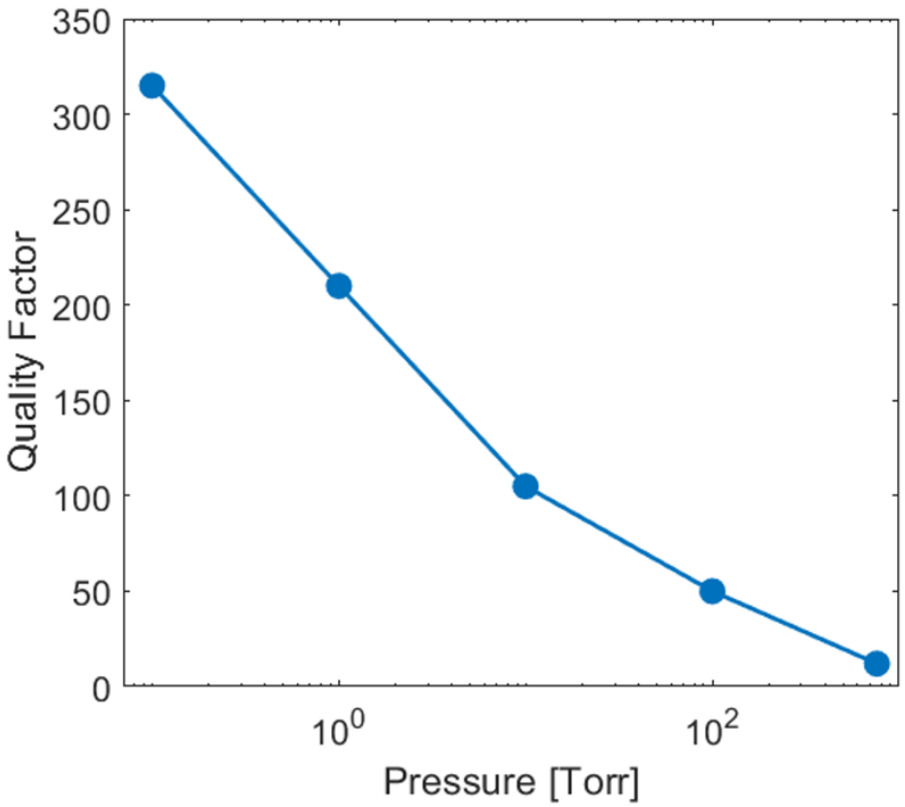


**Figure 5.5** Quality factor of the pNUT measured at different pressures.

air damping negligible compared to the anchor losses through the substrate, which should occur at around $0.1mTorr$. In this measurement, presented in Fig. 5.5, we see a discrepancy between the theoretical scaling of the quality factor with respect to the chamber pressure. From the theory, we expect the air-damping losses in flexural resonators to scale with the air pressure. From the data presented in Fig. 5.5, we see that this is the case only in going from atmospheric pressure ($760Torr$) down to $100Torr$. Below this pressure we approximately have a doubling in quality factor for every decade of pressure. To confirm whether this trend is correct or not more measurement are needed. However, this measurement serves as a confirmation that air damping is the loss mechanism that dominates in setting the device frequency response in air.

### 5.1.3 Arrays Tx Sensitivity

As mentioned at the beginning of the chapter, the measured arrays were part of a separate chip. Because of the fabrication challenges explained in Chapter 3, the release process was not readily controllable. This means that, compared to the individual devices, the devices that compose the arrays experienced slightly different undercut levels and profiles. Because of these reasons, the center frequency of the devices in the array (without the floating metal) has increased from 72 kHz to 90 kHz. The frequency response of the every device in the 2x2 SP array was measured in the Lyncee Tec and is displayed in Fig. 5.6.

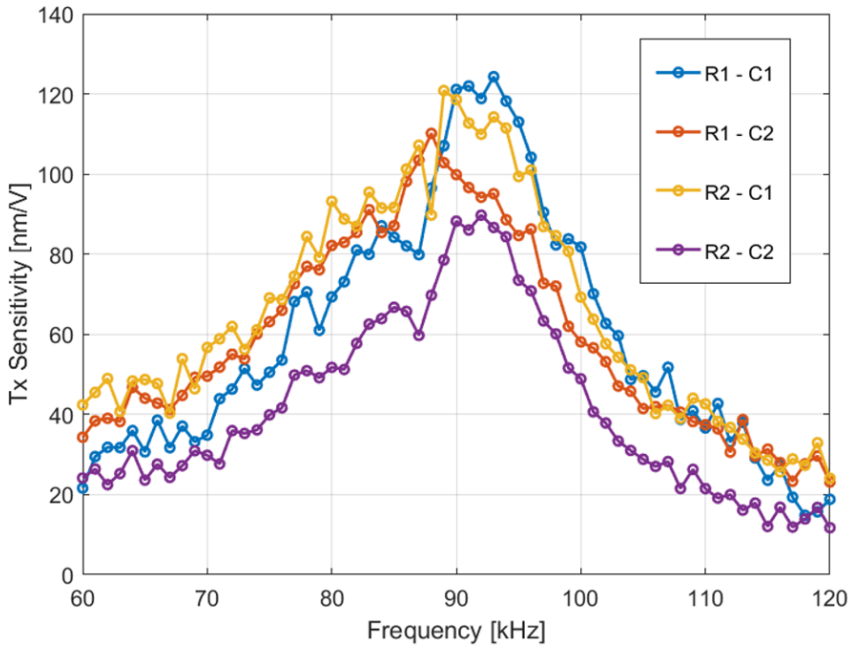


**Figure 5.6** Tx sensitivity of the 4 pNUTs in the 2X2 RSCP array.

These curves were obtained by applying a 2 V actuation at the array electrodes, with the assumption that the devices are characterized by similar electrical capacitances. With this assumption, observed displacement on every single device should equal the the displacement per unit voltage. We obtain the equivalent parameters with a similar fitting approach as in Section 5.1.1. The 4 curves fitted parameters are shown in Table 5.2.

Clearly, since we assigned a $M_{eq}$ value identical to the one of the single pNUT with a

**Table 5.2** .

| | $K_{eq}[\frac{N}{m}]$ | $M_{eq}[kg]$ | $Q[.]$ | $\eta[\frac{N}{V}]$ | $\zeta[\frac{Ns}{m}]$ | $R_m[M\Omega]$ | $C_m[fF]$ | $L_m[H]$ |
|---|---|---|---|---|---|---|---|---|
| R1C1 | 4.4 | $1.3e-11$ | 6.8 | $7.7e-8$ | $1.1e-6$ | 186 | 1.3 | $2.2e3$ |
| R1C2 | 4.1 | $1.3e-11$ | 4.9 | $8.6e-8$ | $1.5e-6$ | 202 | 1.8 | $1.8e3$ |
| R2C1 | 4.2 | $1.3e-11$ | 5 | $9.5e-8$ | $1.5e-6$ | 163 | 2.1 | $1.4e3$ |
| R2C2 | 4.3 | $1.3e-11$ | 6.9 | $5.3e-8$ | $1.1e-6$ | 382 | 0.7 | $4.6e3$ |

resonance at 72 kHz, the devices in the array presented a higher value of $K_{eq}$ to obtain a fitted curve with a 90 kHz resonance. A clue as of why the devices in the array present a higher resonance frequency can be found by inspecting the devices SEM images. We re-propose the SEM images of the individual pNUT and the 2x2 array shown in Fig. 5.1 below, in Fig. 5.7, highlighting the likely source for the discrepancy in $K_{eq}$ values.

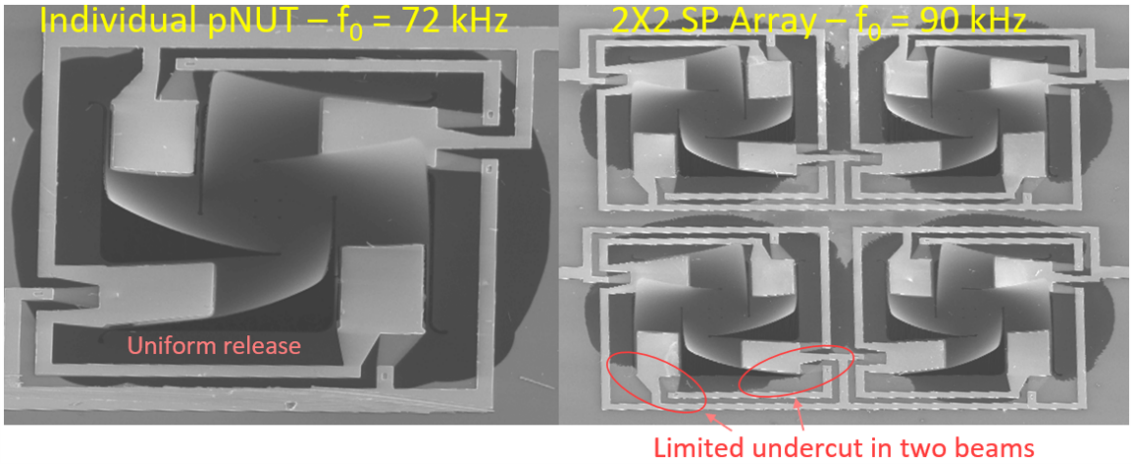


**Figure 5.7** Comparison between the undercut profiles of the individual pNUT and the 2x2 SP array.

In Fig. 5.7 it becomes evident that, unlike the individual device, the array experienced an uneven release profile. We see that all devices part of the 2x2 array present limited undercut in 2 out of 4 beams. In all devices the 2 beams are on the same side, and the same effect can be observed on the 3x3 array SEM picture in Fig.5.1. The consistency of this effect suggests that the source of the uneven undercut is a small offset in the back-side etch lithography

alignment. The reduced undercut at the base of the beams explains why we observe both an increase in $K_{eq}$ and $\eta$ when extracting the equivalent parameters of the devices in the array. As pointed out in Section 2.2.1, the presence of the undercut at the base of the beams modifies the beams mode shape by relaxing the ideal zero-angle constraint and reducing the amount of bending experienced at the beams anchors. From equations 2.9 and 2.10, we know that the value of both $K_{eq}$ and $\eta$ is set by the amount of bending experienced by the beam (i.e. the mode shape second derivative). Therefore, we can expect that variations in the undercut at the beams base will translate in corresponding variations for both $K_{eq}$ and $\eta$.

At resonance, the pNUTs in the array show quality factors and displacements similar to that of the single device. A likely source of the small difference in displacement is that, because of the uneven release, some parts of the plate experience higher displacement amplitudes than others. To a lesser extent, this effect should also be expected in an evenly released device, since the analytical model assumption that the plate is perfectly rigid is an ideality. Unfortunately, it is not easy to characterize the displacement over the pNUT surface. Because of the small thickness of the layers, when we measure the displacement the data often present artifacts. These errors in the data are easy to spot and the corresponding measurement is discarded, but they make the measurement process slow and based on trial and error when selecting different regions on the center plate. Because of this, we expect that the equivalent displacement of all devices should be in the region found in between the lowest and the highest curves.

Because of the reciprocity of the system, we can expect the resonance Rx sensitivity response to be similar for the devices in the array as the single pNUT despite having different resonance frequencies (90 kHz and 72 kHz respectively). An interesting insight from the response in Fig. 5.6 is that because of air damping, the devices have enough frequency bandwidth for their frequency response to overlap, and subsequently increase the overall array sensitivity when used in Rx mode. From Fig. 5.6 we see that the peak frequencies range between 88 kHz and 92 kHz. These frequencies cover a range of 4 kHz, while the 3

dB bandwidth of all devices is approximately 20 kHz. Although quite small, the differences in resonance frequency between devices within the same array can be easily explained by slightly different release profiles, as shown in Fig. 5.7.

## 5.2 Rx Sensitivity Measurements

The Tx sensitivity measurements presented in the previous section were necessary to determine the device equivalent parameters and to locate their frequency of operation on the 30 to 100 kHz range we are interested in. Since the devices are meant to be used as part of a WuRx, we can now proceed to characterize their electrical response when exposed to airborne ultrasound. To generate the airborne ultrasound we use commercial ultrasound sources purchased from ProWave [5]. The available sources center frequencies are at 25 kHz, 32 kHz, 40 kHz, 50 kHz, and 82 kHz, respectively corresponding to the transducer model numbers 250ST160, 328ST160, 400ST100, 500MB120, and 080SR365. Exciting the ultrasound sources off-band still generates ultrasound at lower pressures. At those frequencies, the distance between the ultrasound transmitter (Tx) and the pNUT must be reduced in order to obtain a readable electrical output. To read the pNUT output, we need to amplify the output voltage between the electrodes and detect it with an oscilloscope. The voltage amplifier (VA) we used is described in Chapter 6 as part of the complete WuRx system demo. To measure the signal amplitude, we feed the amplifier output to a UHF Lock-In amplifier by Zurich Instrument (ZI) [41]. Through the ZI software interface LabOne we can use the UHFLI as an oscilloscope and monitor the signal at the VA output in frequency domain. As the UHFLI is equipped with two channels, we can simultaneously observe the pressure amplitude that is present at the pNUTs location, and use it to quantify the Rx sensitivity in mV/Pa. To measure the pressure we use the Type 4939 calibrated microphone rated up to 100 kHz [42], along with its conditioning amplifier.

### 5.2.1 Rx Sensitivity Angular Dependency

The first step to characterize the devices in Rx mode is to verify whether their response has an angular dependence on the direction the ultrasound is coming from. To perform this measurement, we taped the VA and the devices on a metal stage. The metal stage is connected to a pole through a slider that allows for adjusting its vertical position. The pole is positioned on a table with the devices right at the edge. Next, we take the position on the table border as the angular center. On the floor under the table, we use this position to arrange tape lines in a semicircle at $15^o$ intervals. All tapes are $1m$ long. On a separate cart, we position the Tx and the arbitrary wave generator (AWG). The Tx holder is also attached to a pole and we can adjust its vertical position. The set up is shown in Fig. 5.8.

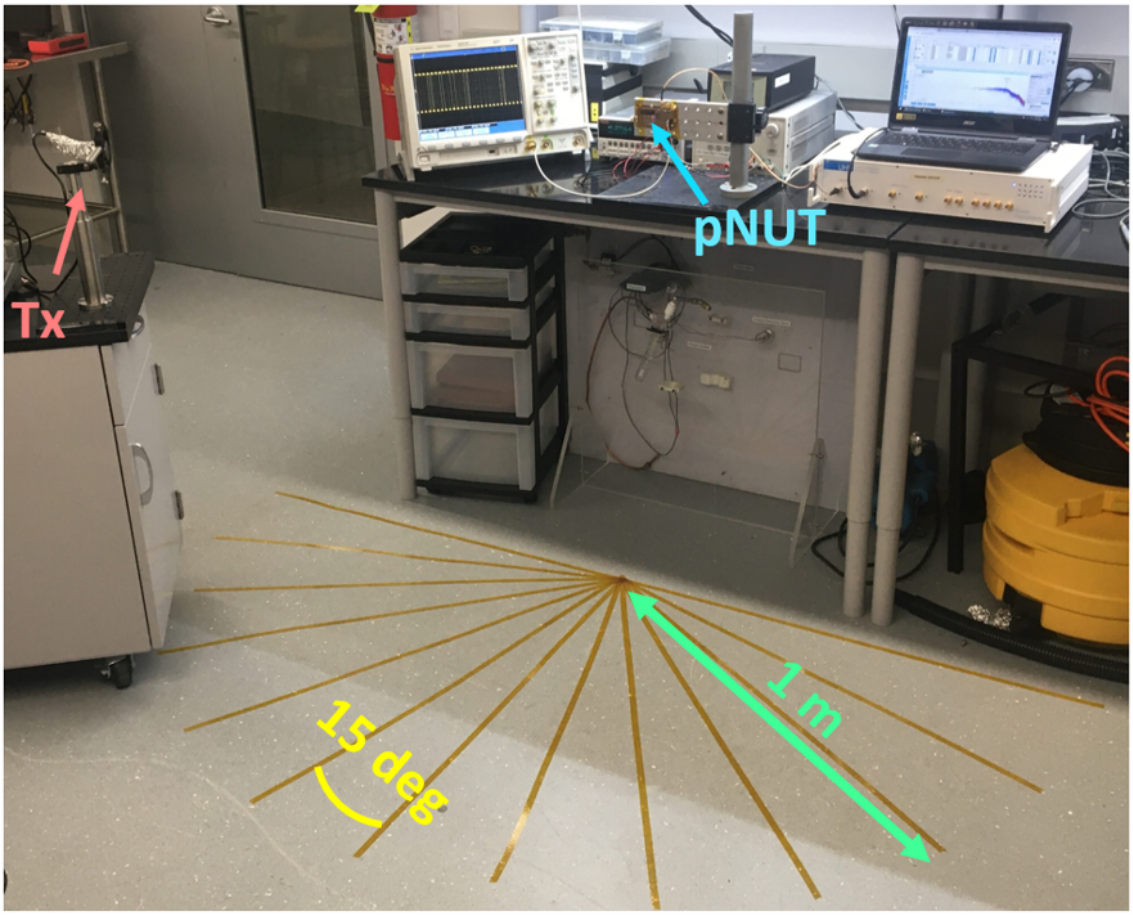


**Figure 5.8** Setup used to measure the Rx mode angular sensitivity of the pNUTs.

To perform the measurement, we make sure that the cart is aligned with the tape line. We generate the ultrasound and record the output voltage at the VA output. Additionally the pressure at the pNUTs location is monitored to make sure it is consistent across angles. This procedure is repeated for all lines in the angular range between $15^o$ and $165^o$. The normalized Rx sensitivity for this measurement is shown in Fig. 5.9. As expected, no major nodes were observed during this experiment. In the frequency range of interest, the wavelength of the ultrasound in air is several mm long, while the biggest array we are considering (the 3x3 SP) is only 400 µm in lateral dimensions, around 1 order of magnitude smaller. In a similar way as observed in antennas, small radiators tend to be isotropic. In the measurement presented in Fig. 5.9, the normalized response remains very close to 1 at all angles. It seems to be slightly lower at the limit angles of $15^o$ and $165^o$, although we think it can be attributed to the VA wires that partially covered the sides of the chip.

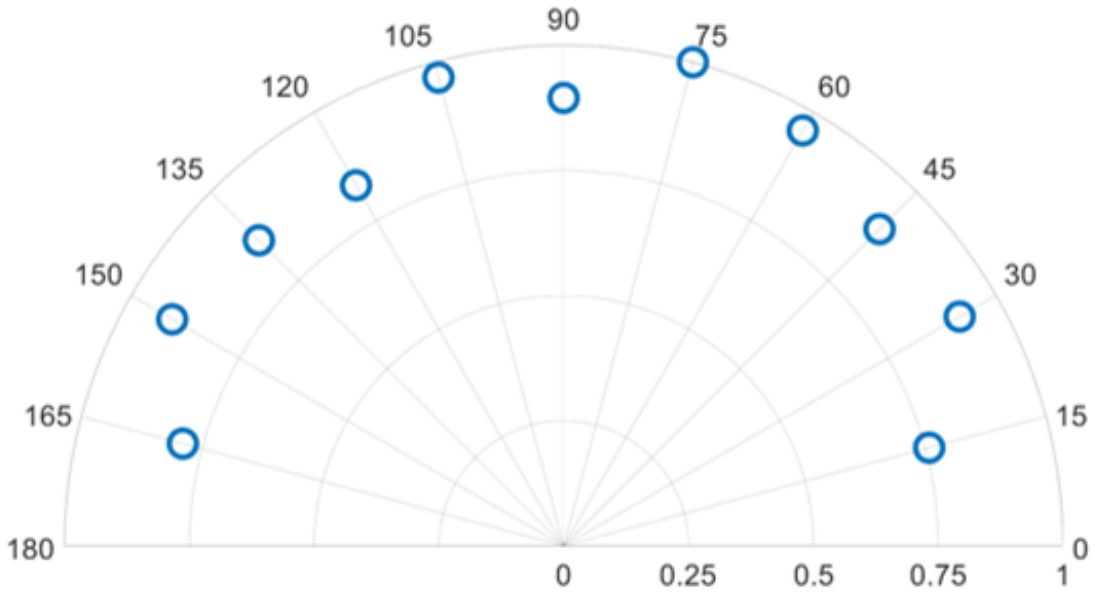


**Figure 5.9** Normalized angular Rx sensitivity of the 2X2 SP pNUT array. The slightly lower response at $15^o$ and $165^o$ angles is likely due to the VA wires on the side of the chip.

### 5.2.2 Single Devices Rx Sensitivity

Once we established that the devices receive pattern was isotropic, we moved on to measure the Rx sensitivity over frequency. The measured Rx sensitivity profile for the two single pNUTs is presented in Fig. 5.10. The process to take one data point begins by generating the ultrasound at the desired frequency, and to align the Tx with the pNUTs. This step is necessary because as we vary the frequency, the emission pattern of the ultrasound source also shifts. Next, the VA output voltage is observed. The output voltage does not remain constant over time because of the noise in the VA and because of the natural fluctuation in the pressure field generated by the Tx. While recording the voltage, the LabOne software allows to keep track of the standard deviation of the voltage at a given frequency. Empirically, we noticed that the standard deviation was always contained within a 10% range of the average VA output. We added the error bars on the plot in Fig. 5.10 to reflect this observation.

After recording the VA output voltage, the UHFLI scope was switched to the second channel connected to the calibrated microphone. While making sure that the Tx and the platform holding the pNUTs were not moved, the microphone was held right above the platform, and slightly tilted to make sure the microphone head was on the line of sight between the Tx and the devices, just at a few inches away from the pNUTs. The microphone was also moved in that region to make sure the highest possible pressure was recorded. Typically, once the microphone head is in the spot of maximum pressure, the recorded pressure is quite stable. We then obtain the voltage at the device electrodes by taking the VA output voltage, dividing it by the VA gain (approximately equal to 1800), and de-embedding the input capacitance of the VA. Because the devices capacitance is about 2.4 pF, and the measured capacitance at the VA input is 6.7 pF, the de-embedding process consists of multiplying the voltage at the VA input by a factor of 3.7. Finally, we take this voltage value and we divide it by the measured pressure to obtain the open circuit (OC) voltage sensitivity of the device. This process is repeated for several frequencies around the

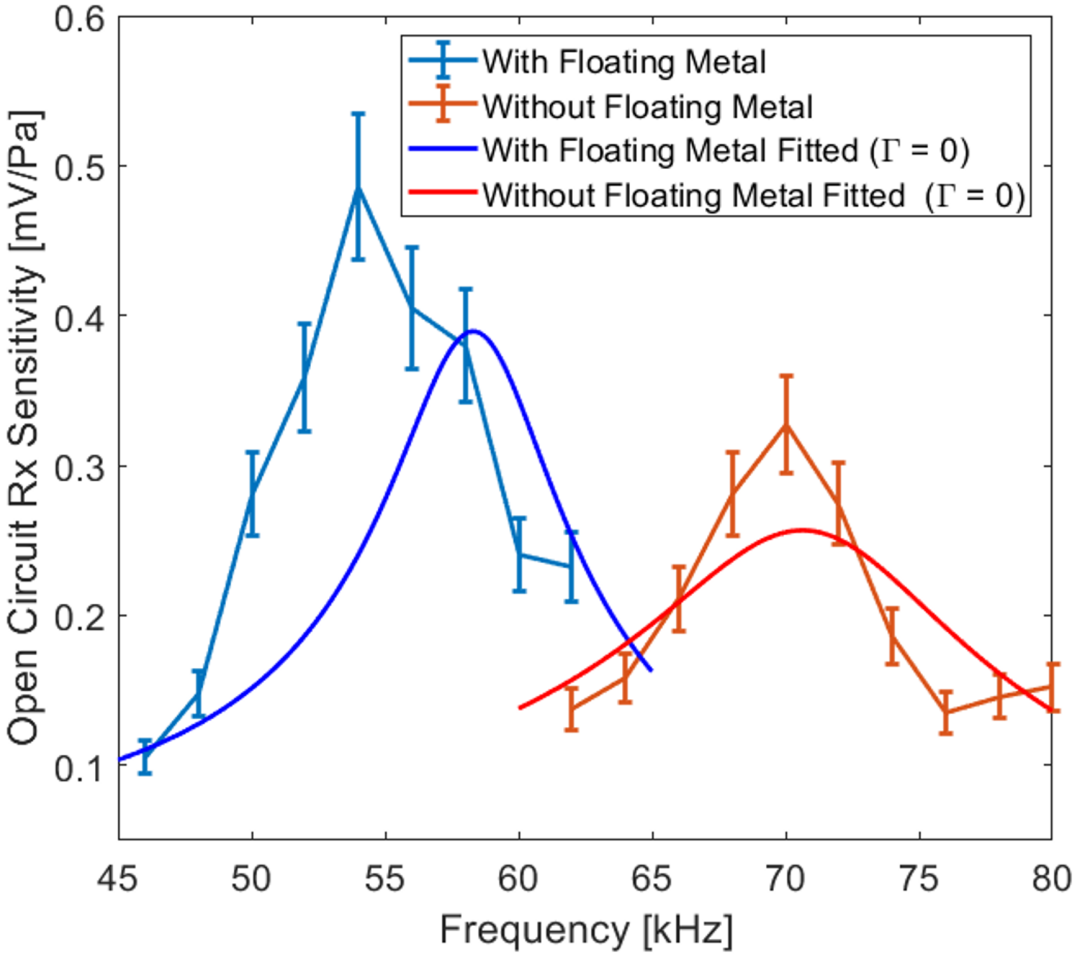


**Figure 5.10** Devices measured Rx sensitivity and extracted Rx sensitivity using the parameters extracted by fitting the displacement curves.

device resonance with 2 kHz intervals. From Fig. 5.10, we see that both devices relative position of the resonance peaks and their relative heights match the profile obtained from the Tx sensitivity measurements. We also superimpose the theoretical OC Rx sensitivities expected from the equivalent circuit model when the circuit elements are selected according to the fitted parameters. In both cases the theoretical response is slightly lower than the one expected from the fitted parameters even assuming $\Gamma = 0$ (i.e. $P_{eff} = 1$), and the resonance frequencies are slightly higher than what observed during the displacement measurements. Overall, the values of the measured Rx sensitivities are quite close to those expected from the equivalent model. More measurements are needed to establish whether the minor differences

can be eliminated with a more rigorous Rx sensitivity testing setup -aimed at reducing the uncertainty intervals- or if the equivalent circuit model itself needs to be expanded.

### Comparison with pMUTs/cMUTs Rx Sensitivity

Now that we quantified the Rx Sensitivity of the individual pNUTs, it is interesting to compare their performance against other ultrasound transducers reported in the literature. As mentioned in Section 2.1.4, the open-circuit Rx sensitivity is not frequently reported. The instances we found where the device Rx sensitivity was included -either directly or indirectly- are presented in Table 5.3.

**Table 5.3** Comparison between Rx sensitivity of the individual pNUTs and ultrasound transducers reported in literature.

| Type | $RxS[\frac{mV}{Pa}]$ | Area $[mm^2]$ | f[kHz] | $NRxS[\frac{mV}{Pamm^2}]$ | Q | Reference |
|---|---|---|---|---|---|---|
| pMUT (PZT) | 0.26 | 1.22 | 40 | 0.21 | 25 | [43] |
| pMUT (AlN) | 0.64 | 0.12 | 214 | 5.33 | 20 | [33] |
| cMUT | 41 | 16 | 50 | 2.5 | 50 | [4] [6] |
| pNUT F | 0.4 | 0.022 | 55 | 18.2 | 9 | This Thesis |
| pNUT NF | 0.3 | 0.022 | 72 | 13.6 | 6 | This Thesis |

*Obtained from reported equivalent circuit values

**Estimated

The data presented in Table 5.3 shows that despite the pNUTs are orders of magnitude smaller than transducers operating at similar frequencies, they show high Rx sensitivities in compact form factors. When normalizing the Rx sensitivity (NRxS) by the transducer area, the pNUTs fair better than classical pMUTs by 1 to 2 orders of magnitude (keeping in mind that [33] is operating at 4x the pNUTs frequency, with the consequent reduction in losses and a smaller area). These results are in agreement with the analysis presented in Section 2.1.6, and open up the possibility for truly miniaturized (sub-mm) long-range ultrasound

receivers. A demonstration of such receiver is presented in the next chapter.

## 5.3 Arrays Rx Sensitivity

A similar measurement procedure was implemented to obtain the open-circuit Rx sensitivity of the 2x2 and 3x3 SP arrays. The measured curves are presented in Fig. 5.11.

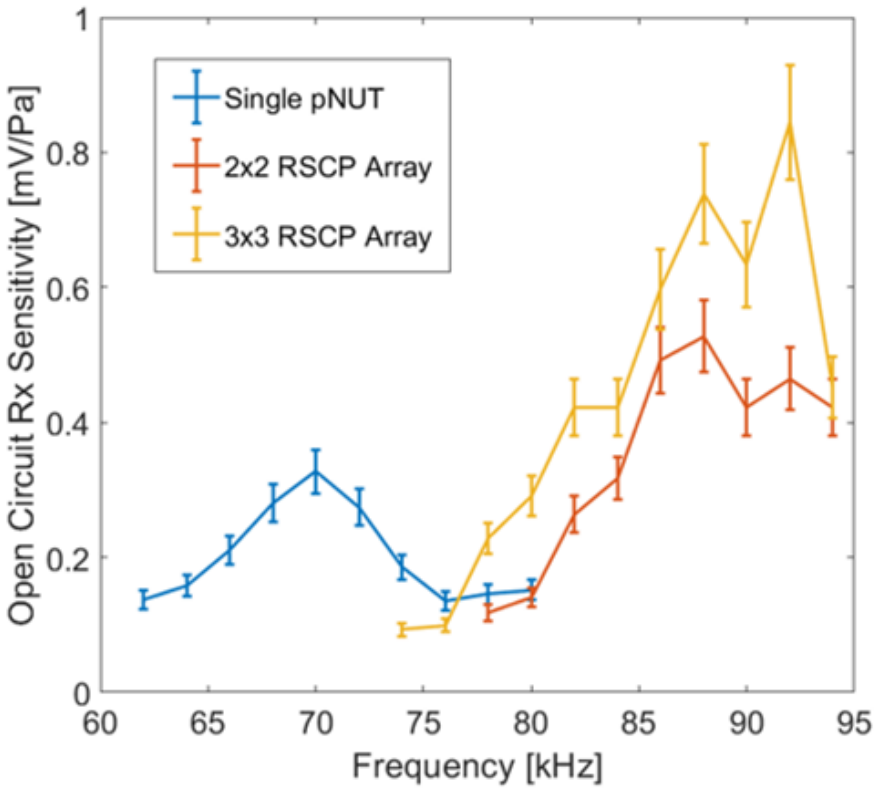


**Figure 5.11** Open-circuit Rx sensitivity of the NF single pNUT and the two arrays.

As expected from the displacement curve from Fig. 5.6, the two arrays fabricated on a separate chip present Rx sensitivity peaks at higher resonance and at around 90 kHz. In the measurements of the individual devices in the 2x2 SP array with the Lyncee Tec instrument, we observed displacements per unit voltage similar to those of the single pNUT, but we see that the Rx sensitivity of the arrays grows with the size of the array. The electrical capacitance of the individual pNUT and of the array was measured with a precision

impedance analyzer (4294a by Agilent). Both the Rx sensitivities and the capacitance at the devices electrodes vs. area are presented in Fig. 5.12.

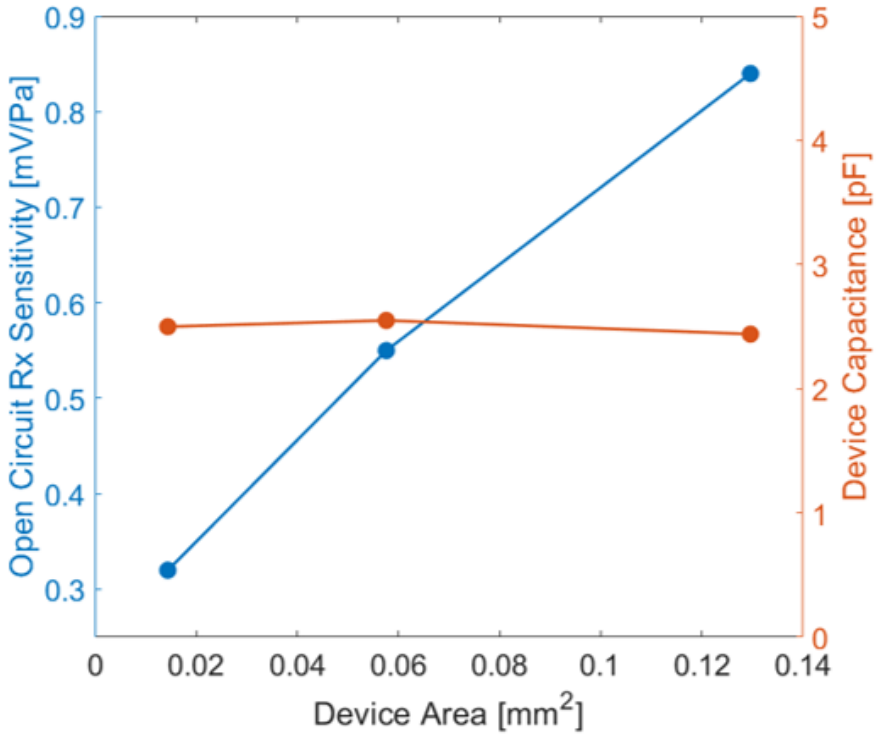


**Figure 5.12** Comparison between the peak Rx sensitivity and electrodes capacitance of the NF devices with respect to the total area. This measurement confirms the modeled trend for SP arrays as previously shown in Fig. 4.10.

We can see that, as expected from the theory of array scaling presented in Chapter 4, Rx sensitivity increases with the number of devices placed in series in each row of the SP array, while the electrodes capacitance remains constant as the array is scaled.

# Chapter 6

# WuRx System Demonstration and Characterization

The development of the IoT comes with mass deployment of wireless nodes. Typically, these nodes are expected to operate on a small battery, and the distributed nature of these networks makes it impractical to perform frequent battery swaps. From a power consumption point of view, the most demanding task for the nodes is communicating with their base-station [44]. A WuRx is a class of receivers that became popular during the last decade and that emerged as the best approach to address the issue of power consumption required to communicate asynchronously with wireless nodes.

A wireless receiver is typically formed by a transduction element and the read-out electronics interfacing with it. In RF receivers the transduction element is an antenna that converts RF waves into an electrical signal. The read-out electronics is generally divided in three parts:

1. A front-end that interfaces the antenna with the next block. This block generally provides matching to the next block and some initial amplification.

2. A mixing block that takes advantage of non-linear elements to demodulate the detected

signal.

3. A base-band block that post-processes the demodulated signal. Generally this means that the signal is further amplified and rectified.

At a high level, the system design implemented in our demonstration follows the same template outlined above, with the difference that the antenna is substituted for the pNUT and the communication takes place over acoustic waves instead of radio waves.

## 6.1 Electronics Description

To demonstrate the system, the three blocks described in the introduction are implemented respectively using:

- A voltage amplifier
- A diodes-based rectifier
- A comparator

The amplification block increases the amplitude of the electrical signal at the output of the device to ensure that it is beyond the voltage threshold necessary to trigger the rectifier. The voltage amplifier also acts as a buffer to impedance-match the pNUTs to the mixing block. The rectifier block takes the amplified modulated signal as input, and outputs its envelope, i.e. the portion of the signal that contains the information we want to retrieve. The signal envelope is then fed to the input of a comparator. The comparator acts as an analog-to-digital converter by comparing the envelope analog signal to an arbitrary threshold, and outputting either a HIGH or LOW signal. Effectively, the comparator is also a base-band amplifier matching the mixing block to the processing unit of the IoT tag. If the string of HIGHs and LOWs matches a specific signature, the main electronics is awaken.

A conceptual schematic of the complete WuRx system is shown in Fig. 6.1, while the layout of the printed circuit board (PCB) is shown in Fig. 6.2.

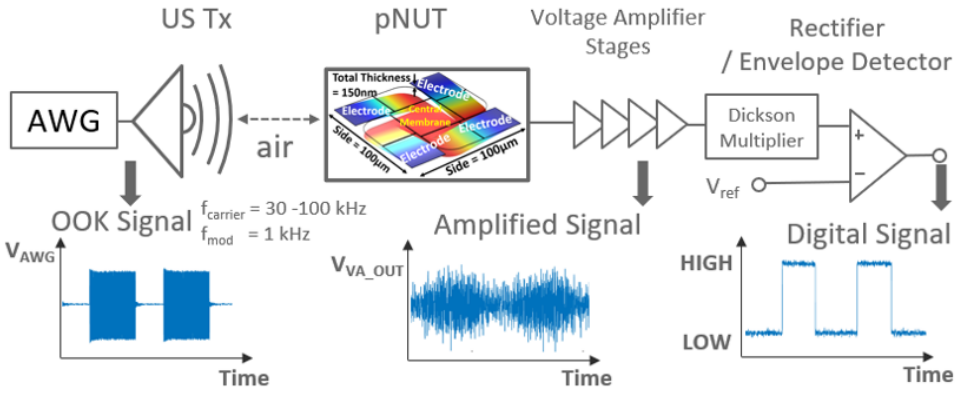


**Figure 6.1** Conceptual schematics of a US-based WuRx.

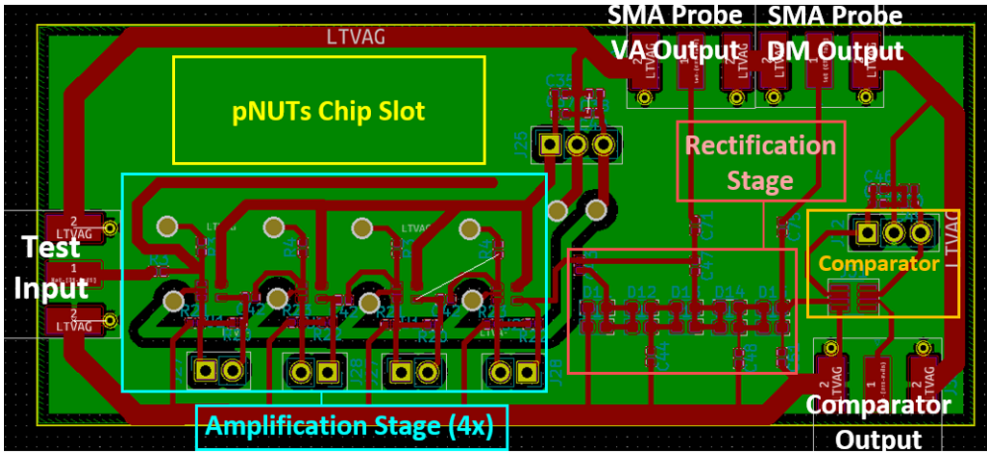


**Figure 6.2** Layout of the PCB designed to demonstrate the concept. The red and green traces represent the top and bottom layers of the PCB respectively.

The technical specification that guided the electronics design were the system range, the data rate, and the total power consumption. The system range depends on the devices Rx sensitivity, the VA and rectifier gains, and the noise levels at the comparator input. In general, we aim to be able to detect around 1 Pa pressure as it corresponds to several meters distance while complying with regulations (Fig 2.3). The system data rate depends on the modulation technique and on the time constants the rectifier is able to achieve. For simplicity, we selected an OOK modulation, and therefore the data rate is set by the

maximum modulation frequency we can achieve. We aim to achieve a modulation frequency of 1 kHz. Although this data rate is not very high compared to typical RF communication, it should be sufficient to transmit small amount of data such as a numeric key that serves as a node identifier. Finally, we target a power budget of 50 µW. The architecture of the demonstrated system is presented in the following sub-sections.

### 6.1.1 Voltage Amplifier architecture

The amplification block was implemented with a classic operational amplifier (OpAmp) non-inverting architecture. The voltage amplifier (VA) is the main source of power consumption in the system, therefore, the main metric used to select the OpAmp was the supply current. Naturally, an OpAmp characterized by a lower supply current comes with a lower gain-bandwidth (GBW) product, resulting in a smaller bandwidth for a chosen overall system gain. This trade-off can be relaxed by choosing to reduce the gain of a single OpAmp stage, hence increasing the bandwidth, and add multiple OpAmp stages in series with each other to obtain an overall gain equal to the product of the individual stages. This choice must be weighted against the increment of power consumption (proportional to the number of stages), and the additional noise introduced by every OpAmp that gets amplified at all subsequent stages. The circuit schematic of an individual OpAmp stage is shown in Fig. 6.3.

The OpAmp MIC861 by Microchip was selected because of the extremely low supply current (4 µA). According to the datasheet the MIC861 has a GBW product between 400 kHz and 650 kHz. The gain of the single stage is given by $G_1 = \frac{R_2}{R_1} + 1$, so the gain $G_n$ of $n$ consecutive stages is given by

$$G_n = (\frac{R_2}{R_1} + 1)^n. \tag{6.1}$$

In the demonstrated system we included 4 stages with $R_1 = 30k\Omega$ and $R_2 = 150k\Omega$,

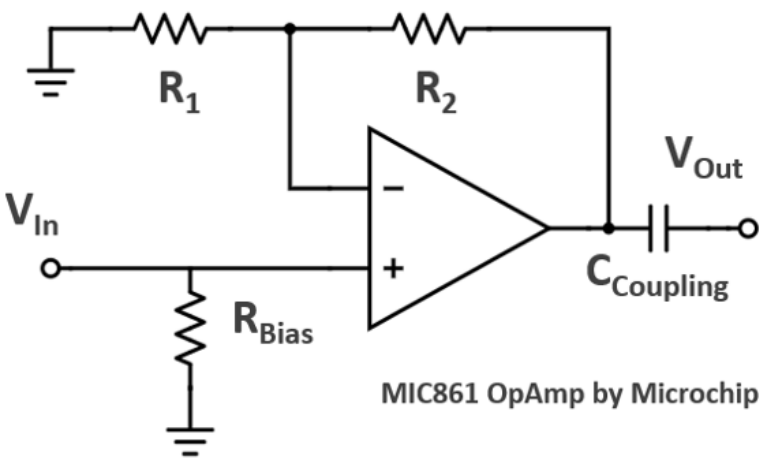


**Figure 6.3** Circuit Schematic of a single stage of the VA. The resistor $R_{bias}$ is needed to provide a path to ground to the base current of the bipolar transistor at the non-inverting terminal and correctly bias the circuit. The coupling capacitor filters out low-frequency components from the input of the next stage.

for a theoretical total gain of 1300 and a bandwidth between 70 and 110 kHz. These gain levels were selected based on the expected Rx sensitivity of the pNUTs, the desired minimum pressure detection level, and the voltage amplitude required at the voltage amplifier output to trigger the comparator. For simplicity, the benchmark values used for these three requirements were 0.1 mV/Pa, 1 Pa, and 150 mV respectively, which brings the required VA gain from 1000 to 2000 V/V.

In the layout, pins to bypass $R_2$ are included in every stage in order to remove the gain contribution of one or more stages (i.e transforming the stage into a voltage buffer). This feature was included to characterize the performance of the system in terms of operational range vs. power consumption. Fig. 6.4 shows the gain over frequency of the VA when the single stages are progressively eliminated.

When all 4 stages are active and no input is provided, the noise at the output of the VA has a standard deviation of 70 mV, with peaks of up to 200 mV amplitude. The noise was measured on the UHFLI oscilloscope by observing the histogram of the noise amplitude over time, as well as the noise spectral density in the frequency domain. The total current drawn

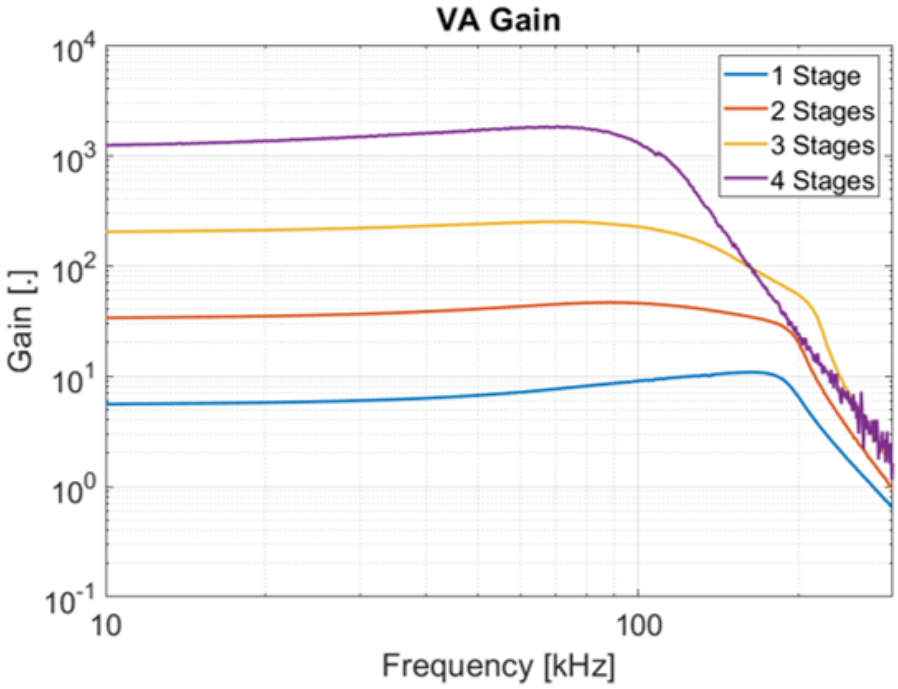


**Figure 6.4** Gain of the VA with 1, 2, 3, and 4 active stages. It is possible to see that the first stage is characterized by a pole close to 100 kHz that compensates for the decline of the gain set by the nominal GBW product. This effect slightly increase the gain, from 1300 to 1800, between 40 and 80 kHz when all 4 stages are active.

by the 4 OpAmps is 15 µA when the positive and negative supply voltages are 0.9 V and -0.9 V respectively, setting the VA total power consumption to 27 µW. On the first stage, we used the high precision impedance analyzer to measure an input capacitance of 6.7 pF. Since all devices have an electrode capacitance of approximately 2.5 pF, the input impedance of the VA will reduce the Rx sensitivity of the system compared to the open-circuit Rx sensitivity of the devices characterized in Chapter 5 by a factor of 3.7.

### 6.1.2 Rectifier Architecture

The rectifier job is to take the modulated signal as input, and output a signal with a voltage that profiles the modulation envelope. Since the harmonic components of the envelope are not present in the desired rectified signal, the rectifier needs to be composed of non-linear

elements. There are several possible architectures for the rectifier, as shown in chapter 2 of [45]. We choose a Dickson multiplier (DM) architecture for this demonstration due to its simplicity and the possibility of building it with off-the-shelf commercial components. The architecture of the DM is presented in Fig. 6.5.

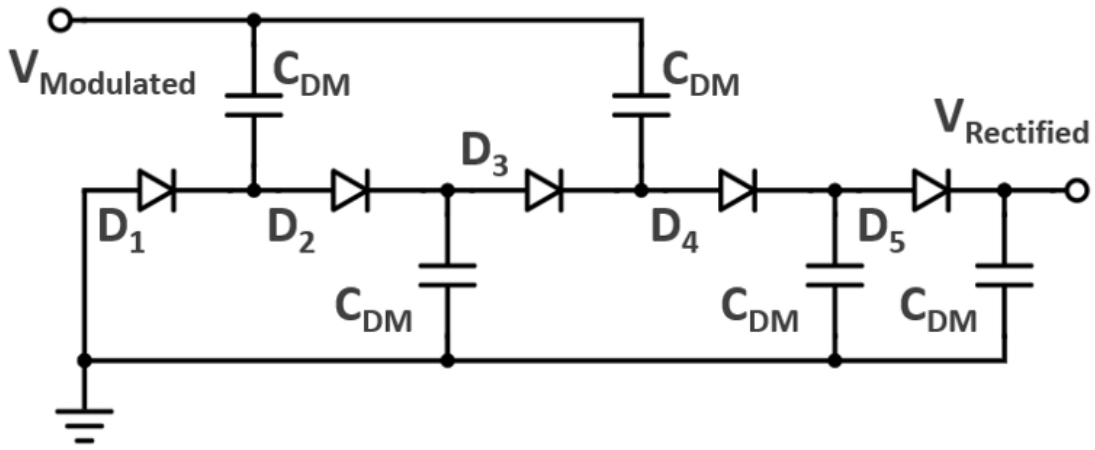


**Figure 6.5** Circuit schematics of the DM included in the PCB layout.

In the DM, an individual cell is composed by 2 diodes and 2 capacitors that alternatively connect the diodes outputs to the input line and to the ground line respectively (this configuration is also called "voltage doubler"). As the name suggests, in principle, adding more cells in series multiplies the magnitude of the output. However, the time constant of the system is increased for every additional cell, which ends up limiting the maximum modulation frequency of the system. This issue can be partially compensated by adding another diode in parallel to the ones in the topology. Adding a second diode is equivalent to having a single diode with the same threshold voltage but double reverse saturation current, resulting in faster discharge times and higher modulation frequency. Adding more diodes in parallel increases the total diode capacitance. For the DM to function as a voltage multiplier we need the diodes capacitance to be much smaller than the DM capacitances, which in turn sets the modulation frequency and the gain of the system. We use this technique (see Fig. 6.2) to increase the modulation frequency of the system and meet the target of 1 kHz. The

number of cells has been kept to 2 for simplicity, as adding more cells would require adding more diodes in parallel in each cell to maintain an appropriate time constant. The value of $C_{DM}$ is 39 pF, a value that was selected to compromise between modulation frequency and gain of the system. The selected diode model is NSR0140P2T5G by ON Semiconductor, a Schottky barrier diode characterized by a low forward threshold voltage. This diode model is characterized by a junction capacitance of 2 pF, therefore having two parallel diodes per cell ensures that the diode capacitance stands at about 10 % of the DM capacitances. The typical parabolic gain curve [46] is shown in Fig 6.6 for an amplitude-modulated (AM) 75 kHz signal with a modulation frequency of 1 kHz.

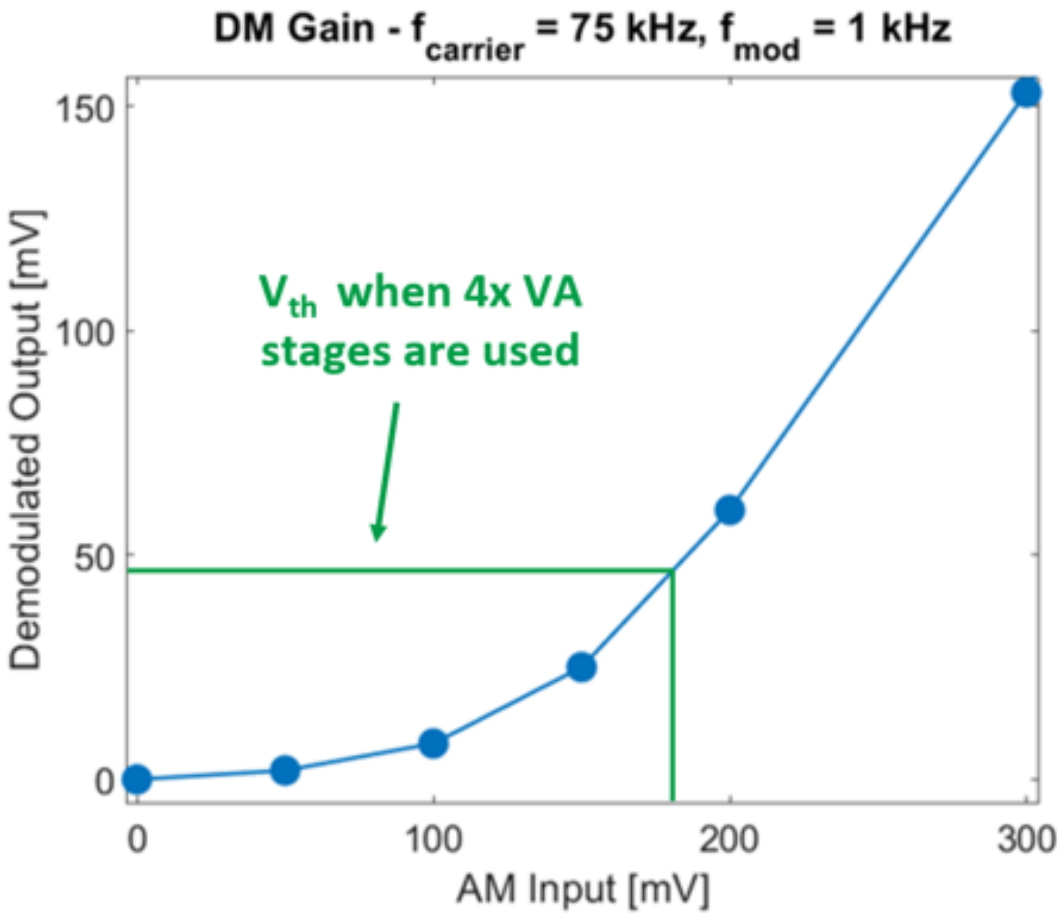


**Figure 6.6** Measured input-output curve of the DM.

The gain curve stays the same for all carrier frequencies in the desired 30-100 kHz range,

while the gain slightly increases for modulation frequencies lower than 1 kHz.

The bit error rate (BER) is the metric we use to establish whether a signal is detected or not.

We cannot assign a value to the BER of a system, but only establish whether the BER of a signal is above or below a certain threshold [47]. We choose a BER of $10^{-3}$ as threshold to consider a certain pressure signal detectable or not. The formula we use to establish that a system has a BER below a threshold with 95% confidence is [47]

$$BER \approx \frac{3}{f_{mod} Time} \tag{6.2}$$

From equation 6.2 we find that we need to correctly rectify the signal for approximately 2.5 seconds to have a BER below $10^{-3}$.

The gain curve in Fig. 6.6 was produced by providing an amplitude-modulated input through the SMA connector at the VA output. The DM gain starts to degrade incrementally beyond 1 kHz. However, modulation frequencies higher than 1 kHz would not work in the actual WuRx when the signal was fed from the VA. Because of the noise at the VA output, the system BER quickly rises beyond the threshold of $10^{-3}$ for modulation frequencies higher than 1 kHz, as the phase jitter amplitude introduced by the VA noise becomes comparable to the modulation period. As mentioned before, the white noise introduced by the VA presented spikes as high as 200 mV. Using an RMS noise of 140 mV, and following the gain in Fig. 6.6, this translates in a noise amplitude of approximately 25 mV at the rectifier output. When the VA is powered but no signal is present, noise is still present and could trigger the comparator. To avoid triggering the comparator we adjust the threshold terminal voltage. A threshold of 40 mV is selected when all four VA stages are used. The noise at the DM output is significantly reduced when three or less VA stages are used. In these cases the comparator threshold is reduced to 10 mV.

## 6.2 WuRx System Characterization

In this section we describe the experimental setup used to characterize the WuRx system and show the WuRx performance for the devices described in Chapter 5. The first step is the system assembly. In Fig. 6.2 we showed that a portion of the PCB was left empty to accommodate the chip with the fabricated devices. An opening is cut out of that region to guarantee that the devices have an open back-cavity. We placed bi-adhesive tape on the sides of the cut-out, we position the chip on top of it, and we press on the chip corners to make sure the chip is soundly connected to the PCB. It is important to have the chip firmly attached to the PCB as we will need to wirebond the pNUTs to the metal traces connected to the VA input and the system ground. If the chip moves during the wirebonding process the bond will fail, with the risk of having the wire hitting the device and breaking it. An example of the assembled system is presented in Fig. 6.7.

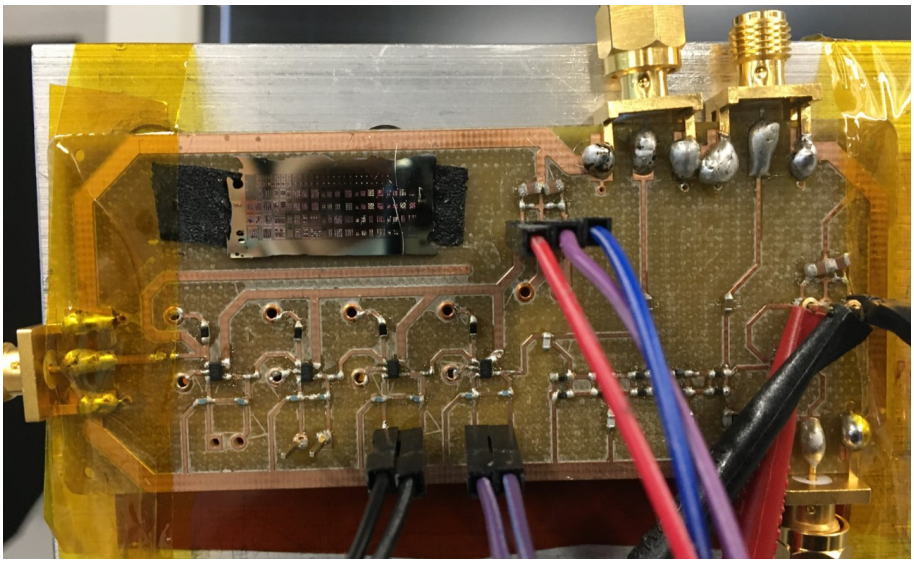

**Figure 6.7** Picture of the wirebonded chip mounted on the PCB.

The assembled system is then attached to a metal stage and mounted on a pole with adjustable height as described previously in Section 5.2.1. Unlike the experimental setup used to characterize the angular sensitivity of the devices, we position the adjustable pole on a moving cart in order to test the WuRx over various positions both for the Tx and the

Rx.

To test the the WuRx, we generate ultrasound with the source with the center frequency closest to the resonance, and we on-ff-key the signal at 1 kHz. For example, to test the single pNUT with the floating metal, which resonates at 57 kHz, we use our 50 kHz source. For the other 3 devices, with resonance frequencies of 72 and 90 kHz, we use our 80 kHz source. This means that in the actual distance measurement we are losing some performance because of the Tx-Rx frequency mismatch. We can then use the Rx sensitivity curves showed in Section 5.2.2 to infer the approximate minimum detectable pressure (MDP) in the scenario where the Tx and Rx have the same center frequency. What we consider the MDP is determined by the bit error rate (BER) observed in the output signal at the output of the comparator as explained in the previous section. To probe the signal, we monitor the VA output with the UHFLI scope, and we use a separate oscilloscope to observe the digital signal at the output of the comparator. In the way the experiment was setup, we tried to replicate as accurately as possible a free-space condition. Having a movable setup allows for positioning the Tx and Rx in a way that minimizes reflections from the surrounding and their effect on the measurement. An example of the complete experimental setup is presented in Fig. 6.8.

The measurement is performed by aligning the Tx and Rx beginning with a short distance. Once the rectified signal is observed on the oscilloscope the Tx is pulled farther away from the Rx while maintaining the alignment. Once we find the approximate distance over which the signal starts disappearing we begin fine-tuning the Tx position to determine the system range more accurately. As mentioned in Section 6.1.2, we need to monitor the signal for at least 2.5 seconds to ensure we have a BER below $10^{-3}$. To do that, we switch the time scale of the oscilloscope to at least 1 second, and monitor the signal for a few seconds. A visual inspection is sufficient to spot possible errors in the rectification. The communication range is measured once we find the maximum distance that shows no rectification errors over a few seconds measurement. Generally, we repeated the measurement varying the relative angle position of the Tx and no significant change in the communication range was

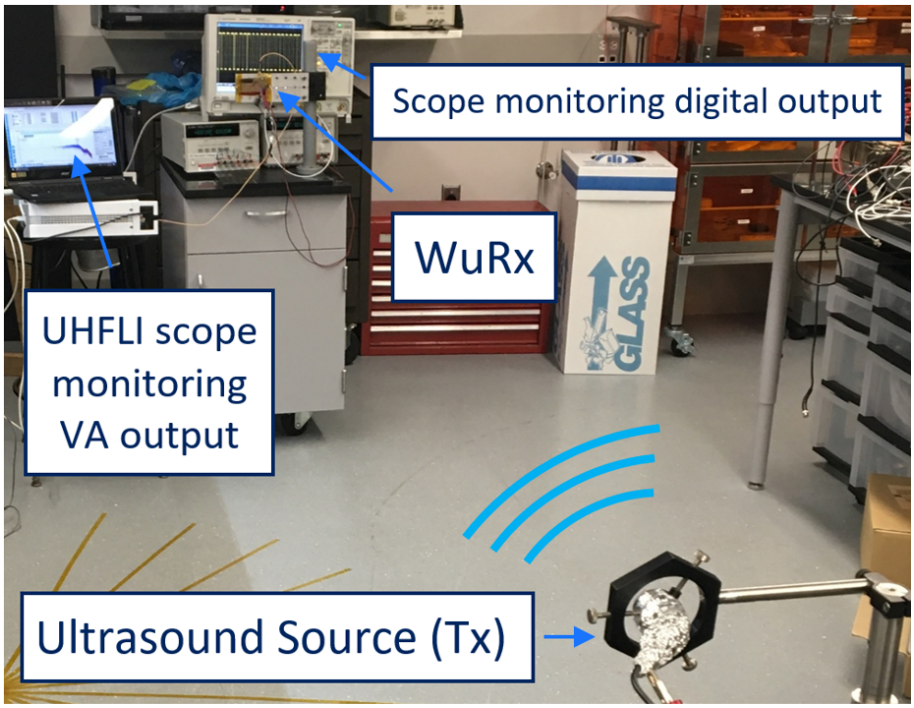


**Figure 6.8** Experimental setup to test the complete WuRx system. The Tx generates the ultrasound, which is picked up on the other side of the room by the WuRx. During the measurement, two scopes are connected to the system: the UHFLI scope is used to monitor both the VA output and the incident acoustic pressure levels, while a separate oscilloscope is used to monitor the digital signal at the output of the comparator.

observed, confirming the results of the angular sensitivity presented in Section 5.2.1. Finally, we maintain the Tx position and we switch to the second channel of the UHFLI scope to measure the pressure corresponding to the maximum range. This pressure corresponds to the MDP. For a given transducer, the procedure is repeated while reducing by 1 the number of amplification stages in the VA. We virtually remove 1 stage by connecting a jumper wire between the stage gain resistor terminals. Fig. 6.7 shows an example of what the VA looks like when two stages are bypassed, converting those stages in voltage buffers. In this way, we can characterize the system range with respect to its power consumption. This process has been repeated for the four devices characterized in Chapter 5. The devices demonstrated MDP and communication range with respect to power consumption are shown in Fig. 6.9.

The data presented in Fig. 6.9 reflects the actual measurements performed with available

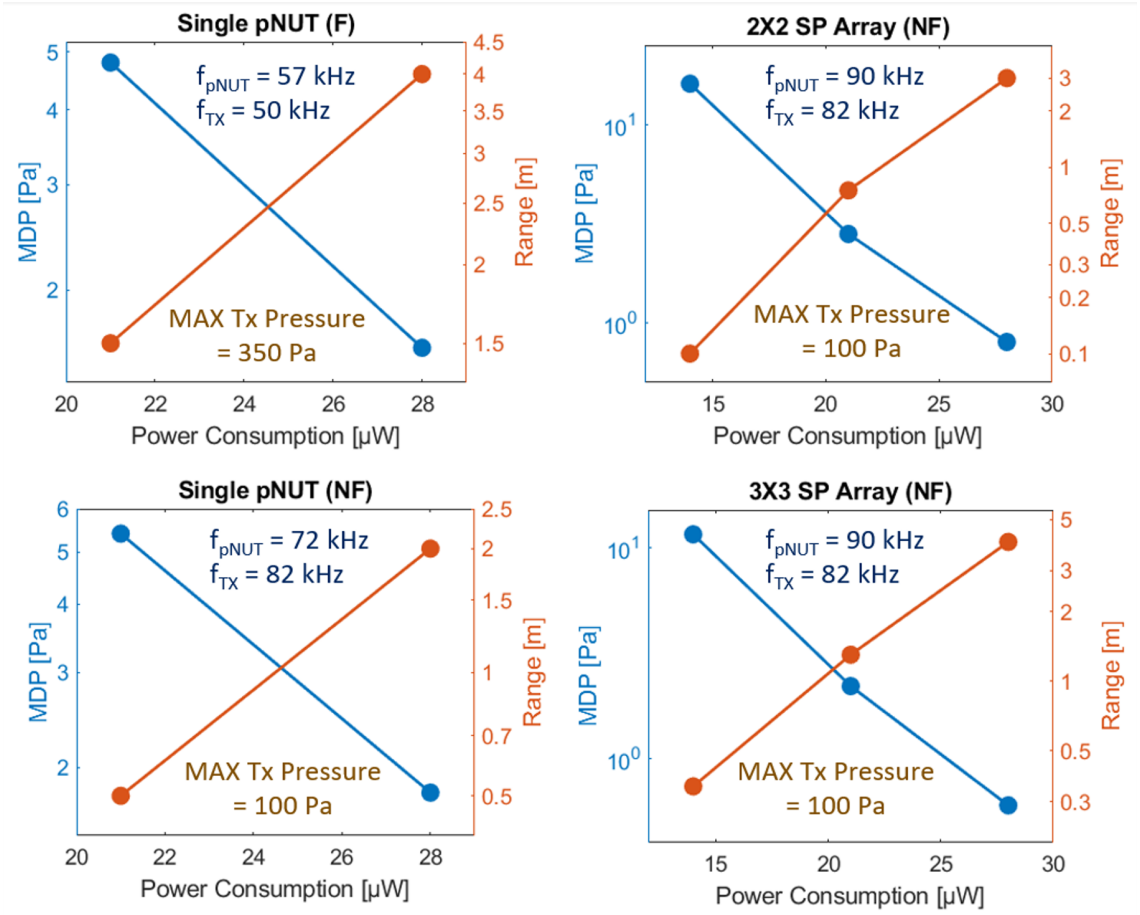


**Figure 6.9** Data collected during the WuRx demonstration. The plots show the measured MDP and communication range of the WuRx system for the 4 devices characterized in Chapter 5.

equipment, and does not reflect the full potential of the pNUTs-based system. We did not have ultrasound sources that exactly matched the resonance frequency of the devices, and therefore the measured MDP and the corresponding range can be improved under the Rx-Tx frequency match condition. Another non-ideality is that we were not able to produce pressures higher than 100 Pa with the 82 kHz Tx. To actuate it, we used a power amplifier to interface the AWG and the Tx, increasing the actuation voltage amplitude from 10 V to 25 V. For higher voltages, the source would quickly heat up, affecting the ultrasound source response curve mid-measurement. The maximum pressure limit of 100 Pa does not impact the reported MDP, and only reduces the communication range. As we reduce the

system power consumption by removing the amplification stages we have a corresponding reduction in the WuRx working range, and an increase in the MDP. As the range is reduced, we need to get the ultrasound source closer to the pNUTs to generate a pressure sufficiently high to trigger the comparator. However, below a 0.1 m distance the rectified signal did not satisfy the BER$<10^{-3}$ requirement despite the high value of the generated pressure. The likely reason for this is that as the Tx gets too close to the Rx, the effect of reflected acoustic waves is not negligible anymore, and the assumed free-field condition is no longer valid. When the single devices were used, the system range is above 0.1 m when at least 3 amplification stages are used. For this reason, only the range data points corresponding to 3 and 4 amplification stages are used. Similarly, the arrays needed at least 2 amplification stages to present a range equal or above 0.1 m. Therefore, the array plots in Fig. 6.9 present 3 data points, corresponding to when 2, 3, and 4 amplification stages are used.

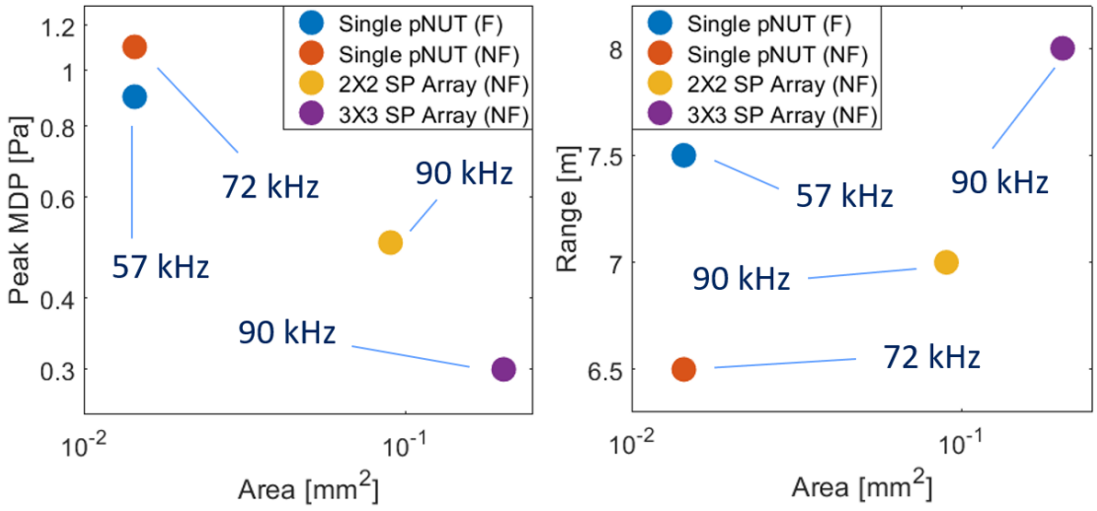


**Figure 6.10** Extrapolated MDP and range for the demonstrated WuRx system vs. transducer area. The MDP and range are obtained by assuming an ultrasound source as the one described in Fig. 2.3, and that the Tx and transducers are frequency-matched.

To get an idea of the full performance of the demonstrated WuRx, we must imagine having 1) a Tx that produces 350 Pa at the source, and 2) a Tx that is frequency-matched to the resonance frequency of the pNUTs. We can extrapolate such scenario by scaling the measured

MDP as if it was at resonance. To do that, we take a look at the Rx sensitivity curves of the devices presented in the previous chapter in Fig. 2.21. Then, we can relate the newly found MDP to a range by using the plot for an hemispherical isotropic ultrasound source as in Fig. 2.3. The extracted MDPs and the corresponding range for the 4 transducers are shown in Fig. 6.10. Fig. 6.10 clearly shows the effect of higher propagation losses experienced by acoustic waves at higher frequency. While we see that the MDP decreases as we increase the total transducer area, we can see that the 57 kHz individual pNUT present a larger range than the 2x2 SP array operating at 90 kHz.

## 6.3 Conclusion and Future Work

In this thesis we demonstrated the use of pNUTs in a working ultrasound-based WuRx. We can now compare the performance of the system with other WuRx reported in literature that use ultrasound as mean of communication. A comparison in terms of range vs. transducer area is presented in Fig. 6.11, while more detailed data is compiled in Table 6.1.

From Fig. 6.11 we see a trend outlining a trade-off between the transducer area and the MDP of the system, which in turn sets the system range. However, Fig. 6.11 does not show explicitly the role of the interfacing electronics in determining the overall system performance. In this demonstration we used off-the-shelf commercial components. Switching to an IC would bring the following improvements to the system range:

- Reduced parasitic capacitance: the VA input capacitance would decrease from 6.7 pF to a value significantly lower than the 2.5 pF across the pNUT electrodes, lowering the system MDP by a factor of 3.7. This change alone would bring the system range above 10 m.

- Reduced VA noise. The system has an input-referred rms noise of approximately 80 µV. This noise is the cause of the phase jitter at the comparator input that increases

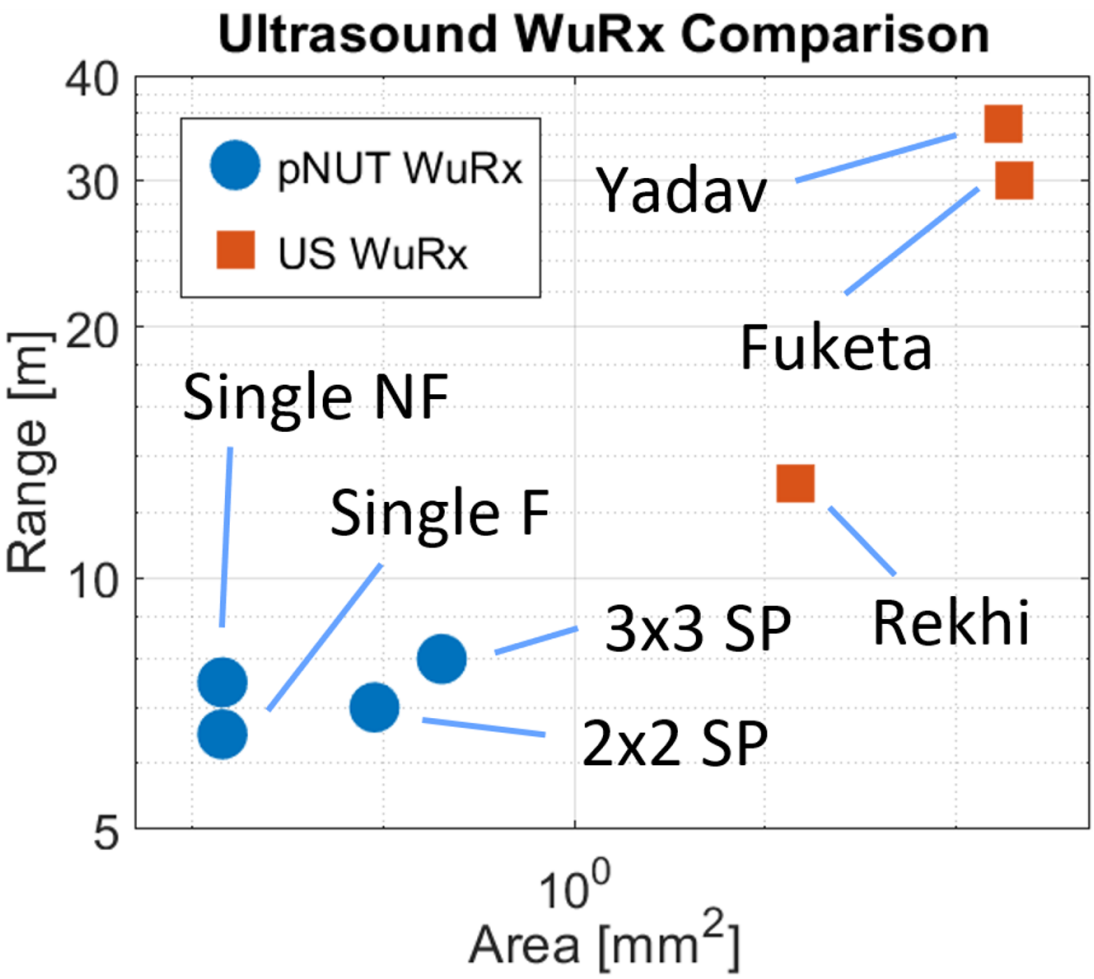


**Figure 6.11** System range vs. transducer area plot. Comparison between ultrasound WuRx.

the the BER above $10^{-3}$. It is possible to reduce it by a factor of 2 by reducing the VA bandwidth from 100 kHz down to 50 kHz.

- Improved rectifier gain. Even maintaining an identical architecture, switching to a CMOS-based DM would improve significantly the block gain. In conjunction with the previous point, this upgrade would further increase the system MDP. As an example, the rectifier gain curve from [13] is shown in Fig. 6.12. In this example the threshold for unity gain stands at 40 mV at the VA output, as opposed to several hundreds mV as in the current implementation.

**Table 6.1** Data comparing ultrasound WuRx from literature and the WuRx presented in this thesis.

| MDP $[Pa]$ | Area $[mm^2]$ | Range $[m]$ | Power $[\mu W]$ | f $[kHz]$ | IC | Reference |
|---|---|---|---|---|---|---|
| 0.004* | 178 | 35 | 4.4 | 40.6 | Yes | Yadav [48] |
| 0.005* | 201 | 30 | 1 | 41 | Yes | Fuketa [49] |
| 0.25* | 14.5 | 13 | 8e-3 | 50 | Yes | Rekhi [13] |
| 0.9 | 0.014 | 7.5 | 27 | 57 | No | This Thesis |
| 1.1 | 0.014 | 6.5 | 27 | 72 | No | This Thesis |
| 0.5 | 0.09 | 7 | 27 | 90 | No | This Thesis |
| 0.3 | 0.2 | 8 | 27 | 90 | No | This Thesis |

* Obtained from [13]. The formula to obtain the minimum detectable pressure from the Rx power sensitivity in dBm is $MDP = \sqrt{2\rho_{air}c_{air}10^{\frac{dBm}{10}}\frac{1mW}{Area}}$.

Assuming the rectifier in Fig.6.12 is used in place of our diodes implementation, the system MDP would further improve with negligible additional power consumption ($\approx$ 10 nW).

For example, we can imagine to reduce the system bandwidth to 50 kHz, and obtain a VA gain of 100 with two amplification stages (i.e. a gain of 10 per stage). With the reduced BW, the peak input-referred noise is now 60 µV, and the corresponding peak noise at the comparator input is 2 mV. Since the comparator has a hysteresis of 4 mV, we set the threshold at 6 mV. Targeting a 7 mV signal to trigger the comparator, we would need a voltage at the input of the comparator of about 0.15 mV. In the scenario where the parasitic capacitance is reduced to the point that it is negligible compared to $C_{el}$, we have lowered the MDP of the individual device (assuming a 50 kHz center frequency) to 0.3 Pa. This would extend the range to 10-12 m while reducing the power consumption to 14 µW.

On top of the improvement enabled by IC technology, different architectures are possible. For example, the circuit used in [10] presents orders of magnitude lower power consumption

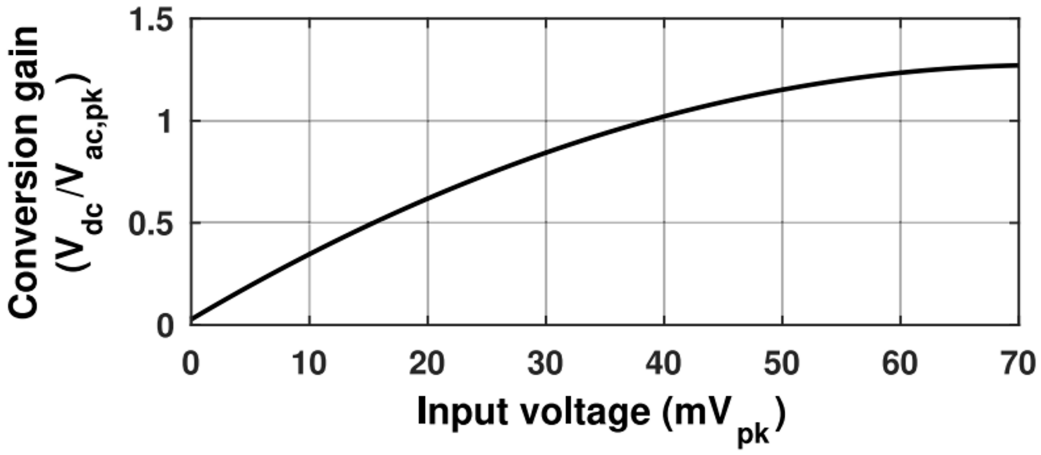


**Figure 6.12** Example of the cMOS rectifier gain curve used in [13].

for a comparable bandwidth, however it is unclear if there would be matching issues between the pNUT and this specific topology.

On the transducer side, further improvement can be achieved by making the release process more controllable. From the analysis shown in Section 2.2.1, we know that the value of $\eta$ is significantly reduced by not having a completely fixed anchor at the beams base. Once the release process is better characterized, this issue can be fixed by either minimizing the amount of undercut around the beams base, or by increasing the electrodes area further out to cover the part of the undercut area where most of the bending moment occurs. Finally, as discussed in Section 4.1.2, the lower parasitic capacitance offered by an IC, would allow to use series-connected arrays and allow for a linear improvement of the transducers Rx sensitivity, further extending the WuRx communication range.

### Comparison between Ultrasound and Radio Frequency WuRx

As mentioned in the introduction, the use of WuRxs to extend the lifetime of wireless tags gathered a lot of attention as the number of deployed sensing nodes is increasingly exponentially, and several WuRx architectures were developed, mostly relying on RF as a mean of communication. Given the multitude of applications for the nodes, the respective require-

ments in terms of power consumption, range and system area can vary significantly. Depending on the application, we will determine what carrier frequency and select the transmission medium to be either US or RF. With this in mind, we can try to contextualize the performance of the demonstrated pNUT-based system in the broader landscape of WuRxs. By following the example reported in [13], we define a figure of merit (FoM) for WuRx in general, and visualize it versus the total system area. In order to compare US and RF receivers, the FoM accounts for the minimum detectable input radiation power and for the total squared system power consumption. A lower FoM indicates a better performing transducer. The resulting FoM versus system area is shown in Fig. 6.13.

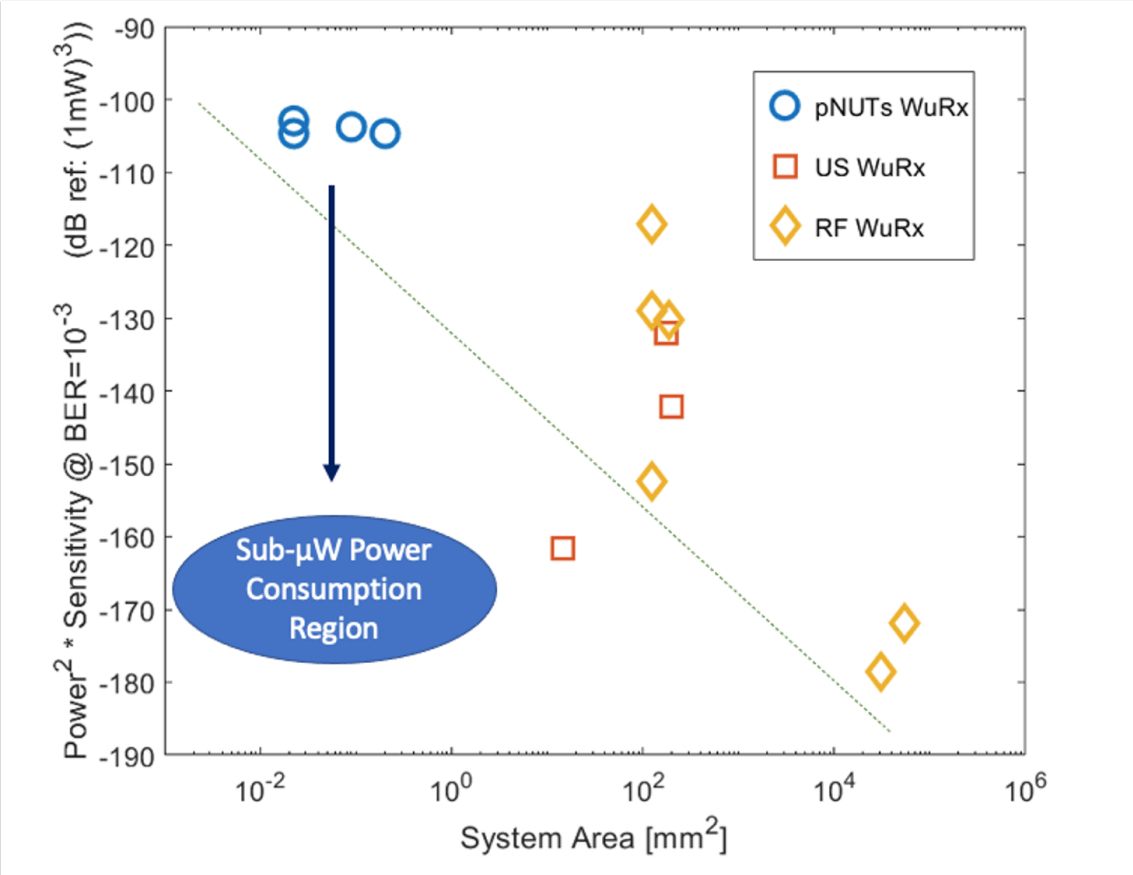


**Figure 6.13** Comparison of RF and US WuRx FoM with respect to system area. The data used to generate the plot is reported in [13].

Fig. 6.13 shows the compromise between the system performance and its area. The

system we demonstrated in this work clearly fits in the expected trade-off between FoM and area, although we notice that with the improvements to the system electronics listed above we should expect a pNUT-based WuRx to break through the trade-off line shown in Fig. 6.13.

### Future Research Directions

Besides optimizing the performance of the system demonstrated in this work, there are other research avenues where pNUTs could be useful and that are worth exploring.

The first one is related to the use of the devices higher electrical output per unit area to harvest acoustic energy and directly power standalone nodes. To do this, a large array of devices would be necessary to collect enough input power. An application scenario of such implementation was shown in Chapter 1 and a concept was shown in Fig. 1.8.

The second direction would explore an analogy in the acoustic domain for the research published on optical metasurfaces (OM) in recent years [50][51]. In the case of OM, deep sub-wavelength structures are patterned over large areas to manipulate the electromagnetic waves amplitude, phase, and frequency. In doing so, there is a higher degree of control in manipulating light compare to traditional techniques that use convex or Fresnel lenses due to the flexibility in designing surface micro-machined structures. In the acoustic domain it would be interesting to verify the feasibility of implementing ultrasound pNUT-based metasurfaces to manipulate acoustic waves in a similar fashion. A possible obstacle could be the high viscous losses we measured in the devices presented in Chapter 5, and further analysis is necessary to verify the feasibility of the project.

# References


[1] H. Basaeri, D. B. Christensen, and S. Roundy, "A review of acoustic power transfer for bio-medical implants," *Smart Materials and Structures*, vol. 25, no. 12, p. 123 001, Dec. 2016, ISSN: 0964-1726. DOI: 10.1088/0964-1726/25/12/123001.

[2] B. Herrera, F. Pop, C. Cassella, M. Rinaldi, B. Herrera, F. Pop, C. Cassella, and M. Rinaldi, "AlN PMUT-based Ultrasonic Power Transfer Links for Implantable Electronics," Institute of Electrical and Electronics Engineers (IEEE), Aug. 2019, pp. 861–864, ISBN: 9781728120072. DOI: 10.1109/transducers.2019.8808320.

[3] M. Alam, M. M. Tehranipoor, and U. Guin, "TSensors Vision, Infrastructure and Security Challenges in Trillion Sensor Era," *Journal of Hardware and Systems Security*, vol. 1, no. 4, pp. 311–327, Dec. 2017, ISSN: 2509-3428. DOI: 10.1007/s41635-017-0028-8.

[4] A. S. Rekhi, B. T. Khuri-Yakub, and A. Arbabian, "Wireless Power Transfer to Millimeter-Sized Nodes Using Airborne Ultrasound," *IEEE Transactions on Ultrasonics, Ferroelectrics, and Frequency Control*, vol. 64, no. 10, pp. 1526–1541, Oct. 2017. DOI: 10.1109/TUFFC.2017.2737620. [Online]. Available: http://ieeexplore.ieee.org/document/8006286/.

[5] Prowave, *http://www.prowave.com.tw/english/item/ut.htm*.

[6] M. C. Ho, M. Kupnik, K. Park, and B. T. Khuri-Yakub, "Long-term measurement results of pre-charged CMUTs with zero external bias operation," in *IEEE International Ultrasonics Symposium*, 2012, ISBN: 9781467345613. DOI: 10.1109/ULTSYM.2012.0022.

[7] G. Massimino, L. D'Alessandro, F. Procopio, R. Ardito, M. Ferrera, and A. Corigliano, "Air-coupled PMUT at 100 kHz with PZT active layer and residual stresses: Multi-physics model and experimental validation," in *2017 18th International Conference on Thermal, Mechanical and Multi-Physics Simulation*, IEEE, Apr. 2017, pp. 1–4, ISBN: 978-1-5090-4344-6. DOI: 10.1109/EuroSimE.2017.7926253. [Online]. Available: http://ieeexplore.ieee.org/document/7926253/.

[8] *Near Zero Power RF and Sensor Operations*. [Online]. Available: https://www.darpa.mil/program/near-zero-rf-and-sensor-operations.

[9] T. Olsson, R. Bogoslovov, E. Federal Christal Gordon, and B. Allen Hamilton, "Near-Zero Power Radio Frequency Receivers," Tech. Rep., 2017.

[10] A. Kochhar, M. E. Galanko, M. Soliman, H. Abdelsalam, L. Colombo, Y. C. Lin, G. Vidal-Alvarez, T. Mukherjee, J. Weldon, J. Paramesh, G. K. Fedder, and G. Piazza, "Resonant microelectromechanical receiver," *Journal of Microelectromechanical Systems*, vol. 28, no. 3, Jun. 2019, ISSN: 10577157. DOI: 10.1109/JMEMS.2019.2898984.

[11] T. Wu, G. Chen, C. Cassella, W. Z. Zhu, M. Assylbekova, M. Rinaldi, and N. McGruer, "Design and fabrication of AlN RF MEMS switch for near-zero power RF wake-up receivers," in *Proceedings of IEEE Sensors*, vol. 2017-December, Institute of Electrical and Electronics Engineers Inc., Dec. 2017, pp. 1–3, ISBN: 9781509010127. DOI: 10.1109/ICSENS.2017.8234413.

[12] L. X. Chuo, Y. Shi, Z. Luo, N. Chiotellis, Z. Foo, G. Kim, Y. Kim, A. Grbic, D. Wentzloff, H. S. Kim, and D. Blaauw, "A 915MHz asymmetric radio using Q-enhanced amplifier for a fully integrated 3×3×3mm3 wireless sensor node with 20m non-line-of-sight communication," in *Digest of Technical Papers - IEEE International Solid-State Circuits Conference*, vol. 60, Institute of Electrical and Electronics Engineers Inc., Mar. 2017, pp. 132–133, ISBN: 9781509037575. DOI: 10.1109/ISSCC.2017.7870296.

[13] A. S. Rekhi and A. Arbabian, "Ultrasonic Wake-Up With Precharged Transducers," *IEEE Journal of Solid-State Circuits*, vol. 54, no. 5, pp. 1475–1486, May 2019, ISSN: 00189200. DOI: 10.1109/JSSC.2019.2892617.

[14] D. Lymberopoulos, J. Liu, X. Yang, R. R. Choudhury, V. Handziski, J. Sorber, and L. Zhong, "MICROSOFT INDOOR LOCALIZATION COMPETITION: EXPERIENCES AND LESSONS LEARNED," Tech. Rep.

[15] P. Lazik and A. Rowe, "Indoor pseudo-ranging of mobile devices using ultrasonic chirps," in *SenSys 2012 - Proceedings of the 10th ACM Conference on Embedded Networked Sensor Systems*, New York, New York, USA: ACM Press, 2012, pp. 99–112, ISBN: 9781450311694. DOI: 10.1145/2426656.2426667. [Online]. Available: http://dl.acm.org/citation.cfm?doid=2426656.2426667.

[16] Y. Lu, A. Heidari, and D. A. Horsley, "A High Fill-Factor Annular Array of High Frequency Piezoelectric Micromachined Ultrasonic Transducers," *Journal of Microelectromechanical Systems*, vol. 24, no. 4, pp. 904–913, Aug. 2015, ISSN: 10577157. DOI: 10.1109/JMEMS.2014.2358991.

[17] L. Colombo, A. Kochhar, G. Vidal-Alvarez, Z. Schaffer, P. Simeoni, G. Piazza, and G. Piazza, "Comparison between different MEMS Laterally Vibrating Resonator Technologies for Passive Voltage Amplification in an RF Front-End System," in *2018 IEEE MTT-S IMWS-AMP*, IEEE, Jul. 2018, ISBN: 978-1-5386-5569-6. DOI: 10.1109/IMWS-AMP.2018.8457149. [Online]. Available: https://ieeexplore.ieee.org/document/8457149/.

[18] D. M. Pozar, *Microwave Engineering*, 4th Editio. WILEY, 2012.

[19] D. Kim, M. L. Kuntzman, and N. Hall, "A transmission-line model of back-cavity dynamics for in-plane pressure-differential microphones," *The Journal of the Acoustical Society of America*, vol. 136, no. 5, pp. 2544–2553, Nov. 2014. DOI: 10.1121/1.4897401. [Online]. Available: http://asa.scitation.org/doi/10.1121/1.4897401.

[20] J. L. Butler and C. H. Sherman, "Acoustic Radiation from Transducers," in, 2016, pp. 517–553. DOI: 10.1007/978-3-319-39044-4{_}10.

[21] K. K. Park, H. J. Lee, P. Crisman, M. Kupnik, O. Oralkan, and B. T. Khuri-Yakub, "Optimum design of circular CMUT membranes for high quality factor in air," in *Proceedings - IEEE Ultrasonics Symposium*, 2008, pp. 504–507. DOI: 10.1109/ULTSYM.2008.0123.

[22] C. R. Kwang-Hua, "Microelectromechanical systems cantilever resonators: Pressure-Dependent gas film damping," *Journal of Dynamic Systems, Measurement and Control, Transactions of the ASME*, vol. 142, no. 9, Sep. 2020, ISSN: 15289028. DOI: 10.1115/1.4047012.

[23] D. Horsley, Y. Lu, and O. Rozen, "Flexural Piezoelectric Resonators," in, 2017, pp. 153–173. DOI: 10.1007/978-3-319-28688-4{_}6.

[24] R. D. Blevins, *Formulas for Dynamics, Acoustics and Vibration*. Chichester, UK: John Wiley & Sons, Ltd, Nov. 2015, pp. 1–448, ISBN: 9781119038122. DOI: 10.1002/9781119038122. [Online]. Available: http://doi.wiley.com/10.1002/9781119038122.

[25] *Practical MEMS book: Analysis and design of microsystems, MEMS sensors (accelerometers, pressure sensors, and gyroscopes), sensor electronics, actuators, RF MEMS, and optical MEMS*. [Online]. Available: http://www.kaajakari.net/PracticalMEMS/.

[26] P. Simeoni and G. Piazza, "A Miniaturized (100 µm x 100 µm) 45 kHz Aluminum Nitride Ultrasonic Transducer for Airborne Communication and Powering," in *2019 IEEE International Ultrasonics Symposium*, Glasgow, 2019.

[27] X. Jiang, G. Luo, Q. Wang, and D. A. Horsley, "Improving PMUT Transmit Performance via Sub-Micron Thickness Scaling," in *2018 IEEE International Ultrasonics Symposium (IUS)*, IEEE, Oct. 2018, pp. 1–9, ISBN: 978-1-5386-3425-7. DOI: 10.1109/ULTSYM.2018.8580158. [Online]. Available: https://ieeexplore.ieee.org/document/8580158/.

[28] S. Akhbari, F. Sammoura, B. Eovino, C. Yang, and L. Lin, "Bimorph Piezoelectric Micromachined Ultrasonic Transducers," *JOURNAL OF MICROELECTROMECHANICAL SYSTEMS*, vol. 25, no. 2, 2016. DOI: 10.1109/JMEMS.2016.2516510. [Online]. Available: http://www.ieee.org/publications_standards/publications/rights/index.html.

[29] S. Akhbari, F. Sammoura, S. Shelton, C. Yang, D. Horsley, and L. Lin, "Highly responsive curved aluminum nitride PMUT," in *Proceedings of the IEEE International Conference on Micro Electro Mechanical Systems (MEMS)*, Institute of Electrical and Electronics Engineers Inc., 2014, pp. 124–127, ISBN: 9781479935086. DOI: 10.1109/MEMSYS.2014.6765589.

[30] S. Shelton, M. Chan, H. Park, D. A. Horsley, B. Boser, I. Izyumin, R. Przybyla, T. Frey, M. Judy, K. Nunan, F. Sammoura, and K. Yang, "CMOS-Compatible AlN Piezoelectric Micromachined Ultrasonic Transducers," 2009. DOI: 10.1109/ULTSYM.2009.0100. [Online]. Available: https://ieeexplore.ieee.org/ielx5/5430769/5441390/05441602.pdf?tp=&arnumber=5441602&isnumber=5441390.

[31] *(No Title)*. [Online]. Available: https://www.osti.gov/servlets/purl/1146165.

[32] S. Reid, G. Cagnoli, D. R. Crooks, J. Hough, P. Murray, S. Rowan, M. M. Fejer, R. Route, and S. Zappe, "Mechanical dissipation in silicon flexures," *Physics Letters, Section A: General, Atomic and Solid State Physics*, vol. 351, no. 4-5, pp. 205–211, Mar. 2006, ISSN: 03759601. DOI: 10.1016/j.physleta.2005.10.103.

[33] R. J. Przybyla, S. E. Shelton, A. Guedes, I. I. Izyumin, M. H. Kline, D. A. Horsley, and B. E. Boser, "In-air rangefinding with an AlN piezoelectric micromachined ultrasound transducer," *IEEE Sensors Journal*, vol. 11, no. 11, pp. 2690–2697, 2011, ISSN: 1530437X. DOI: 10.1109/JSEN.2011.2157490.

[34] P. W. Eaton, F. Bitsie, J. H. Smith, and D. W. Plummer, "A New Analytical Solution for Diaphragm Deflection and its Application to a Surface-Micromachined Pressure Sensor," Computational Publications, Apr. 1999, ISBN: 0966613546. [Online]. Available: https://briefs.techconnect.org/papers/a-new-analytical-solution-for-diaphragm-deflection-and-its-application-to-a-surface-micromachined-pressure-sensor/.

[35] *(PDF) Platinum Patterning by a Modified Lift-Off Technique and Its Application in a Silicon Load Cell*. [Online]. Available: https://www.researchgate.net/publication/230650384_Platinum_Patterning_by_a_Modified_Lift-Off_Technique_and_Its_Application_in_a_Silicon_Load_Cell.

[36] "Lift Lift-Off Techniques," Tech. Rep.

[37] H. Hashemi, "Transimpedance Amplifiers (TIA): Choosing the Best Amplifier for the Job," Tech. Rep., 2015. [Online]. Available: www.ti.com.

[38] B. H. Nyquist, "THERMAL AGITATION OF ELECTRIC CHARGE IN CONDUCTORS*," Tech. Rep.

[39] A. M. Niknejad and A. M. Niknejad, "Lecture 11: Electrical Noise Introduction to Noise," Tech. Rep.

[40] *Reflection DHM[r] | LyncéeTec*. [Online]. Available: https://www.lynceetec.com/reflection-dhm/.

[41] *600 MHz Lock-in Amplifier | Zurich Instruments*. [Online]. Available: https://www.zhinst.com/americas/en/products/uhfli-lock-amplifier.

[42] *Type 4939 1/4" Free-Field Microphone| Brüel & Kjær*.

[43] G. L. Luo, Y. Kusano, M. N. Roberto, and D. A. Horsley, "High-Pressure Output 40 kHz Air-Coupled Piezoelectric Micromachined Ultrasonic Transducers," in *Proceedings of the IEEE International Conference on Micro Electro Mechanical Systems (MEMS)*, vol. 2019-January, Institute of Electrical and Electronics Engineers Inc., Jan. 2019, pp. 787–790, ISBN: 9781728116105. DOI: 10.1109/MEMSYS.2019.8870618.

[44] I. Demirkol, C. Ersoy, and E. Onur, "Wake-up receivers for wireless sensor networks: Benefits and challenges - [Accepted from open call]," *IEEE Wireless Communications*, vol. 16, no. 4, pp. 88–96, Aug. 2009, ISSN: 15361284. DOI: 10.1109/MWC.2009.5281260.

[45] F. Yuan and F. Yuan, "Radio-Frequency Power Harvest," in *CMOS Circuits for Passive Wireless Microsystems*, Springer New York, 2011, pp. 7–47. DOI: 10.1007/978-1-4419-7680-2{_}2. [Online]. Available: https://link.springer.com/chapter/10.1007/978-1-4419-7680-2_2.

[46] X. Huang, G. Dolmans, H. De Groot, and J. R. Long, "Noise and Sensitivity in RF Envelope Detection Receivers," *IEEE TRANSACTIONS ON CIRCUITS AND SYSTEMS-II: EXPRESS BRIEFS*, vol. 60, no. 10, 2013. DOI: 10.1109/TCSII.2013.2278094. [Online]. Available: http://ieeexplore.ieee.org..

[47] *How Do I Measure the Bit Error Rate (BER) to a Given Confidence Level on the J-BERT M8020A and the M8040A High-Performance BERT? | Keysight*. [Online]. Available: https://www.keysight.com/main/editorial.jspx?ckey=1481106&id=1481106&nid=-11143.0.00&lc=eng&cc=US.

[48] K. Yadav, I. Kymissis, and P. R. Kinget, "A 4.4-$\mu$ W wake-up receiver using ultrasound data," *IEEE Journal of Solid-State Circuits*, vol. 48, no. 3, pp. 649–660, 2013, ISSN: 00189200. DOI: 10.1109/JSSC.2012.2235671.

[49] H. Fuketa, S. O'Uchi, and T. Matsukawa, "A 0.3-V 1- $\mu$w Super-Regenerative Ultrasound Wake-Up Receiver with Power Scalability," *IEEE Transactions on Circuits and Systems II: Express Briefs*, vol. 64, no. 9, pp. 1027–1031, Sep. 2017, ISSN: 15497747. DOI: 10.1109/TCSII.2016.2621772.

[50] J. Rho, "Metasurfaces: Subwavelength nanostructure arrays for ultrathin flat optics and photonics," *MRS Bulletin*, vol. 45, no. 3, pp. 180–187, Mar. 2020, ISSN: 08837694. DOI: 10.1557/mrs.2020.68.

[51] D. Neshev and I. Aharonovich, "Optical metasurfaces: new generation building blocks for multi-functional optics," *Light: Science and Applications*, vol. 7, no. 1, pp. 2047–7538, Dec. 2018, ISSN: 20477538. DOI: 10.1038/s41377-018-0058-1. [Online]. Available: www.nature.com/lsa.

# APPENDIX

# Appendix A

# Open Circuit Voltage vs. Gamma

Below we present the matlab script used to derive the OC Rx sensitivity of the devices in Chapter 2.

```
% Reference Transformer Ratios, Electrodes Capacitance and Scaling Factor


SF = 1; %Scaling Factor, pMUT has the same area as pNUT with SF=0.2


eta_pNUT   = 1e-7;
% eta for a pNUT with 100 µm X 100 µm area and 100/200 nm AlN/Pt (fs 50 kHz)


A_eff_pNUT = 7e-9;
% effective area of a 100 µm X 100 µm pNUT


Area_pNUT  = 1e-8;
% total area of a 100 µm X 100 µm pNUT


cap_pNUT   = 2.4e-12;
% reference capacitance pNUT


eta_pMUT   = 6.4e-6/50;
% Data estimated from [1].
% eta of a pMUT with diameter 120 µm and 100/100 nm AlN/SiO2
```

```
A_eff_pMUT = 0.3*pi*(60e-6)^2
% effective area of a pMUT with 60 µm radius

Area_pMUT  = pi*(60e-6)^2;
% total area of a 60 µm radius pMUT

cap_pMUT   = 4*14.6e-12;
% reference capacitance pMUT

%Choose pNUT or pMUT by commenting out the other

% area  = Area_pNUT*SF;
% A_eff = A_eff_pNUT*SF;
% eta   = eta_pNUT*SF;
% Cel   = cap_pNUT;

area  = Area_pMUT*SF;
A_eff = A_eff_pMUT*SF;
eta   = eta_pMUT*SF;
Cel   = cap_pMUT;

%Acoustic Domain
p_plus     = 1; %Incident Pressure
rho_air    = 1.293;
c_air      = 331.5;
Z0         = rho_air*c_air./area; %Air Acoustic Impedance
```

```
ZpNUT      = linspace(Z0/30,Z0*30,10000); %pNUT Acoustic Resistance
Gamma      = (ZpNUT-Z0)./(ZpNUT+Z0);
p_eff      = (1+Gamma)*p_plus; %Effective Pressure on pNUT
power      = p_eff.^2./ZpNUT; %Power on pNUT
efficiency = power./(p_plus^2./Z0)/2; %Efficiency from air to pNUT

%Electrical Domain

%eta      = SF*1e-7;
%Cel      = 2.4e-12; %Capacitance
f         = 50e3;%Frequency
Z_el      = 1/(2*pi*f*Cel); %Electrodes Impedance
ZpNUT_el = ZpNUT.*A_eff^2./eta^2; %pNUT resistance in electrical domain
V_eff     = p_eff.*A_eff./eta; %Effective pressure in electrical domain
V_el      = V_eff.*Z_el./(Z_el+ZpNUT_el); %Voltage across electrodes
power_el = V_el.^2./Z_el; %Electrical power actross electrodes

total_efficiency = power_el./(p_plus^2./Z0)/8;

%[1] Richard J. Przybyla et al., In-Air Rangefinding With an AlN
Piezoelectric Micromachined Ultrasound Transducer, 2011

%Plotting
plot(Gamma,1e3*V_el,'LineWidth',2)
xlabel('\Gamma', 'FontSize', 16, 'FontWeight', 'bold')
ylabel('Open Circuit Voltage [mV]','FontName','Helvetica', 'FontSize', 16)
```

# Appendix B

# Gamma Scaling

As pointed out in Chapter 2, $K_{eq}$ and $M_{eq}$ are proportional to $t^3/A$ and $tA$ respectively. In the code below, we are assuming that $t$ and $A$ are scaled together. Therefore, we can reduce the scaling to $A^2$ for both parameters. As a result, $\zeta$, is scaled proportionally to $A$ through the factor "(side/side_ref)$\hat{}$2". We assume in the code that the frequency of operation can be treated as an independent variable.

```
f0               = 1e3*[30:5:100];
sides            = 1e-6*[100:10:300];
Pin_eff          = zeros(length(f0),length(sides));
Gam              = zeros(length(f0),length(sides));
i                = 1;
for side = sides
    side_ref         = 100e-6;
    rho_air          = 1.293;
    c_air            = 331.5;
    area             = side.^2;
    Z0               = rho_air*c_air./area;
    Effective_Radius = sqrt(0.65.*area/pi);
    Zpnut            = (side/side_ref)^2*1.75e-6./area.^2;
    k_air            = 2*pi.*f0/c_air;
    Z_rad_air        = rho_air*c_air/pi./Effective_Radius.^2 .*...
        (1 - besselj(1,2.*k_air.*Effective_Radius)./k_air./Effective_Radius ...
```

```
        + 1i*StruveH1(2*k_air.*Effective_Radius)./k_air./Effective_Radius);
    Zrad              = abs(Z_rad_air);
    Zl                = Zrad + Zpnut;
    Gamma             = (Zl-Z0)./(Zl+Z0);
    Gam(:,i)    = Gamma;
    %Pin               = 1;
    %Pin_eff(:,i)       = (1+Gamma)*Pin;
    i                 = i+1;
end

surf(sides, f0, Gam)
```

# Nomenclature

| | |
|---|---|
| $\alpha$ | Coefficient accounting for viscous losses during acoustic waves propagation |
| $\eta$ | Electro-mechanical coupling coefficient |
| $\Gamma$ | Reflection coefficient at impedance boundaries |
| $\gamma$ | Coefficient accounting for ultrasound source directivity |
| $\mu$ | Surface mass density |
| $\mu_{air}$ | Air viscosity ($1.8e-5\frac{kg}{ms}$) |
| $\nu_{eff}$ | Effective Poisson ratio |
| $\phi_{elastic}$ | Fraction of the total thickness occupied by the elastic layer |
| $\phi_{piezo}$ | Fraction of the total thickness occupied by the piezoelectric layer |
| $\rho_{air}$ | Air density |
| $\rho_{eff}$ | Effective volume mass density |
| $\zeta$ | Transducer equivalent damper |
| $A$ | Transducer total area |
| $a$ | Circular pMUT radius |

$A_{eff}$ Effective transducer area

$a_{eff}$ Effective radius of the piston that best approximate the radiation impedance of the transducer

$A_{el}$ Area covered by electrodes

$C_0$ Device electrical capacitance

$C_m$ Device motional capacitance

$c_{air}$ Sound velocity in air

$C_{cavity}$ Equivalent capacitor in the acoustic domain describing the effect of of the back-cavity volume

$D$ Flexural rigidity of the films stack

$d$ pNUT vertical displacement

$e_{31,eff}$ Effective piezoelectric coefficient

$E_{eff}$ Effective Young modulus

$f_0$ Resonance frequency of the plate

$F_{eq}$ Equivalent force in the mechanical domain induced by the incident pressure

$G_n$ Boltzmann constant approximately equal to $1.38e-23[\frac{m^2kg}{s^2K}]$

$G_n$ Total gain of n consecutive voltage amplifier stages

$J1$ Bessel function of the first kind, order 1

$J1$ Struve function of order 1

$K_{eq}$ Transducer equivalent stiffness

$L_m$ Device motional inductance

$L_b$ pNUT beams length

$l_{slot}$ total length of the slots etched in the piezoelectric layer

$M_{eq}$ Transducer equivalent mass

$P^+/P^-$ Amplitude of a forward/backward-propagating acoustic wave in a delay line

$P_{in}$ Effective acoustic pressure at the device acoustic port

$P_{Tx}$ Acoustic pressure at the ultrasound source location

$r$ Distance from the ultrasound source

$R_1, R_2$ Gain resistances in an individual stage of the voltage amplifier

$R_m$ Device motional resistance

$r_{Tx}$ Radius of the ultrasound source

$t$ Transducer thickness

$t_{slot}$ Thickness of the slot etched in the piezoelectric layer

$V$ Volume of the back-cavity

$V_{out}$ Voltage across the device terminals

$V_{Pin}$ Equivalent input voltage generated by the incident pressure

$W_b$ pNUT beams width

$w_{slot}$ width of the slots etched in the piezoelectric layer

$x$ Normalized position along pMUT radius / pNUT beams length

$x_{el}$ Portion of the device covered by electrodes

$Y(x)$ Device mode shape

$Z_0$ Characteristic impedance in a delay line

$Z_L$ Load impedance in a delay line

$z_{neutral}$ Relative position of the neutral plane along the stack thickness

$Z_{pNUT}$ Acoustic impedance of the device seen from the acoustic port

$Z_{rad}$ Radiation impedance of the transducer